

**The Kemp Caldera hydrothermal system, Scotia Sea –  
Morphological, mineralogical and geochemical  
characteristics**

DISSERTATION

zur Erlangung des  
Doktorgrades der Naturwissenschaften  
(Dr. rer. nat.)

am Fachbereich Geowissenschaften  
der Universität Bremen

vorgelegt von  
**Victoria Kürzinger**

Eingereicht am 14. September 2022  
Promotionskolloquium am 25. November 2022



## **Gutachter**

Prof. Dr. Wolfgang Bach

Universität Bremen

MARUM – Zentrum für Marine Umweltwissenschaften

Klagenfurter Straße 2-4

28359 Bremen

Prof. Dr. Colin Devey

GEOMAR – Helmholtz-Zentrum für Ozeanforschung Kiel

Wischhofstraße 1-3

24148 Kiel



## PREFACE

Finding the origin of life has been in focus of scientific research for centuries. One hypothesis concerning the origin of mankind is the theory of evolution by Charles Darwin. Human history dates back at least three million years, when our earliest and human-like ancestors of the species *Australopithecus* and *Homo* entered the stage of the Earth. Since then, not only human evolution has progressed with great strides, but also cultural, social and technical developments have continuously improved.

With the development of new technologies and the resulting possibility to travel by land and sea, explorers and voyagers such as Christopher Columbus, Vasco da Gama, James Cook, Alexander von Humboldt and Roald Amundsen were able to sail the oceans and discover new ways and continents. The spirit of discovery was great and as Aristotle said: “All men strive for knowledge by nature.”

Despite the efforts over the past centuries to understand the world in its entirety, it still holds – literally deep – secrets. Earth's oceans have remained largely hidden from humans, and supposedly we seem to know more about the Moon than we do about the deep sea. Not even 200 years ago in the middle of the 19<sup>th</sup> century, exploration of the deep sea began. At this time, a remarkable discovery was made during the British R/V *Challenger* expedition from 1872 to 1876. They found about 5000 unknown species of living beings at a depth of more than 5 km. This was quite a big step in the exploration of the deep sea, since only a few years before it was assumed that no life is possible at water depths beyond 500 m. Together with the discovery of hydrothermal vents in the 1970s, another great discovery was made: Hydrothermal vents in the deep sea host a variety of species that do not depend on sunlight and have adapted to a way of life that is hostile and unknown to humans. Although hydrothermal vents are among the most extreme environments on Earth in terms of temperature and toxicity of the discharging fluids, they are oases of life. However, this kind of research is not only about exploring the deep sea as a natural habitat, but also to get better insights into physics and evolution of the ocean crust, natural hazards and the entire system earth.

In my thesis, the focus is set on hydrothermal systems, especially on the hydrothermal system of the Kemp Caldera in the Scotia Sea. Because my PhD project is part of the MARUM “Cluster of Excellence” in the general area “The Ocean Floor as Reactor – Theme 3: Processes and dynamics of vents and seeps”, I joined the R/V *Polarstern* PS119 cruise in 2019 to the Eastern Scotia Sea. Here, I focused on the scientific problems of the Kemp Caldera, one of the largest submarine volcanic structures of the South Sandwich island arc. This submarine arc caldera volcano hosts a unique hydrothermal system in terms of isotopically heavy sulfur.

Since the discovery of the Kemp Caldera in 2009, the caldera has been the focus especially of biological studies, but from a geological point of view, it is very poorly understood. This work thus aims to provide new insights in morphology, mineralogy and geochemistry of the Kemp Caldera hydrothermal system.

---

**TABLE OF CONTENTS**

Preface.....	I
Table of contents.....	III
List of abbreviations .....	V
Abstract.....	VI
Zusammenfassung.....	VII
Outline and contributions to manuscripts.....	VIII
1 Introduction to hydrothermal systems.....	1
1.1 Subaerial hydrothermal systems .....	1
1.2 Submarine hydrothermal systems .....	6
1.3 Life at hydrothermal vents .....	10
1.4 Mineral deposits and processes at hydrothermal vents .....	11
1.5 Stable isotopes in hydrothermal systems .....	13
1.6 Geologic setting and study area of the Kemp Caldera.....	14
2 Motivation and objectives .....	16
3 Manuscript I – The Kemp Caldera, the southernmost arc caldera volcano from the South Sandwich island arc – New results from seafloor investigations .....	17
Abstract .....	17
3.1 Introduction .....	18
3.2 Geologic setting .....	18
3.3 Methods .....	21
3.4 Results.....	23
3.5 Discussion.....	34
3.6 Conclusion .....	38
Acknowledgements.....	38
4 Manuscript II – Sulfur formation associated with coexisting sulfide minerals in the Kemp Caldera hydrothermal system, Scotia Sea.....	39
Abstract .....	39
4.1 Introduction .....	40
4.2 Geologic setting and sampling locations.....	42

## Table of contents

---

4.3	Materials and Methods .....	46
4.4	Results .....	49
4.5	Discussion.....	58
4.6	Summary and conclusions .....	72
	Acknowledgements.....	73
5	Manuscript III – Experimental study of sulfur isotopic composition of white smoker precipitates in the Kemp Caldera (Scotia Sea) .....	74
	Abstract .....	74
5.1	Introduction .....	75
5.2	Methods .....	77
5.3	Results.....	80
5.4	Discussion.....	83
5.5	Conclusion .....	90
	Acknowledgements.....	90
6	Conclusions and outlook .....	91
	Acknowledgements .....	95
	References.....	97
	Appendix .....	114

---

**LIST OF ABBREVIATIONS**

BC	Beehive Chimney	Anh	anhydrite (CaSO <sub>4</sub> )
EPR	East Pacific Rise	Bar	barite (BaSO <sub>4</sub> )
GW	Great Wall	Bn	bornite (Cu <sub>5</sub> FeS <sub>4</sub> )
MOR	mid-ocean ridge	Cc	chalcocite (Cu <sub>2</sub> S)
MORB	mid-ocean ridge basalt	Cpy	chalcopyrite (CuFeS <sub>2</sub> )
TAG	Trans-Atlantic Geotraverse	Cv	covellite (CuS)
		Mar	marcasite (FeS <sub>2</sub> )
GWB	Geochemist's Workbench	Py	pyrite (FeS <sub>2</sub> )
		S <sup>0</sup>	elemental sulfur (S)
IGT	isobaric gas-thight (fluid samplers)	Sph	sphalerite (ZnS)
MBES	multibeam echosounder	Ten	tennantite (Cu <sub>10</sub> [Fe,Zn] <sub>2</sub> As <sub>4</sub> S <sub>18</sub> )
OFOBS	Ocean Floor Observation and Bathymetry System		
ORP	oxidation-reduction potential	AFM	alkali-iron-magnesium diagram
ROV	Remotely Operated Vehicle	TAS	total-alkali silica diagram
USBL	ultra-short baseline		
EA-IRMS	elemental analyzer isotope ratio mass spectrometry		
IC	ion chromatography		
ICP-OES	inductively coupled plasma optical emission spectroscopy		
SEM-EDX	Scanning Electron Microscopy with Energy Dispersive X-ray Analysis		
XRD	X-ray diffraction		
XRF	X-ray fluorescence		
α	fractionation factor		
δ	deviation from standard (variations in isotope ratio)		
Δ <sub>R</sub> G	Gibbs energy		
Δ <sub>R</sub> G <sup>0</sup>	standard state Gibbs energy		
ll-pol	plane polarized light		
x-pol	crossed polarized light		

## ABSTRACT

Submarine calderas are a unique form of hydrothermal systems, which are not yet well understood in terms of how they form or how they develop over time. One of the least explored submarine calderas is the Kemp Caldera, which is located in the Scotia Sea in the rear-arc region of the southernmost part of the South Sandwich island arc. Since its discovery in 2009, the caldera has been of great interest primarily to bioscience researchers, but within the last few years, the Kemp Caldera has also been increasingly studied from a geoscientific perspective.

One of the objectives of the R/V *Polarstern* PS119 expedition in 2019 was the investigation of the Kemp Caldera and its hydrothermal system in more detail. New bathymetric data together with visual seafloor observations and rock samples now show that the caldera was formed by two collapse events, resulting in a prominent morphology. The shape of the resurgent cone, which occurs in the central part of the caldera, and the results of rock analyses indicate a dacitic post-caldera eruption that was responsible for the formation and development of several vent fields. Two of these hydrothermal fields, Great Wall and Toxic Castle, located on the eastern slope of the central resurgent cone, are of particular interest. Here, contrary to other hydrothermal systems in this area, elemental sulfur occurs not only in fine-crystalline, but also in liquid form. Sampling and later investigation of the sulfur and other hydrothermal precipitates showed that the elemental sulfur is isotopically heavy and thus cannot be attributed to the generally accepted formation by  $\text{SO}_2$  disproportionation. Instead, the observed isotopic composition of sulfur must be the result from synproportionation of  $\text{SO}_2$  and  $\text{H}_2\text{S}$ . Although this reaction has not been documented from other hydrothermal systems, the use of a thermodynamic computation software and a Rayleigh fractionation model demonstrated that synproportionation is thermodynamically possible both at Great Wall and Toxic Castle, and capable of producing the observed sulfur isotopic composition. Moreover, experiments carried out under hydrothermal conditions produced artificially generated sulfur, whose measured isotope values matched those predicted by the Rayleigh fractionation model for synproportionation. This thesis therefore proves, for the first time, that synproportionation can form sulfur in hydrothermal environments and might thus represent a previously unknown source of isotopically heavy sulfur.

## ZUSAMMENFASSUNG

Submarine Calderen sind eine einzigartige Form von Hydrothermalsystemen, über deren Entstehung und Entwicklung trotz intensiver Forschung nur wenig bekannt ist. Eine der bisher am wenigsten erforschten submarinen Calderen ist die Kemp Caldera, welche in der Schottische See im hinteren Bereich des südlichsten Teils des Süd-Sandwich-Inselbogens liegt. Seit ihrer Entdeckung im Jahr 2009 war sie vor allem für die biowissenschaftliche Forschung von großem Interesse, doch innerhalb der letzten Jahre wurde die Kemp Caldera auch vermehrt aus geowissenschaftlicher Perspektive untersucht.

Ein Ziel der *Polarstern* PS119 Expedition 2019 war die nähere Untersuchung der Kemp Caldera und ihres hydrothermalen Systems. Neue bathymetrische Daten zusammen mit visuellen Beobachtungen des Meeresbodens und Gesteinsproben geben nun Aufschluss darüber, dass die Caldera durch zwei Kollapsevents entstanden ist. Die Form des sekundär-magmatischen Kegels, der sich im zentralen Bereich der Caldera befindet, und die Ergebnisse der Gesteinsanalysen weisen auf eine dazitische post-caldera Eruption hin, die ausschlaggebend für die Entstehung und Entwicklung einiger Hydrothermalfelder gewesen ist. Zwei dieser hydrothermalen Felder, Great Wall und Toxic Castle, die sich am östlichen Hang des zentralen sekundär-magmatischen Kegels befinden, sind von besonderem Interesse. Im Gegensatz zu anderen hydrothermalen Systemen in diesem Gebiet kommt elementarer Schwefel hier nicht nur in feinkristalliner, sondern auch in flüssiger Form vor. Die Beprobung und spätere Untersuchung des Schwefels und anderer hydrothermalen Präzipitate zeigten, dass der elementare Schwefel isotopisch schwer ist und somit nicht auf die allgemein anerkannte Bildung durch  $\text{SO}_2$ -Disproportionierung zurückgeführt werden kann. Die beobachtete Isotopenzusammensetzung des Schwefels ist vielmehr das Ergebnis der Synproportionierung von  $\text{SO}_2$  und  $\text{H}_2\text{S}$ . Obwohl diese Reaktion in anderen hydrothermalen Systemen bisher nicht dokumentiert wurde, hat die Verwendung einer thermodynamischen Berechnungssoftware und eines Rayleigh-Fraktionierungsmodells gezeigt, dass die Synproportionierung sowohl in Great Wall als auch in Toxic Castle thermodynamisch möglich ist und die beobachtete Schwefelisotopenzusammensetzung hervorbringen kann. Darüber hinaus wurde bei den unter hydrothermalen Bedingungen durchgeführten Experimenten künstlich hergestellter Schwefel produziert, dessen gemessene Isotopenwerte mit denen übereinstimmten, die das Rayleigh-Fraktionierungsmodell für die Synproportionierung vorhersagt. Mit dieser Arbeit wird somit zum ersten Mal nachgewiesen, dass durch Synproportionierung Schwefel in hydrothermalen Umgebungen gebildet werden kann und somit eine bisher unbekannte Quelle für isotopisch schweren Schwefel darstellen könnte.

## OUTLINE AND CONTRIBUTIONS TO MANUSCRIPTS

This cumulative thesis focuses on submarine arc and back-arc hydrothermal systems and is intended to provide a better overview of the Kemp Caldera hydrothermal system in particular, which has been exclusively viewed and studied from a biological perspective until now. The thesis first provides a general introduction into (submarine) hydrothermal systems and their associated processes (chapter 1), which is followed by a short description of the state of the art and the identification of relevant knowledge gaps. These serve as motivation for this thesis and are stated along the objectives for this work (chapter 2).

Three manuscripts, each with a different perspective on the Kemp Caldera, were and will be submitted to scientific journals and form the core of this thesis. The first manuscript (chapter 3) gives an overview of the morphology of the Kemp Caldera and its hydrothermal vent sites, which are described and interpreted on the basis of first petrological results from rocks sampled with the ROV *MARUM QUEST 4000* and visual seafloor observations both from ROV and OFOBS dives. The second manuscript (chapter 4) focuses on the hydrothermal precipitates of the active vent sites in the center of the caldera and the newly discovered location on the NNW caldera rim. The mineral accumulations from this location were studied in more detail, using analytical methods (microscopy, SEM-EDX, etc.). Elemental sulfur occurring at the central vent fields was examined particularly closely, since the formation of the isotopically heavy sulfur observed here could not be explained by the sulfur formation processes known so far. A hypothesis of sulfur formation by synproportionation of  $\text{SO}_2$  and  $\text{H}_2\text{S}$  is already discussed theoretically in the second manuscript but also forms the basis of the third manuscript (chapter 5), where it was proven by laboratory experiments carried out under hydrothermal conditions. The results indicate that the formation of isotopically heavy sulfur is practically feasible and thus can also take place in nature.

In the final section (chapter 6), the findings of the three manuscripts are summarized, followed by the acknowledgements, a complete reference list, and the appendix. A list of authors with their contributions to the respective manuscripts is provided in the tables below:

---

**Manuscript I – The Kemp Caldera, the southernmost arc caldera volcano from the South Sandwich island arc – New results from seafloor investigations**

<b>Author</b>	<b>Contribution to manuscript</b>
Victoria Kürzinger	Lead author of the manuscript, creation and illustration of all figures, data interpretation
Miriam Römer	Study planning and design, responsible scientist for ROV dive 449, support in creation of maps, critical revision of the manuscript
Anna Lichtschlag	Responsible scientists for ROV dive 447, revision of the manuscript
Gerhard Bohrmann	Chief scientist of the PS119 research cruise, supporting contributions to the manuscript, revision of the manuscript

**Manuscript II – Sulfur formation associated with coexisting sulfide minerals in the Kemp Caldera hydrothermal system, Scotia Sea**

<b>Author</b>	<b>Contribution to manuscript</b>
Victoria Kürzinger	Lead author of the manuscript, creation and illustration of all figures, study planning and design, mineralogical analysis and data interpretation, calculation of synproportionation energetics and Rayleigh fractionation model
Alexander Diehl	Chemical analyses of vent fluids, critical revision of the manuscript
Samuel I. Pereira	Chemical analyses of vent fluids, revision of the manuscript
Harald Strauss	Sulfur isotope measurements, revision of the manuscript
Gerhard Bohrmann	Chief scientist of the PS119 research cruise, study planning and design
Wolfgang Bach	Supporting contributions to the manuscript, model calculations with GWB, support with Rayleigh fractionation model, critical revision of the manuscript

**Manuscript III – Experimental study of sulfur isotopic composition of white smoker precipitates in the Kemp Caldera (Scotia Sea)**

<b>Author</b>	<b>Contribution to manuscript</b>
Victoria Kürzinger	Lead author of the manuscript, creation and illustration of all figures, study planning and design, planning and conducting of the experiments, SEM-EDX analysis and data interpretation, modelling of Rayleigh fractionation
Christian T. Hansen	Planning and conducting of the experiments, revision of the manuscript
Harald Strauss	Sulfur isotope measurements, revision of the manuscript
Shi-Jun Wu	Provision of the titanium reaction cells for hydrothermal experiments
Wolfgang Bach	Planning of the experiments, support with thermodynamic calculations, critical revision of the manuscript



## 1 INTRODUCTION TO HYDROTHERMAL SYSTEMS

Hydrothermal systems can be found in many places around the world. They are often the visual expression of volcanic activity, magma degassing and other geodynamic processes happening deep inside the Earth (Iwasaki et al., 1963; Rinehart, 1980). Hydrothermal systems occur both subaerial and submarine, where subaerial systems occur as geysers, hot springs or fumaroles in the direct neighborhood of volcanoes. Submarine hydrothermal activity on the other hand is usually expressed in form of hydrothermal vents found primarily along mid-ocean ridges (MORs), volcanic arcs and back-arc basins (Leat and Larter, 2003; German and Seyfried, 2014; de Ronde and Stucker, 2015).

The existence of subaerial hydrothermal systems has always been known, as they are visible features on the surface of the Earth and thus generally easily accessible to us. Conversely, submarine hydrothermal systems were inaccessible and therefore remained elusive for a long time. In 1977, the first deep-sea hydrothermal vents were discovered at the Galápagos Spreading Center in the eastern equatorial Pacific (Corliss et al., 1979). This discovery was probably one of the greatest and most spectacular scientific achievements of the late 20<sup>th</sup> century. Besides the discovery of warm (maximum temperatures of 17 °C) shimmering water emerging from the volcanic basement (Corliss et al., 1979), one highlight was the unique faunal diversity found around the hydrothermal vents. For the first time, within this hostile-believed environment, chemosynthetic communities were discovered as the first known organisms that can live light-independently (Haymon et al., 2007). Only two years after the discovery of the first vent communities, much hotter hydrothermal vents with temperatures of  $380\pm 30$  °C were discovered at the East Pacific Rise in 1979 (Spiess et al., 1980). These chimneys are known as black smokers because their plumes are colored black due to tiny particles of sulfide minerals. Due to the progressing development of especially submarine research techniques, hydrothermal systems have received increasing attention and their investigation is still one of the major interests of science today.

### 1.1 Subaerial hydrothermal systems

Probably the most familiar phenomena of subaerial hydrothermal systems are geysers, fumaroles and hot springs. Geysers are fountains of steam-heated groundwater occurring in areas of volcanic activity (Pirajno, 2020). A water column exerts pressure on its deeper layers, so that the boiling temperatures there are higher than in the upper level. As a result, water begins to boil at depth and raises the overlying water column, causing a pressure release, which is followed by a sudden burst of superheated water discharged as steam at the Earth's

surface (Pirajno, 2020). Examples of famous or spectacular geysers are the Great Geysir and Strokkur (Iceland) as well as Old Faithful and Great Fountain in the Yellowstone National Park (USA). Other places where geysers can be found are the New Zealand's North Island, Chile and Indonesia.

Fumaroles are hot gas and vapor exhalations in volcanically active areas. Fumarolic gases consist predominantly of water, followed by CO<sub>2</sub> and other magmatic volatiles such as H<sub>2</sub>S, SO<sub>2</sub> and HCl (Fischer et al., 1997; Fischer and Chiodini, 2015). The temperatures of the emitted gases vary from low-temperature fumaroles (T ~ 100 °C) to high-temperature fumaroles with temperatures between 500 and 900 °C (Connor et al., 1993; Capasso et al., 1997; Hedenquist et al., 2018; Pirajno, 2020). Fumaroles that mainly emit sulfuric gases, which can be easily oxidized to native sulfur and/or sulfuric acid, are called solfatara (Schoen and Rye, 1970; Bogie et al., 2005).

Hot springs often occur together with fumaroles. These springs are pools whose water temperature is higher than the surrounding air (around 37 °C and higher; Pentecost et al., 2003; Rosli et al., 2022). The water is hydrothermally heated by a shallow magma intrusion or by convective circulation (Pirajno, 2020). The water of hot springs is often brightly colored due to abundant microbial communities (Figure 1.1). The (geo-)chemical composition of hot spring deposits is dominated by carbonates and silicates, but depends on the environment of the springs and the composition of ascending fluids (Des Marais and Walter, 2019). Calc-sinter and travertines can be found as a result of rising fluids interacting with carbonate rocks. The acid-sulfate fluids (formed by the oxidation of H<sub>2</sub>S to H<sub>2</sub>SO<sub>4</sub>) dissolve the calcium carbonates on their way to the surface, where the carbonates are deposited as calcite, leading to the formation of travertines (Fouke, 2001; Des Marais and Walter, 2019). The formation of siliceous sinter is different from the calc-sinter precipitation. The solubility of silica is strongly temperature-dependent, so hot spring waters become supersaturated in silica as they cool (Chan, 1989; Trewin and Fayers, 2005). Through several intermediate steps, siliceous sinter is finally formed.



**Figure 1.1.** Hot spring Doublet Pool with siliceous sinter deposits and benthic microbial communities in the Yellowstone National Park, USA (Des Marais and Walter, 2019).

Geysers, fumaroles and hot springs are only the surface phenomena of hydrothermal processes, which mainly take place in the sub-surface and can be the reason for the formation of mineral (ore) deposits. There are several different types of continental deposits (e.g., Skarn deposits, sedimentary exhalative deposits, volcanic-hosted massive sulfide deposits), of which two examples will be explained in more detail: porphyry Cu(-Au) deposits and epithermal (Au) systems.

Epithermal mineral deposits are formed from diluted ( $< 5$  wt% NaCl) hot waters in shallow crustal levels. The water is heated by a shallow magma intrusion and thus reaches temperatures between 50 and 300 °C. These rising hot waters are able to leach metals from the surrounding volcanic rock and may even carry dissolved gold. Due to fluid mixing and oxidation processes, mineralization occurs relatively close to the surface ( $< 1$  km depth) mainly in veins and in the breccia and stockwork zone, where such minerals may fill existing pore spaces (Hedenquist et al., 2000).

In epithermal deposits, two different mineralization types can be distinguished: high-sulfidation and low-sulfidation (e.g., Hedenquist et al., 2000; Resing et al., 2007; Tun et al., 2015). In particular, these terms refer to the oxidation state of dissolved sulfur in the fluids as well as to the fluid composition, pH, and alteration stage of the volcanic host rock (Cooke and Simmons, 2000; Hedenquist et al., 2000; Resing et al., 2007; Tun et al., 2015). High-sulfidation systems are characterized by low pH and oxidized sulfur species, especially  $\text{HSO}_4^-$  and  $\text{SO}_2$ , and occur relatively close to or directly inside the volcanic crater (Cooke and Simmons, 2000; Robb, 2005; Resing et al., 2007). Copper and arsenic sulfides like covellite, enargite and luzonite as well as pyrite are typical sulfides in such systems together with advanced argillic alteration assemblages (including quartz, alunite, clays plus native sulfur), indicating alteration of the host rock through acid-sulfate fluids (Hedenquist et al., 2000; Resing et al., 2007). Low-sulfidation systems, by contrast, are dominated by reduced fluids ( $\text{HS}^-$ ,  $\text{H}_2\text{S}$ ) with near-neutral pH and are commonly found in distal settings of volcanic activity, resulting in lower temperatures compared to high-sulfidation systems (Figure 1.2). Typical sulfide assemblages are (arseno-)pyrite, pyrrhotite and Fe-rich sphalerite (Hedenquist et al., 2000). Hot springs and fumaroles may be present in low-sulfidation deposits that are not deeply eroded.

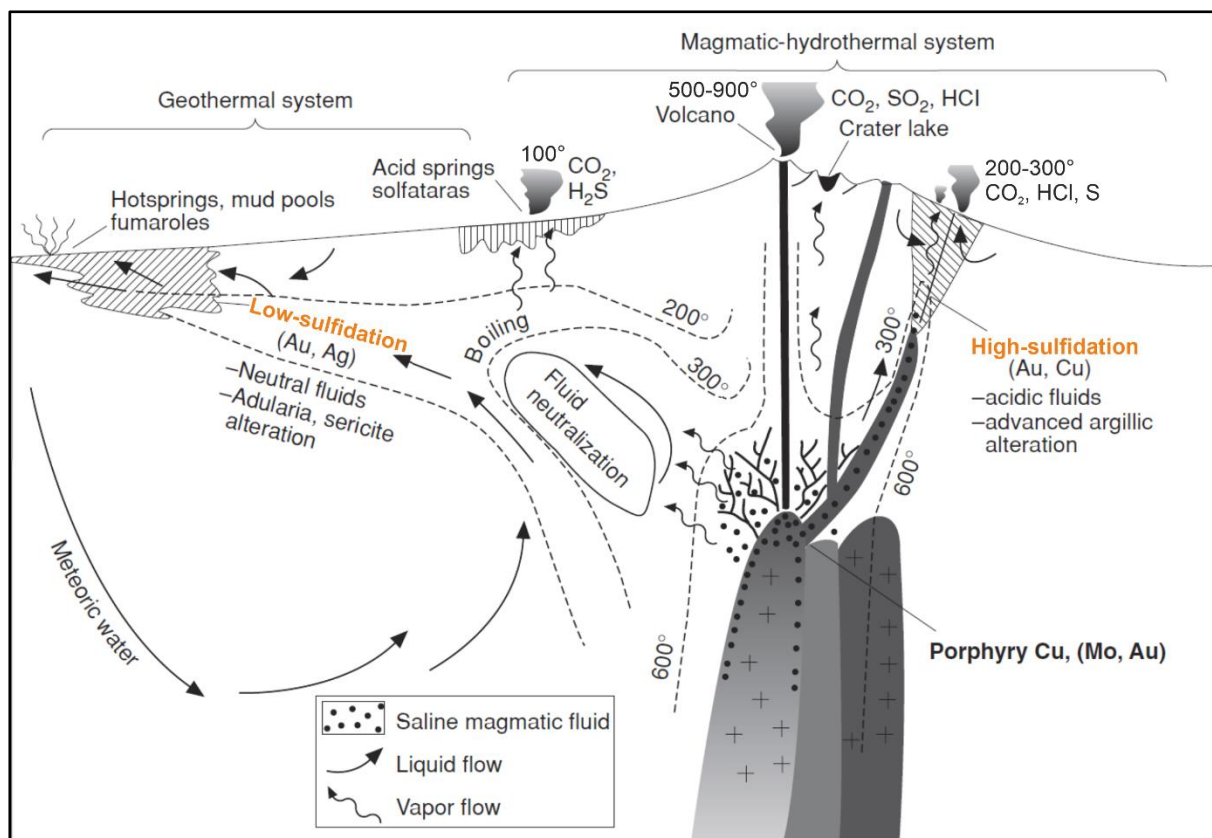


**Figure 1.2.** Schematic drawing of subaerial hydrothermal systems with high- and low-sulfidation mineralization types of epithermal ore deposits (Hedenquist et al., 2000; Robb, 2005). Porphyry Cu(-Au) deposits can occur beneath epithermal deposits.



## 1.2 Submarine hydrothermal systems

Submarine hydrothermal systems occur mainly at active plate boundaries either at mid-ocean ridges (MORs) or in arc/back-arc environments of subduction zones. The most active submarine hydrothermal sites are located in the Pacific Ocean (e.g., along the East Pacific Rise, the Kermadec arc and the Izu-Bonin-Mariana arc) and along the Mid-Atlantic Ridge in the Atlantic Ocean (Figure 1.4).

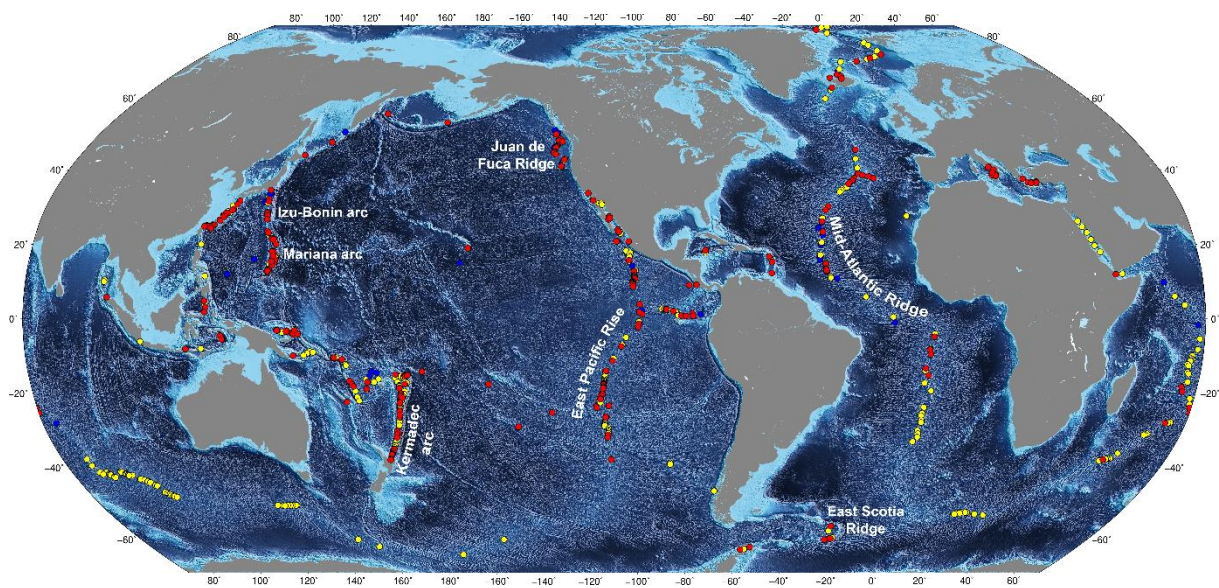


**Figure 1.4.** Overview map of all known submarine hydrothermal systems. Red dots indicate active submarine hydrothermal systems, while yellow dots reveal unconfirmed locations (modified after Beaulieu and Szafranski, 2020).

In general, submarine hydrothermal processes describe the circulation of seawater that penetrates the seafloor through initial pathways, e.g., faults and fissures. On its way through the ocean crust, the seawater is heated up to temperatures  $> 400\text{ }^{\circ}\text{C}$  by the underlying magma. The heat triggers chemical reactions between the circulating water and the surrounding rock, causing chemical alteration of both. The resulting hot and typically acidic fluids then rise back to the seafloor where they discharge as hydrothermal vents. Depending on the fluid composition, immediate chemical reactions can be seen as black, white or different-colored smoke due to the reaction of discharging hot hydrothermal fluids with cold ambient seawater.

Commonly, two main types of submarine hydrothermal systems are distinguished: seawater-rock-dominated hydrothermal systems, typically associated with MORs, and magmatic-hydrothermal systems, which mainly occur in arc and back-arc environments (Reeves et al., 2011; de Ronde and Stucker, 2015; Seewald et al., 2015; de Ronde et al., 2019). Both

hydrothermal systems are characterized by different fluid types, which leads to differences not only in temperature, pH and fluid composition, but also in mineralization.

### 1.2.1 Seawater-rock-dominated hydrothermal systems

Seawater-rock-dominated hydrothermal systems are dominated by seawater-derived fluids, as the name suggests. Typical minerals, e.g., clay minerals, quartz, and opaline silica as well as Cu- and Zn-rich sulfides can precipitate as a result of conductive cooling of the hydrothermal fluids or cooling due to seawater mixing (de Ronde et al., 2005; de Ronde and Stucker, 2015; McDermott et al., 2018; Seewald et al., 2019). Those sulfides can form typical black smoker chimneys that are characteristic for seawater-rock-dominated systems (Figure 1.5), especially at MORs. In general, seawater-derived fluids contain reduced sulfur species (e.g., H<sub>2</sub>S) and are enriched in dissolved metals. The fluids are characterized by pH-values around 3 and temperatures exceeding 300 °C. However, diffuse venting with lower temperatures of < 70 °C can also occur.

Seawater-derived fluids are a result of seawater penetrating the seafloor, which migrates down through fractures and faults until it gets heated by thermal energy from the underlying magma. Higher temperatures and exchanges of elements/ions between fluids and the surrounding host rock cause the seawater to become chemically altered on its way through the Earth's crust. Eventually, the modified seawater-derived fluid becomes buoyant so that it starts rising back up. During its ascent, it gets in interaction with the surrounding rock until the fluid is finally expelled at the seafloor as hydrothermal vent. Furthermore, mineral precipitation takes place, forming mounds or chimneys on the seafloor as a result of sulfide and sulfate accumulation.

To go into more detail, percolating seawater at hydrothermal vents undergoes several stages during its descent and subsequent ascent back to the seafloor. Cold seawater of typically 2 °C penetrates the seafloor, where it becomes increasingly heated with depth, leading to chemical alteration of the surrounding rock. At temperatures of ~60 °C, especially plagioclase and olivine are altered to Fe-micas, Fe-oxyhydroxides and smectite ("recharge zone", Figure 1.5; von Damm et al., 1985; Tivey, 2007). With increasing temperatures and due to precipitation of Mg-bearing minerals, Mg is removed from the already modified and downward-migrating seawater (Mg = 0 in end-member fluid; von Damm, 1990; Gamo et al., 1997; Wilckens et al., 2019). Calcium and sulfate are also removed from this seawater-derived fluid at temperatures > 150 °C caused by anhydrite precipitation (end-member fluid contains near-zero sulfate; Tivey, 2007; de Ronde and Stucker, 2015; Stucker et al., 2017). Another process that occurs within the deeper recharge zone is the reaction of fluid with Fe-bearing minerals, resulting in reducing conditions. In the deep reaction zone, the reduced fluids are able to leach metals such as Cu, Fe, Zn as well as sulfur from the volcanic rock. When temperatures start to exceed

400 °C, the fluid reaches such a high buoyancy that it swiftly rises back to the seafloor (“upflow zone”, Figure 1.5). Simultaneous magma degassing can cause mixing of the ascending fluid and magmatic volatiles (e.g., SO<sub>2</sub>, CO<sub>2</sub> and other trace gases; Resing et al., 2004; Seewald et al., 2015). At MORs, however, magmatic volatiles have not such a great influence on the vent fluid composition as it is the case in arc and back-arc systems described below. Due to the higher ambient pressure at depth severely elevating the boiling point of water, the decreasing pressure of the upward-moving fluid and its consistently high temperature can cause the seawater to boil, resulting in phase separation of the fluid into a high-salinity liquid phase and a low-salinity volatile-enriched vapor phase (Butterfield et al., 1994; Tivey, 2007; Seewald et al., 2015; Stucker et al., 2017; Seewald et al., 2019). Finally, the hot and metal-enriched fluids reach the seafloor where they discharge as hydrothermal vent fluids with temperatures that can easily exceed 300 °C. Mixing of these discharged fluids with ambient cold seawater results in chemical reactions and mineral precipitation, which can be seen as black smoker chimneys on the seafloor (Figure 1.5).

Evidence of phase separation is seen in the Cl<sup>-</sup> concentration of the discharging fluids because it either exceeds the chloride concentration of seawater or is less than that. Moreover, phase separation does not only affect fluid salinity but also metal concentration of the fluids. Chloride complexes are important transport agents for metal ions and are therefore important for mineral precipitation (von Damm, 1990; Hannington et al., 1995; Tivey, 2007). Despite the precipitation of anhydrite at temperatures > 150 °C, Ca<sup>2+</sup> is found in hydrothermal fluids discharging at the seafloor, which is due to the fact that calcium (along with potassium and sodium) is leached from the surrounding host rock and added to the fluids (Tivey, 2007; Wilckens et al., 2019).

The most well-known sites of MOR hydrothermal systems are the East Pacific Rise (EPR) 21°N fields, Southern Juan de Fuca Ridge hydrothermal vents and the Trans-Atlantic Geotraverse (TAG) field at the Mid-Atlantic Ridge. Although most of these locations are known for the occurrence of black smokers, the TAG hydrothermal field is special. Here, next to the “common” black smoker chimneys, white smokers occur on the SE edge of the lower platform in the so-called Kremlin area (Thompson et al., 1988; Humphris et al., 2015). The white smoker fluids here, however, are formed as a result of mixing black smoker fluids with seawater (Humphris and Tivey, 2000; Humphris et al., 2015), unlike the formation of the white smoker fluids associated with arc and back-arc systems as described below.

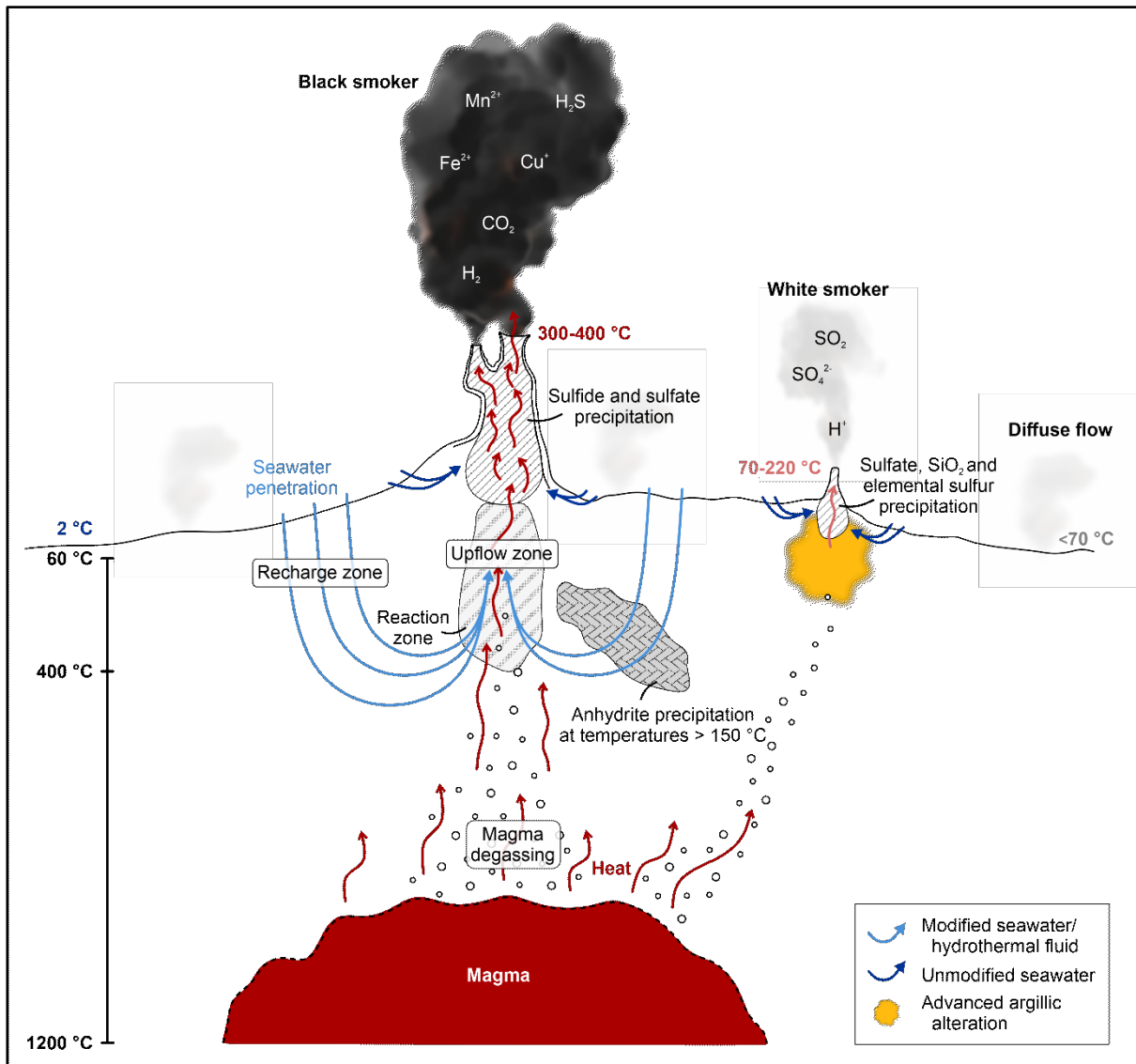


**Figure 1.5.** Schematic drawing showing the principals of subseafloor hydrothermal processes and the formation of black and white smoker. Black smokers typically characterize seawater-rock-dominated hydrothermal systems (especially at MORs, but also in arc/back-arc environments), while white smokers are a common phenomenon of magmatic-hydrothermal systems. Black smoker fluids are high-temperature seawater-derived hydrothermal fluids with moderately acid pH-values of 3 to 4. The chimneys were mainly made of sulfide minerals as well as sulfates, building the outer wall. Acid-sulfate fluids of magmatic-hydrothermal systems are highly acidic (pH ≤ 1) and have lower temperatures (mainly ~100 °C, but also higher temperatures are known) compared to seawater-derived fluids. Metal sulfides are typically not found in acid-sulfate precipitates because convective circulation of seawater-derived hydrothermal fluids is missing and hence metals were not leached from the surrounding rock.

### 1.2.2 Magmatic-hydrothermal systems

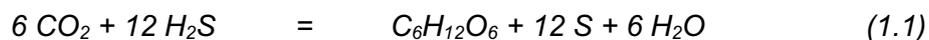
In contrast to seawater-rock-dominated hydrothermal systems, magmatic-hydrothermal systems are characterized by a direct input of magmatic volatiles and the absence of metal sulfides due to the missing circulation of seawater-derived fluids (Figure 1.5). Magmatic-hydrothermal systems are associated with the formation of elemental sulfur on the seafloor and advanced argillic alteration mineral assemblages in upflow zones, leading to venting of

acid-sulfate fluids typically seen as white smokers (Seewald et al., 2015; Seewald et al., 2019; Wilckens et al., 2019). Acid-sulfate fluids are metal-poor, usually depleted in Na and K, and dominated by oxidized sulfur species, e.g., SO<sub>2</sub> and HSO<sub>4</sub><sup>-</sup>. They are generally cooler than seawater-derived fluids with temperatures ≤ 220 °C. Due to the direct magmatic input and disproportionation of magmatic SO<sub>2</sub>, the fluids are highly acidic with pH-values as low as < 1 (Butterfield et al., 2011; Seewald et al., 2015). The process of disproportionation is described in more detail in the subchapter 1.4.

Examples of familiar submarine arc/back-arc hydrothermal systems are Brothers volcano in the Kermadec arc, Niuatahi volcano (also known as MTJ-1 caldera or Volcano O) in the NE Lau Basin, DESMOS caldera in the Eastern Manus Basin and the Niuia volcanic edifice (Niuia North) located in the NE of Niuatahi. What they all have in common is the occurrence of elemental sulfur, which was always ascribed to the disproportionation of magmatic SO<sub>2</sub> (eq. 1.3) as the most commonly observed process of sulfur formation (e.g., de Ronde et al., 2005; de Ronde et al., 2011; Seewald et al., 2019).

### 1.3 Life at hydrothermal vents

Hydrothermal vents are some of the most extreme environments on Earth and even if they appear to be hostile (to humans), they are in fact veritable oases of life in the deep sea. A variety of species have adapted to life under extreme conditions without sunlight, which is possible due to chemosynthesis. Unlike photosynthesis, where energy is produced from sunlight, chemosynthesis produces energy from inorganic compounds such as methane, carbon dioxide or dissolved sulfur species, all of which derive from hydrothermal fluids. A general equation for chemosynthesis is given by eq. 1.1:



The base of hydrothermal vent fauna are autotrophic bacteria, which receive their energy directly from the inorganic compounds and convert them into essential organic matter through chemical reactions. Autotrophic bacteria are often found as large white or yellowish mats covering the seafloor around hydrothermal vents. These bacteria can also live in the sub-surface or even on the surface of or within other vent animals as microbial symbionts (ecto- and endosymbiosis; Polz and Cavanaugh, 1996). In case of the latter, both the bacteria and the host animal, e.g., tube worms and bivalves, benefit from this relationship because the host supplies important inorganic nutrients, while the bacteria provide the host animal with energy in the form of food (Hessler and Kaharl, 1995; Polz and Cavanaugh, 1996; Newton et al., 2007). Examples of vent fauna animals are tube worms, vent crabs (e.g., *Kiwa* genus), anemones and giant clams (e.g., *Calyptogena magnifica*, which was discovered together with

the first deep-sea hydrothermal vents in the Galápagos Rift in 1977), which especially cluster around black smokers (Figure 1.6) (Newton et al., 2007; Thatje et al., 2015; Linse et al., 2019).

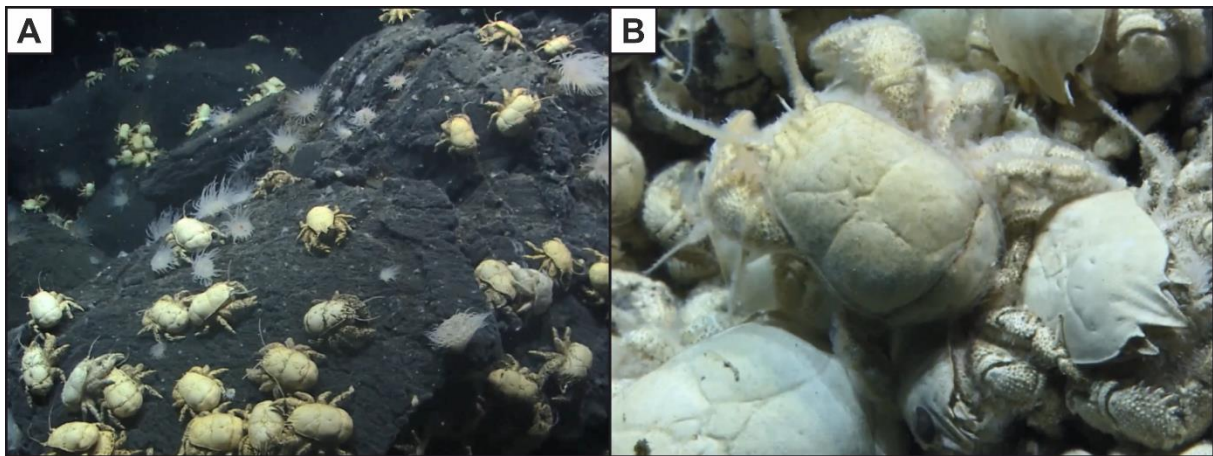


**Figure 1.6.** A) Vent crabs *Kiwa tyleri* and anemones close to a black smoker vent field of the East Scotia Ridge segment E2, and B) Close-up picture of a *Kiwa* crab. The white fluff on the surface of the animals are autotrophic bacteria. Photos were taken during ROV dives on the PS119 cruise.

Another type of vent bacteria are heterotrophic bacteria, which also occur in hydrothermal environments. In contrast to the autotrophic bacteria, they depend on organic (rather than inorganic) matter as material for their body substance and are therefore dependent on other living organisms (Hessler and Kaharl, 1995).

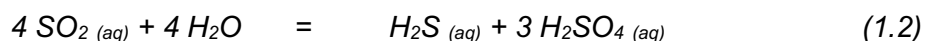
#### 1.4 Mineral deposits and processes at hydrothermal vents

Hydrothermal deposits currently forming on the seafloor are quite complex, but can be in general divided into seawater-rock-dominated hydrothermal systems and magmatic-hydrothermal systems, as abovementioned. In seawater-rock-dominated hydrothermal systems, sulfides may be deposited as single chimneys (cm to > 10 m high) or as expansive mounds covering wide areas of the seafloor (between several meters and > 100 m) (Embley et al., 1988; Scott et al., 1995). Black smoker chimneys form from sulfate and metal sulfide precipitation when hydrothermal fluids discharge at the seafloor and cool as a result of mixing with ambient seawater. Such chimneys typically grow in a zonation pattern starting with the precipitation of barite and/or anhydrite (i.e., sulfates) as low-temperature mineral phases (Graham et al., 1988; Neukirchen and Ries, 2014). The resulting “sulfate walls” protect the hydrothermal fluid from intense seawater mixing and thus from rapid cooling (cf. Berkenbosch et al., 2012). Due to continuous fluid flow and dissolution from the outside, however, the sulfates are gradually dissolved, giving way to subsequent mineral precipitates forming inside the protective barite/anhydrite walls. A typical sulfide sequence from outside to inside is

marcasite and wurtzite, pyrite and sphalerite, bornite (associated with chalcocite and covellite) and chalcopyrite (Haymon, 1983; Graham et al., 1988; Tivey, 1995; Berkenbosch et al., 2012). As this sequence would suggest, the higher temperatures in the center of the chimney (up to > 350 °C) allows the precipitation of high-temperature Cu-bearing mineral assemblages (Tivey, 2007).

The innermost parts of typical chimneys especially at mid-ocean ridge hydrothermal vent sites are largely characterized by chalcopyrite, enveloped by a bornite layer (Haymon, 1983). This has also been noted for some chimneys growing at the Brothers NW Caldera vent site (Berkenbosch et al., 2012). At the margin of this chalcopyrite-dominated zone, replacement of chalcopyrite by bornite can occur (Zhao et al., 2014b). Bornite itself can alter relatively easily to intermediate phases such as chalcocite and covellite and then to azurite and malachite. Due to more oxidizing conditions at the chimney's exterior, replacement and exsolution processes can more readily take place. Thus, between the chalcopyrite zone and the Fe- and Zn-enriched outer layer, bornite is commonly replaced by chalcocite and covellite (Graham et al., 1988; Berkenbosch et al., 2012). The outermost layer of sulfide minerals is dominated by pyrite, colloform marcasite and sphalerite, which locally can replace sulfates (de Ronde et al., 2003; de Ronde et al., 2011; Berkenbosch et al., 2012).

Acid-sulfate type fluids in magmatic-hydrothermal systems on the other hand are typically associated with the formation of elemental sulfur by disproportionation of magmatic SO<sub>2</sub>. Due to disproportionation, reduced (S<sup>0</sup> or H<sub>2</sub>S) and oxidized (SO<sub>4</sub><sup>2-</sup>) sulfur species are generated, resulting in the formation of sulfuric acid and thus fluids with pH-values down to 1 (de Ronde et al., 2005; de Ronde et al., 2011; Seewald et al., 2019). The disproportionation reactions can be described as follows:



Elemental sulfur (and H<sub>2</sub>S) formed by SO<sub>2</sub> disproportionation generally shows negative δ<sup>34</sup>S values (< 0 ‰), which are common values for elemental sulfur in magmatic-hydrothermal systems. As a result of a kinetic δ<sup>34</sup>S isotope effect, <sup>34</sup>S-depleted native sulfur (or H<sub>2</sub>S) and <sup>34</sup>S-enriched sulfate are produced compared to the influxing SO<sub>2</sub> (Kusakabe et al., 2000; McDermott et al., 2015).

The Kemp Caldera system, which is discussed in more detail in this thesis, is different from other hydrothermal systems in which elemental sulfur is formed. The peculiarity of the Kemp Caldera is the isotopically heavy sulfur that cannot result from the common disproportionation reaction.

## 1.5 Stable isotopes in hydrothermal systems

Since the development of isotope ratio mass spectrometry in the middle of the 20<sup>th</sup> century, this technique has been increasingly used in geochemistry to measure stable isotopes in a wide variety of environments on Earth. An isotope ratio mass spectrometer has the capability to measure variations in isotope ratios, even if they are very small. In nature, such isotope variations occur because of biological, chemical or physical processes resulting in isotope fractionation. This means that isotopes were partitioned between species/phases of the same element (e.g., hydrogen, oxygen, carbon, or sulfur) with a different isotope ratio (Shanks et al., 1995). Isotope fractionation can be expressed in general with the equation:

$$\alpha_{x-y} = \frac{1000 + \delta_x}{1000 + \delta_y} \quad (1.4)$$

where  $\alpha$  is the fractionation factor describing equilibrium isotopic partitioning and  $\delta$  indicates the deviation from a standard resulting from small variations in isotope ratios (Figure 1.7).

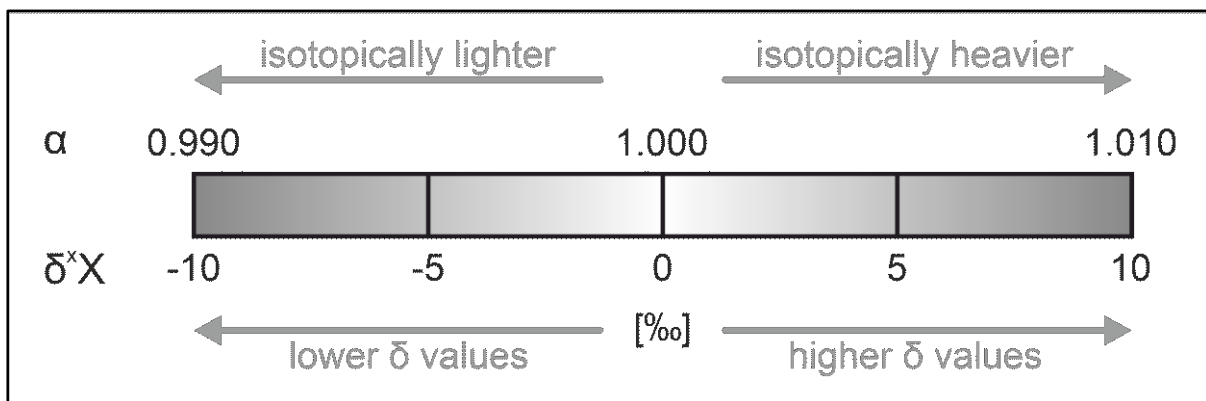


**Figure 1.7.** Schematic drawing of the  $\alpha$ - and  $\delta$ -scale used for the expression of stable isotope ratio values (modified after Shanks et al., 1995).

Based on isotope fractionation or different isotope ratios it is possible to determine the origin of an element involved in the formation of a mineral or to infer the formation process of a mineral. In case of sulfur species normally occurring in hydrothermal systems (which is explained in more detail in chapter 4), the mean  $\delta^{34}\text{S}$  value of MORB is around 0 ‰, while arc lavas are  $^{34}\text{S}$ -enriched and show  $\delta^{34}\text{S}$  values between 4 and 10 ‰ (Hannington et al., 2005; Labidi et al., 2012; McDermott et al., 2015). However, elemental sulfur formed by  $\text{SO}_2$  disproportionation (eq. 1.3) in arc/back-arc environments or at mid-ocean ridges show negative  $\delta^{34}\text{S}$  values of down to  $-9$  ‰ (de Ronde et al., 2005; McDermott et al., 2015; Peters et al., 2021). This is attributed to sulfur isotope fractionation between different sulfur species during the disproportionation reaction or other (sulfur) formation processes. In contrast to the negative sulfur values of  $\text{S}^0$ , sulfate in hydrothermal environments, e.g., sulfate minerals such as

anhydrite and barite, mainly concentrates around the value of seawater sulfate ( $\delta^{34}\text{S}_{\text{SO}_4} = 21 \pm 1 \text{ ‰}$ ; Herzig et al., 1998; Present et al., 2020). Oxidation of isotopically lighter sulfide minerals or  $\text{H}_2\text{S}$  of the vent fluids results in  $\delta^{34}\text{S}$  values lower than seawater sulfate, while seawater sulfate local hydrothermal reduction associated with  $^{34}\text{S}$  enrichment of the residual sulfate leads to values  $> 21 \text{ ‰}$  (Shanks et al., 1995).

## 1.6 Geologic setting and study area of the Kemp Caldera

The Kemp Caldera, like Niutahi or Brothers volcano, is a submarine arc caldera volcano. It was discovered during a geophysical survey on the research cruise JR224 of the R/V *James Clark Ross* in 2009 (Larter, 2009; Cole et al., 2014). The Kemp Caldera belongs to the southernmost part of the South Sandwich island arc, situated in the Scotia Sea (Figure 1.8). The Scotia Sea area is located in the southernmost part of the Atlantic Ocean and comprises four tectonic plates. The Sandwich micro-plate is the smallest one, enclosed by the Scotia Plate in the west, the South American Plate in the north and east, and the Antarctic Plate in the south (Leat et al., 2000; Pearce et al., 2000; Barker, 2001).

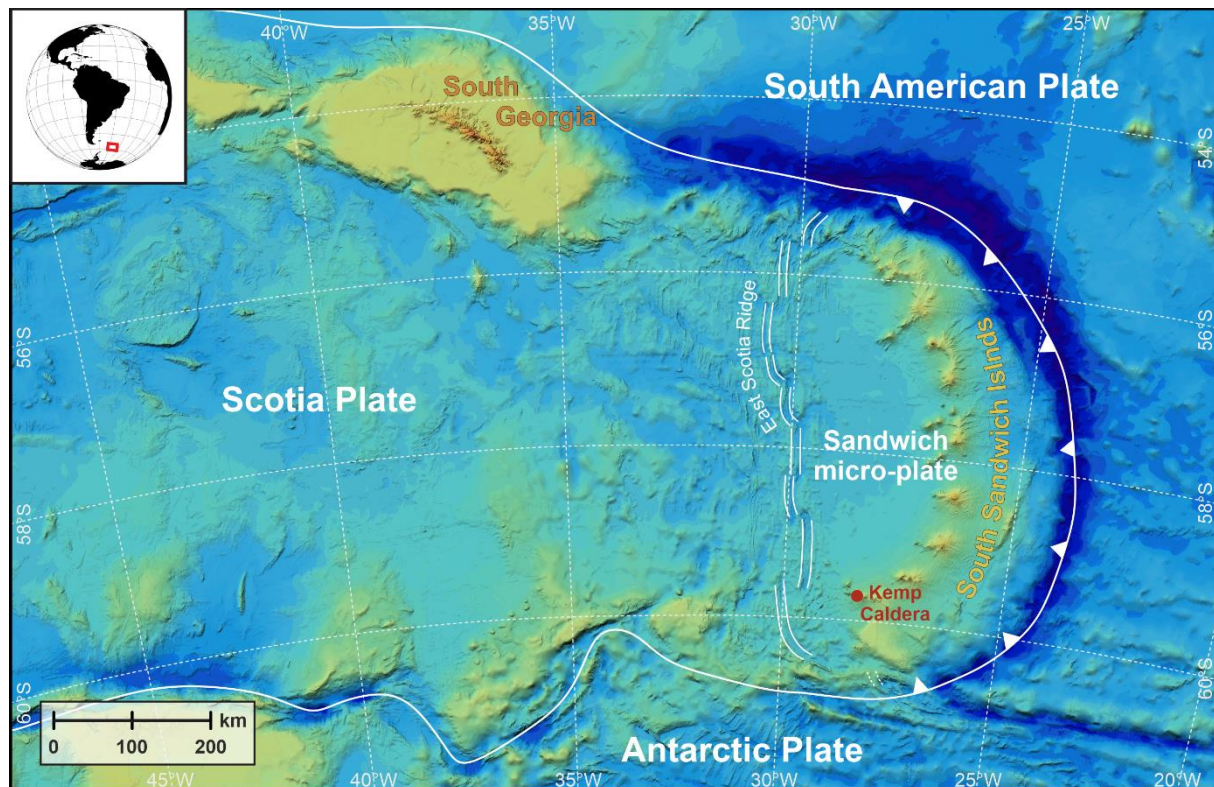


**Figure 1.8.** General map of the Scotia Sea area and the location of the Kemp Caldera. The caldera belongs to the submerged part in the south of the South Sandwich island arc.

The intra-oceanic East Scotia Ridge as an active spreading center is situated to the west of the Sandwich micro-plate and separates the Sandwich plate and the Scotia plate (Bruguier and Livermore, 2001; Larter et al., 2003; Leat et al., 2016). This spreading (current intermediate spreading rate averages 65 to 70 mm/a) was initiated ~15 Ma ago and is associated with the subduction zone to the east of the Sandwich micro-plate, where it overrides the subducting South American Plate (German et al., 2000; Bruguier and Livermore, 2001; Cole et al., 2014). The East Scotia Ridge consists of nine ridge segments (E1 to E9 from north to south) and an anomalous tenth segment E10 that is located at the southern edge of the Sandwich micro-plate (Leat et al., 2000; James et al., 2014). Several hydrothermal vent fields occur along the East Scotia Ridge. The most active sites with actively venting chimneys (e.g. Dog's Head, Sepia, Black & White, Ivory Towers and Pagoda) are known from the ridge segments E2 and E9 (cf. German et al., 2000; Livermore, 2003; Cole et al., 2014; James et al., 2014). The lithosphere that is formed on this intra-oceanic ridge is of basaltic and basalt-andesitic composition (Fretzdorff et al., 2002; Leat et al., 2004; Cole et al., 2014).

The South Sandwich Trench represents the eastern border of the Sandwich micro-plate. The trench developed as a result of the (still ongoing) subduction of the westward moving (ca. 70 to 85 mm/a) South American Plate underneath the overriding Sandwich micro-plate (Pearce et al., 2000; Fretzdorff et al., 2002). The active transform plate boundary between the South American Plate and the Antarctic Plate marks the southern end of the South Sandwich Trench. Here, the trench is shallower than in the north, which is caused by the age difference of the oceanic lithosphere. Older, stiffer lithosphere (~80 Ma) is subducted in the northern part, resulting in a steep dip angle of the subducting plate and a trench depth of more than 8 km, compared to much younger, warmer crust (~27 Ma) in the south, resulting in a depth of only < 7 km (Leat et al., 2004; Barry et al., 2006; Leat et al., 2010; Leat et al., 2016). The subducting slab dehydrates, which initiates partial melting of the overlying mantle wedge, giving rise to the South Sandwich island arc formation. The lithology of the intra-oceanic arc and the islands itself has a basaltic to rhyolitic composition and belongs to magma series ranging from (low-K) tholeiitic to calc-alkaline (Larter et al., 1998; Leat et al., 2004; Barry et al., 2006).

So far, it has been assumed that the lithology of the Kemp Caldera is the same as that of the neighboring Kemp Seamount, which mainly consists of basaltic andesite and tholeiitic basalt (Leat et al., 2004; Leat et al., 2013; Cole et al., 2014). However, analyses of rock samples taken during the R/V *Polarstern* expedition PS119 in 2019 indicate that the volcanic rock is of a more siliceous composition (see chapter 3, Manuscript I).

A detailed description of the Kemp Caldera, its morphology and a description of the hydrothermally active sites within the caldera is given in chapter 3.

## 2 MOTIVATION AND OBJECTIVES

Submarine hydrothermal systems have fascinated scientists since their discovery in the 1970s. Due to the variety of hydrothermal systems across different settings and their interest for a large number of disciplines, scientists have strived to study the processes that are characteristic for such systems. A unique form of hydrothermal systems are submarine calderas, which remain poorly understood in terms of their formation and development over time. Despite years of intensive research, we still have a very rudimentary knowledge of many of the processes, so that each newly discovered hydrothermal system contributes to a better understanding of those systems.

Within the scope of my PhD, I participated in the R/V *Polarstern* PS119 research cruise to the Eastern Scotia Sea in 2019. One of the goals of this research cruise was a general investigation of the Kemp Caldera, one of the largest submarine volcanic structures of the South Sandwich island arc. This submarine arc caldera volcano was discovered 13 years ago and, since then, has been studied intensively from a biological point of view. However, it is important to gain better knowledge and insights into all processes that are responsible for the formation, its development and the current (hydrothermal) activity of the Kemp Caldera. I therefore focused on some of the geologic questions associated with the Kemp Caldera hydrothermal system in order to provide new information on the hydrothermal and thermodynamic processes of both the caldera and arc/back-arc hydrothermal systems in general.

The purpose of this work is to expand the knowledge of the Kemp Caldera (hydrothermal) system, as an example of submarine arc/back-arc hydrothermal systems. This caldera is one of the least explored submarine calderas. Its formation is still fairly unknown whereas only assumptions have been made about its rock composition. Changes in temperature and hydrothermal activity observed at the Kemp Caldera floor since the R/V *James Cook* JC42 expedition in 2009/2010 are associated with changes of volcanic activity at depth, which means that the caldera is still (volcanically) active. During my research, I came across rather uncommon mineral associations and the special feature of isotopically heavy sulfur in the central vent fields of the Kemp Caldera. The formation of this elemental sulfur could not be explained by the common sulfur formation processes, e.g., SO<sub>2</sub> disproportionation or SO<sub>4</sub> reduction. Hence, the behavior of sulfur in arc and back-arc hydrothermal systems regarding sulfur formation and its isotopy is probably more complex than previously thought. This, as well as the morphology and development of the Kemp Caldera hydrothermal system is described further in the following chapters.

### 3 MANUSCRIPT I

## THE KEMP CALDERA, THE SOUTHERNMOST ARC CALDERA VOLCANO FROM THE SOUTH SANDWICH ISLAND ARC – NEW RESULTS FROM SEAFLOOR INVESTIGATIONS

Victoria Kürzinger<sup>1,2</sup>, Miriam Römer<sup>1,2</sup>, Anna Lichtschlag<sup>3</sup>, Gerhard Bohrmann<sup>1,2</sup>

<sup>1</sup> MARUM Center for Marine Environmental Sciences, University of Bremen, Leobener Straße 8, 28359 Bremen, Germany

<sup>2</sup> Faculty of Geoscience, University of Bremen, Klagenfurter Straße 2-4, 28359 Bremen, Germany

<sup>3</sup> National Oceanography Centre, European Way, Southampton SO14 3ZH, UK

### In preparation for submission

---

#### Abstract

In 2009, a submarine caldera volcano in the south of the South Sandwich island arc (Scotia Sea) was discovered during the R/V *James Clark Ross* research cruise JR224. At this time, also hydrothermal activity was recorded within the now named Kemp Caldera. Since then, the focus has been primarily on biological studies. To get more information about the morphology, petrology and the formation of the Kemp Caldera, further investigations were made during the R/V *Polarstern* cruise PS119 in 2019. Ship's multibeam data were collected to get an overview of the caldera bathymetry and backscatter characteristics. Furthermore, OFOBS and ROV dives were deployed for detailed visual investigations of the hydrothermally active sites Vent field at the central resurgent cone and Flare site at the NNW caldera rim. During ROV dives, rock samples were collected from the cone providing first information about the Kemp Caldera rock composition. The caldera rocks are not basaltic or andesitic as the rocks from the neighboring Kemp Seamount, but have a dacitic composition. This suggests that the dacitic cone was formed by a later eruption of differentiated magma, providing information about the formation of the caldera and its current processes.

*Keywords:* Kemp Caldera, visual investigations, hydrothermally active sites, dacitic rock composition

---

### 3.1 Introduction

The development of marine technologies (including, e.g., acoustic and towed camera systems, robots and geophysical methods) in the last decades enabled the collection of huge amounts of seafloor data and thus mapping of large submarine areas. Multibeam and single beam echosounders are the most commonly used systems for seafloor mapping. The transmitted acoustic signals are processed to result bathymetric maps, which enable structural and geological interpretations. The development of higher resolution of newly acquired bathymetric data can provide more detailed information about an area, allowing identification of small-scale changes over time. Thus, seafloor mapping is not only applied as a tool to explore new areas, but also for routine surveys to investigate known areas for changes over time.

During the research cruise JR224 of the R/V *James Clark Ross* in 2009, new multibeam swath bathymetry data were collected as well as routine surveys were conducted. A highlight of the new collected multibeam survey data was the discovery of the previously unknown submarine Kemp Caldera west of Kemp Seamount (Larter, 2009). Sites of hydrothermal activity in the Kemp Caldera (formerly known as McIntosh Crater or McIntosh Caldera) were observed during video footage taken on the JR224 cruise and the follow-up JC42 research cruise of the R/V *James Cook* in 2010 (Larter, 2009; Rogers, 2010; Cole et al., 2014). Note that based on morphological criteria (e.g., aspect ratio, flat bottom, steep walls), Kemp Caldera was identified as a caldera and not a crater. Since its discovery, the Kemp Caldera was investigated intensively from a biological point of view (see, e.g., Amon et al., 2013; Arango and Linse, 2015; Georgieva et al., 2015; Linse et al., 2019), but remains largely unknown regarding its geological history and evolution. This paper provides first petrological results from the Kemp Caldera rocks sampled during the R/V *Polarstern* PS119 cruise in 2019. Furthermore, backscatter data collected during this cruise, give insights into Kemp Caldera surface characteristics, and OFOBS and ROV dives enabled detailed descriptions of the hydrothermally active sites.

### 3.2 Geologic setting

The Kemp Caldera is a submarine arc caldera volcano located in the Scotia Sea and belongs to the southernmost part of the South Sandwich island arc. The Scotia Sea is an area located partly in the Southern Ocean and (for the greater part) in the South Atlantic. It is enclosed by the Drake Passage to the west, the Weddell Sea to the south, and the Atlantic Ocean to the east and north. Directly beneath the Scotia Sea, the Scotia Plate and the smaller Sandwich micro-plate are situated (Figure 3.1). The Scotia Plate boundary is marked by the North Scotia

Ridge, East Scotia Ridge and South Scotia Ridge to the north, east and south, respectively. To the west, the plate is bounded by the Shackleton Fracture Zone. Here, the West Scotia Ridge can also be found. This extinct spreading center, which was active between 30 Ma and 6 Ma ago, was responsible for the formation of the oceanic lithosphere of the Scotia Plate as it is the still active East Scotia Ridge (Riley et al., 2019). The intra-oceanic East Scotia Ridge, consisting of ten ridge segments, represents not only the eastern boundary of the Scotia Plate, but also the boundary of the Sandwich micro-plate to its west. Hydrothermal activity was recorded from the segments E2 in the north and E9 in the south, where hydrothermal vent fields like Dogs Head and Cindy's Castle are known (German et al., 2000; Rogers et al., 2012; James et al., 2014). Roughly 15 Ma ago, the East Scotia Ridge spreading started and has a current average spreading rate of ca. 65-70 mm/a (German et al., 2000; Cole et al., 2014). The crust is mainly made up of tholeiitic basalt and basaltic andesite (Leat et al., 2000; Fretzdorff et al., 2002).

The South Sandwich Trench represents the subduction zone to the east of the Sandwich micro-plate, where the plate overrides the subducting South American Plate (Pearce et al., 2000; Livermore, 2003; Leat et al., 2016). As a consequence of age difference, because older crust (~80 Ma) is subducted in the north than in the south (~27 Ma), the trench is much deeper in the north (> 8 km) than in the southern part (< 7 km) (Leat et al., 2004; Barry et al., 2006; Leat et al., 2010; Leat et al., 2016).

The formation of the South Sandwich island arc is also related to the subduction of the South American Plate under the Sandwich micro-plate. Due to dehydration of the down-dipping slab, partial melting of the overlying mantle wedge is initiated, which leads to the formation of the South Sandwich Islands (Leat et al., 2003; Leat et al., 2013). In total, the South Sandwich island arc consists of eleven volcanic islands and numerous seamounts (Holdgate and Baker, 1979; Barry et al., 2006). The island's lithology ranges from basalt to rhyolite, and belongs to the (low-K) tholeiitic and calc-alkaline series (Larter et al., 1998; Leat et al., 2004; Barry et al., 2006). Hydrothermally active sites are known not only from the East Scotia Ridge, but also from the island arc, in particular the Kemp Caldera in the south of the South Sandwich Islands (Larter, 2009; Cole et al., 2014). The Kemp Caldera belongs to the submerged part of the South Sandwich island arc, but is located in the rear-arc ca. 25 km west of the main volcanic arc (Larter, 2009; Cole et al., 2014; Kürzinger et al., 2022).

## The Kemp Caldera, the southernmost arc caldera volcano from the South Sandwich island arc – New results from seafloor investigations

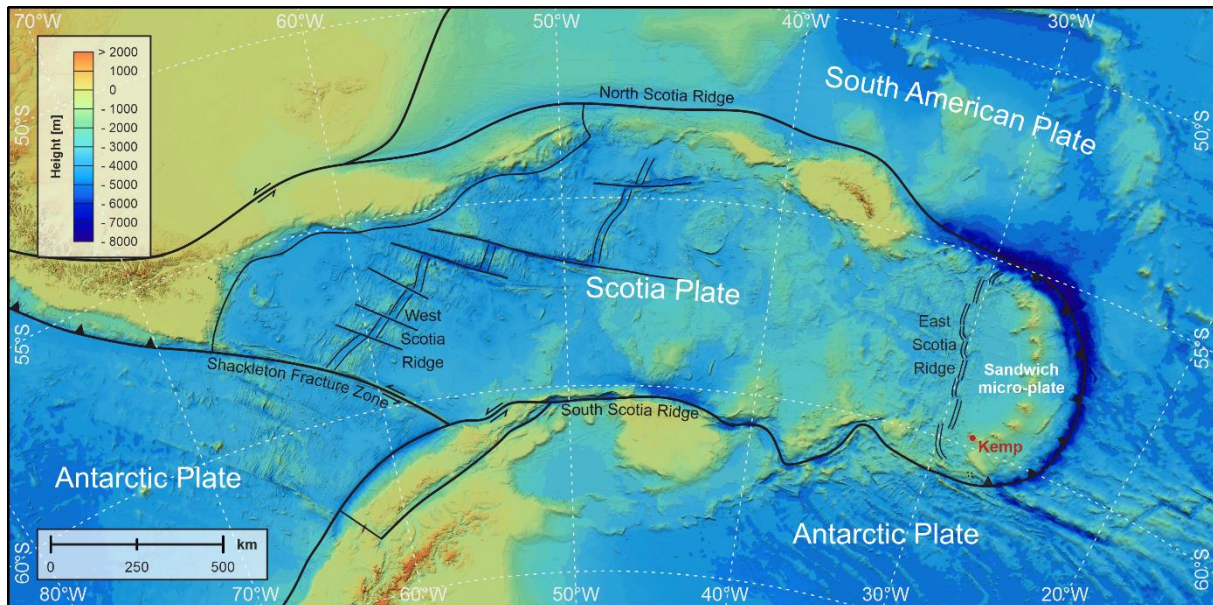


**Figure 3.1.** Bathymetric map of the Scotia Plate and its surroundings. Important tectonic features of the Scotia Sea, Scotia Plate and Sandwich micro-plate are labeled on the map. The submarine Kemp Caldera (labeled in red) is located in the south of the South Sandwich island arc on the Sandwich micro-plate.

The majority of the hydrothermal activity within the Kemp Caldera is known from the central area at the so-called Vent field (Figure 3.2A). Well described features from the area are, e.g., the Great Wall, which is a diffuse venting site named after a ca. one-meter high wall-like structure consisting of weathered rock and covered by fine-crystalline sulfur as well as microbial mats (Rogers, 2010; Cole et al., 2014; Hepburn, 2015; Linse et al., 2019; Kürzinger et al., 2022). Toxic Castle and Winter Palace are white smoker vent fields located east of Great Wall. Previously, Toxic Castle was known as diffuse flow area (Tyler, 2011; Hepburn, 2015), but nowadays, the emitting fluids reach temperatures of more than 200 °C, similar to that of Winter Palace (Cole et al., 2014; Linse et al., 2019; Kürzinger et al., 2022). An interesting phenomenon of Toxic Castle and Winter Palace is the occurrence of liquid sulfur which partly covers the chimneys (Rogers, 2010; Kürzinger et al., 2022). Moreover, at Toxic Castle a rather uncommon co-occurrence of sulfide minerals (like covellite) and elemental sulfur (Kürzinger et al., 2022) has been described. The well-shaped covellite crystals are enclosed by a sulfur matrix.

A second hydrothermal active site was discovered during the R/V *Polarstern* PS119 expedition in 2019 (Bohrmann, 2019; Thomas Pape, personal communication) at the NNW caldera rim (Figure 3.2A). Here, a bubble stream was detected in the water column as hydroacoustic anomaly (also known as “flare”). During a visual seafloor survey at this Flare site, an actively venting chimney was discovered, named Beehive Chimney, however, the gas bubble source could not be detected. The actively venting Beehive Chimney is characterized by fluid

temperatures of ~230 °C, and the relatively small chimneys found there consist mainly of barite, chalcopyrite, marcasite, and sphalerite, showing a zonation pattern similar to that observed in other black smoker chimneys (Kürzinger et al., 2022).

### 3.3 Methods

During the R/V *Polarstern* PS119 research cruise in April/May 2019, multibeam and single beam swath bathymetry surveys were conducted at Kemp Caldera (Bohrmann, 2019). For visual impressions and seafloor images, both OFOBS (Ocean Floor Observation and Bathymetry System) and ROV (Remotely Operated Vehicle) were used. Furthermore, rock sampling was enabled by the ROV (Table 3.1).

#### 3.3.1 Hydroacoustic data

Hydroacoustic data were collected during multibeam and single beam swath bathymetry surveys. Bathymetry and backscatter data were recorded with the hull-mounted *TELEDYNE HS-DS3* multibeam echosounder (MBES) at sounding frequencies between 14 and 17 kHz and is applied for water depths of 30 to ca. 8200 m. The collected data were post-processed with the open source MB-System software suite (Caress et al., 2017). The resulting grid displays high quality seafloor data with a resolution of 30 m. Backscatter data were processed with CARIS Hips&Sips. Sub-bottom profiler data were collected using the hull-mounted *TELEDYNE PARASOUND P70* echosounder. Visualization was done with IHS Kingdom Suite.

#### 3.3.2 Ocean Floor Observation and Bathymetry System (OFOBS)

To acquire seafloor images, an OFOBS was deployed. A complete list of all devices mounted at the OFOBS and its functionality is described in detail in Purser et al. (2019) in detail. In this study, the following devices were used: for visual seafloor observations, a high-resolution digital camera *iSiTEC*, *CANON EOS 5D Mark III*, equipped for still frames and a *Sony FCB-H11* HD color camera for video recording were used, and a Posidonia ultra-short baseline (USBL) transponder was used for underwater positioning. For the cleaning of outliers, smoothing and interpolation to 1 sec the software tool of Marcon (2019) was used.

### 3.3.3 The Remotely Operated Vehicle (ROV) *MARUM QUEST 4000*

The ROV *MARUM QUEST 4000* was used to collect additional seafloor images. To enhance the video imaging quality, two ultra-low latency HDTV cameras, a 4k video tiling system, a stereo camera with corrected optics and a still camera prototype (15 Mpx) were installed on the vehicle. A DVL (1200 kHz) was used to perform stationing, displacement and other automatic control functions.

Rock samples were collected from the caldera floor using the ROV (Table 3.1). With its hydraulic manipulator arm, the rock samples were taken, placed in the vehicle basket, and transported to the surface. For microscopic investigations, polished thin sections from the rock samples were prepared and examined in terms of mineral identification and texture of igneous rocks. For this purpose, a LEICA DMRX stereomicroscope was used. Additionally, X-ray fluorescence (XRF) analysis was used to determine the elemental composition of the rocks. The XRF analysis was conducted at the Institute for Chemistry and Biology of the Marine Environment (ICBM) in Oldenburg.

**Table 3.1**

ROV dives deployed at Vent field for visual seafloor mapping and rock sampling.

Ship station	ROV dive	Latitude	Longitude	Water depth	Sample ID	Description
PS119/028	ROV 447	59°41.679'	28°21.093'	1418.6 m	028-5R	Rock with fine-crystalline sulfur (Great Wall)
PS119/028	ROV 447	59°41.678'	28°21.095'	1416.7 m	028-6R	Rock from Great Wall
PS119/033	ROV 448	59°41.668'	28°21.054'	1427.2 m	033-3B	Rock from clam field

### 3.4 Results

#### 3.4.1 Morphology and backscatter

The main purpose of the multibeam swath bathymetry surveys was bathymetric mapping to gain new insights into the geomorphology of the Kemp Caldera (Figure 3.2).

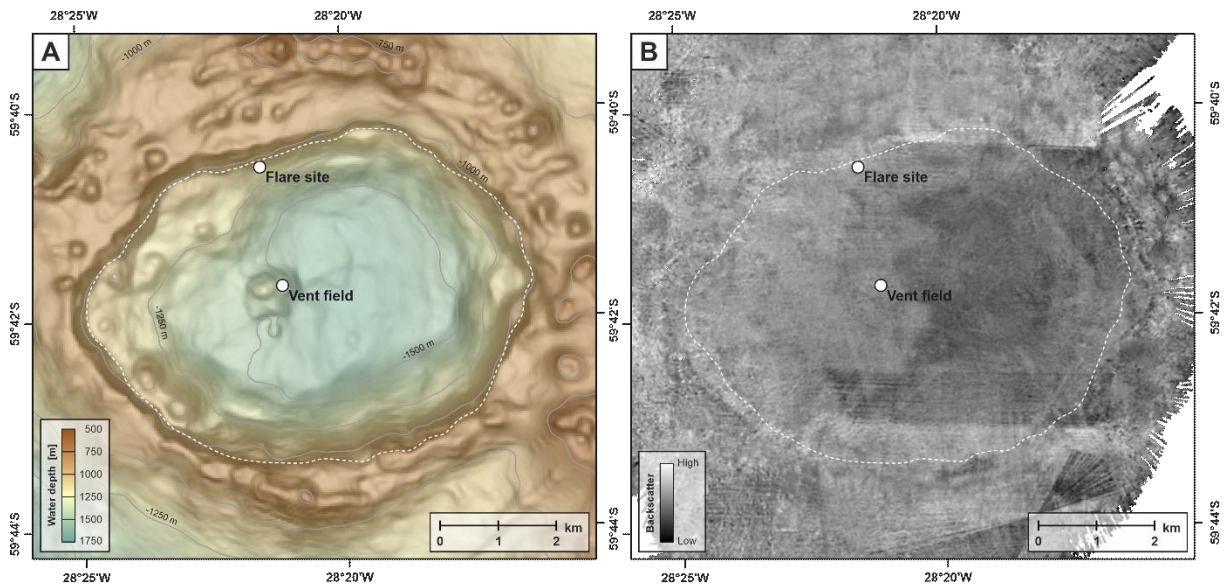


**Figure 3.2.** A) Bathymetric map of the Kemp Caldera with Vent field and Flare site. The white dashed line indicates the upper edge of a stepped terrace in a water depth of ca. 1070 to 1170 m, and B) Map of processed backscatter results.

In the bathymetric map it is seen that the Kemp Caldera has a subcircular shape (Figure 3.2A). It has a rim-to-rim extension from north to south of about 6.5 km and an east-west width of roughly 8.6 km. At its deepest point in the eastern center, the caldera floor is ~1618 m deep, while the caldera rim lies in a water depth of mainly between 800 and 900 m. Several secondary cones are found especially at the northern and eastern caldera rim, which reach a depth of ca. 630 m below the water surface. In the western center of the Kemp Caldera there is also a secondary cone, interpreted as resurgent cone (Linse et al., 2019; Kürzinger et al., 2022). The top of this cone lies in a water depth of 1339 m and thus towers over the caldera floor by more than 270 m. Inside the caldera at a depth of about 1070 m in the west and ca. 1170 m in the east close to the rim, a morphologic step can be seen as stepped terrace at the inner caldera wall (Figure 3.2A).

Backscatter data were used to get an overview of the Kemp Caldera surface facies and the roughness of the seafloor. The distinction between high and low reflectance is represented as a brightness gradation: white (high reflectance, usually indicating harder surfaces) to black (low reflectance, usually indicating softer surfaces). As seen in Figure 3.2B, the Kemp Caldera floor shows a rather inhomogeneous backscatter pattern. However, two different backscatter facies separate the caldera floor in an eastern and a western part of similar extent along a roughly N to S directed lineation. A slightly lower backscatter appears to characterize the eastern part of the caldera floor, while the western part shows a relatively high backscatter, similar to the caldera rim.

### **3.4.2 OFOBS seafloor observations and sub-bottom information**

As mentioned above, there are two backscatter facies dividing the Kemp Caldera in an eastern and western part. Based on OFOBS seafloor observations, the reasons for differences between the backscatter facies could be described in more detail. The area of low reflectance is characterized by sediment as soft ground (Figure 3.3D), while the western area is dominated by hard ground consisting of volcanic rock (Figure 3.3C), which reflects the signals of the ship-based multibeam echosounder in higher intensity.

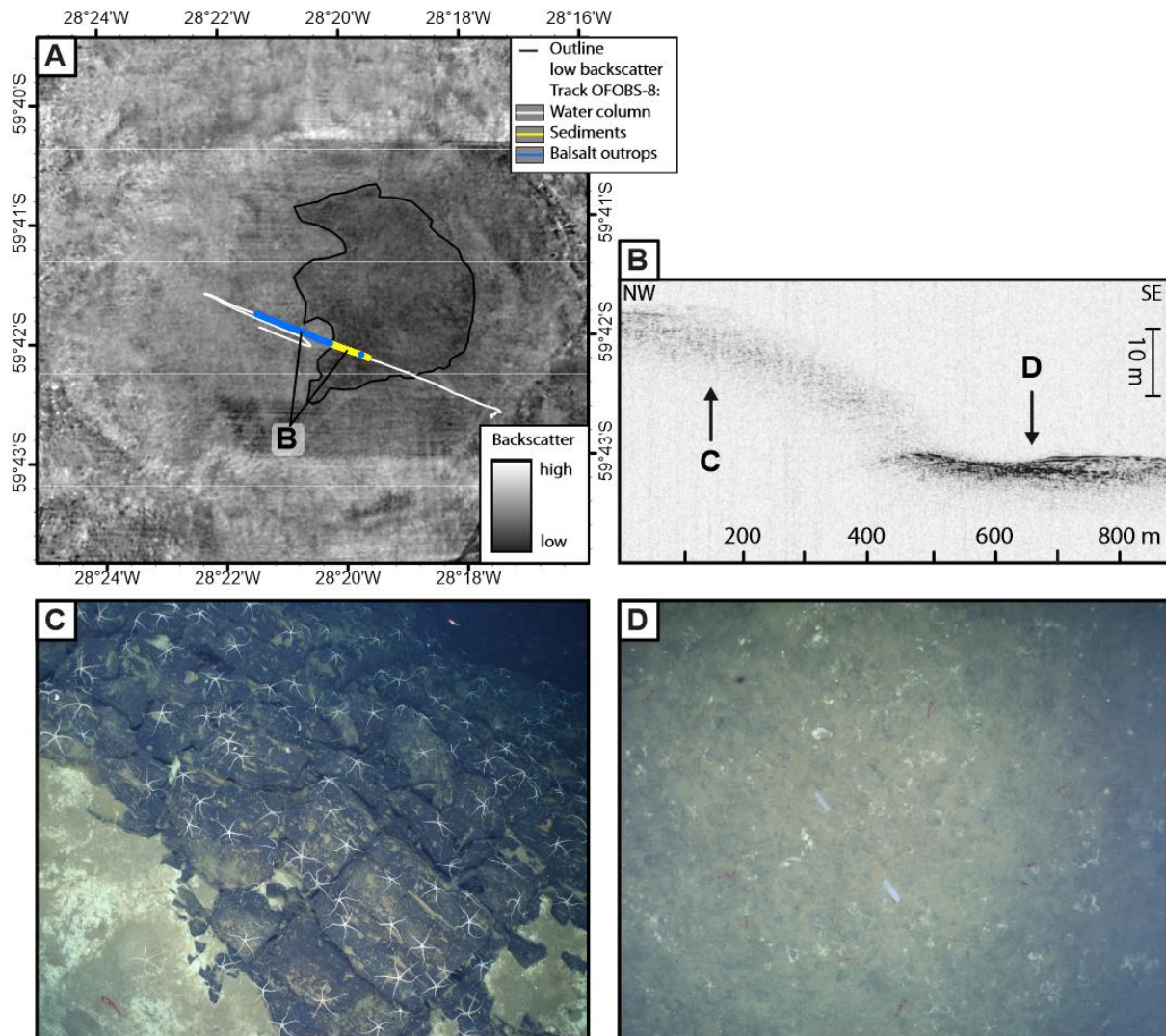


**Figure 3.3.** A) Backscatter data (eastern part with lower reflectance is framed) with the OFOBS-8 track (white line). The blue and yellow highlighted line denotes the sub-bottom profile in (B), B) Sub-bottom profile displaying the transition from the area of high reflectance (C) to the area of low reflectance (D), C) Seafloor image showing a steep slope of blocky volcanic rock colonized by a vast number of brittle stars, and D) Sediment-covered area in the eastern half of the caldera.

With respect to the *PARASOUND* data, sub-bottom profiles could barely be displayed and show a different picture than expected from the backscatter data and OFOBS images. This is due to a very steep caldera rim and little penetration at the western caldera part, resulting in scattering of the signal and a cloudy, almost transparent seafloor reflection. Only in the eastern part of the caldera, penetration of a few meters into the sub-bottom was achieved and partly layers, which partly could be identified as sediment, were visible (Figure 3.3B).

### 3.4.3 Visual seafloor mapping

Using ROV video surveys, visual seafloor mapping was conducted in two hydrothermally active areas of the Kemp Caldera: a) the Vent field at the foot of the eastern flank of the resurgent cone in the caldera's center, and b) the Flare site at the NNW of the caldera (Figure 3.2A). Results of the visual mapping are summarized in Figure 3.4 and 3.6.

#### *Vent field*

The Vent field is the most hydrothermally active area within the Kemp Caldera known so far, located in the caldera's center to the east of the resurgent cone. This area hosts three vent sites: Great Wall, Toxic Castle and Winter Palace. The Vent field floor is mainly covered by sediment except for the slope side in the northwest, which is dominated by boulders and bedrock outcrops (Figure 3.4 and Figure 3.5-7). Downslope to the east, the bedrock is increasingly covered by sediments, but still boulders and smaller rocks are visible on top of the sediment. The white smoker vent sites Toxic Castle and Winter Palace, where small white smoker chimneys and mounds are present, are sediment-dominated.

Great Wall, one of the hydrothermally active sites in this area, is located in a water depth of ca. 1416 m at the eastern flank of the resurgent cone. The wall-like structure from which this site owes its name, mainly consists of weathered rock (Figure 3.5-1). In some places, the wall is covered by microbial mats, limpets and by fine-crystalline elemental sulfur. In addition to Great Wall, such sulfur walls also exist in the surrounding area, where sulfur-bearing hydrothermal fluids escape through fissures and cracks in the seafloor (Figure 3.4). The area around Great Wall is mainly sandy ground with some larger and smaller boulders on top (Figure 3.5-1 and 3.5-6). Downslope toward both Toxic Castle and Winter Palace vent fields, these boulders diminish and decrease in size.

Toxic Castle is located < 80 m east-southeast to Great Wall and its morphological features are different compared to its western neighbor site. This actively venting area hosts several white smoker chimneys and mounds (Figure 3.5-2a). An interesting phenomenon of this site is the occurrence of liquid elemental sulfur (Figure 3.5-2b). At some spots, the liquid sulfur drips out of the rock and rapidly cools to sulfur spherules. At other places, the sulfur is already solidified to sulfur drops, covering some of the mounds. We also discovered a flange structure at Toxic Castle, from which hot water was rising from below and turned into white smoke (Figure 3.5-3).

Winter Palace, like Toxic Castle, is an active white smoker vent field and is located at a water depth of ~1422 m. Unfortunately, due to low visibility caused by the white smokers, less features could be distinguished than at the other locations. However, also here liquid elemental sulfur was discovered in patches (Figure 3.5-4).

The Kemp Caldera, the southernmost arc caldera volcano from the South Sandwich island arc – New results from seafloor investigations

To the north, about halfway from Great Wall to Toxic Castle, a clam field is present in a small depression (Figure 3.5-5). This sediment patch, hosting living clams, lies between hillocks, covered by sediment and small boulders.

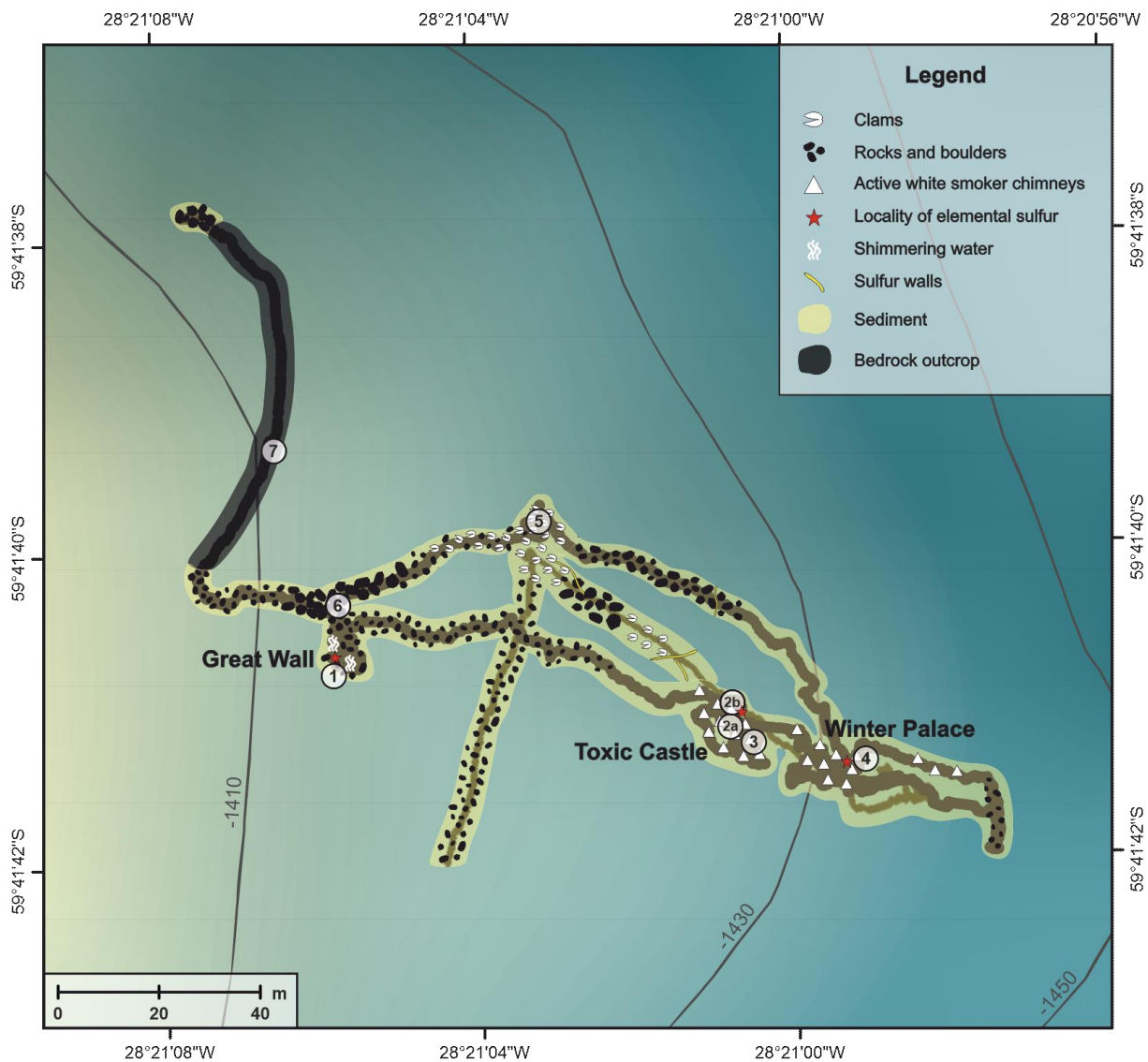


**Figure 3.4.** Map created from visual ROV seafloor observations (ROV 447 and 448) of the Vent field area. The numbers in this map refer to corresponding numbers of seafloor images in Figure 3.5.

The Kemp Caldera, the southernmost arc caldera volcano from the South Sandwich island arc – New results from seafloor investigations

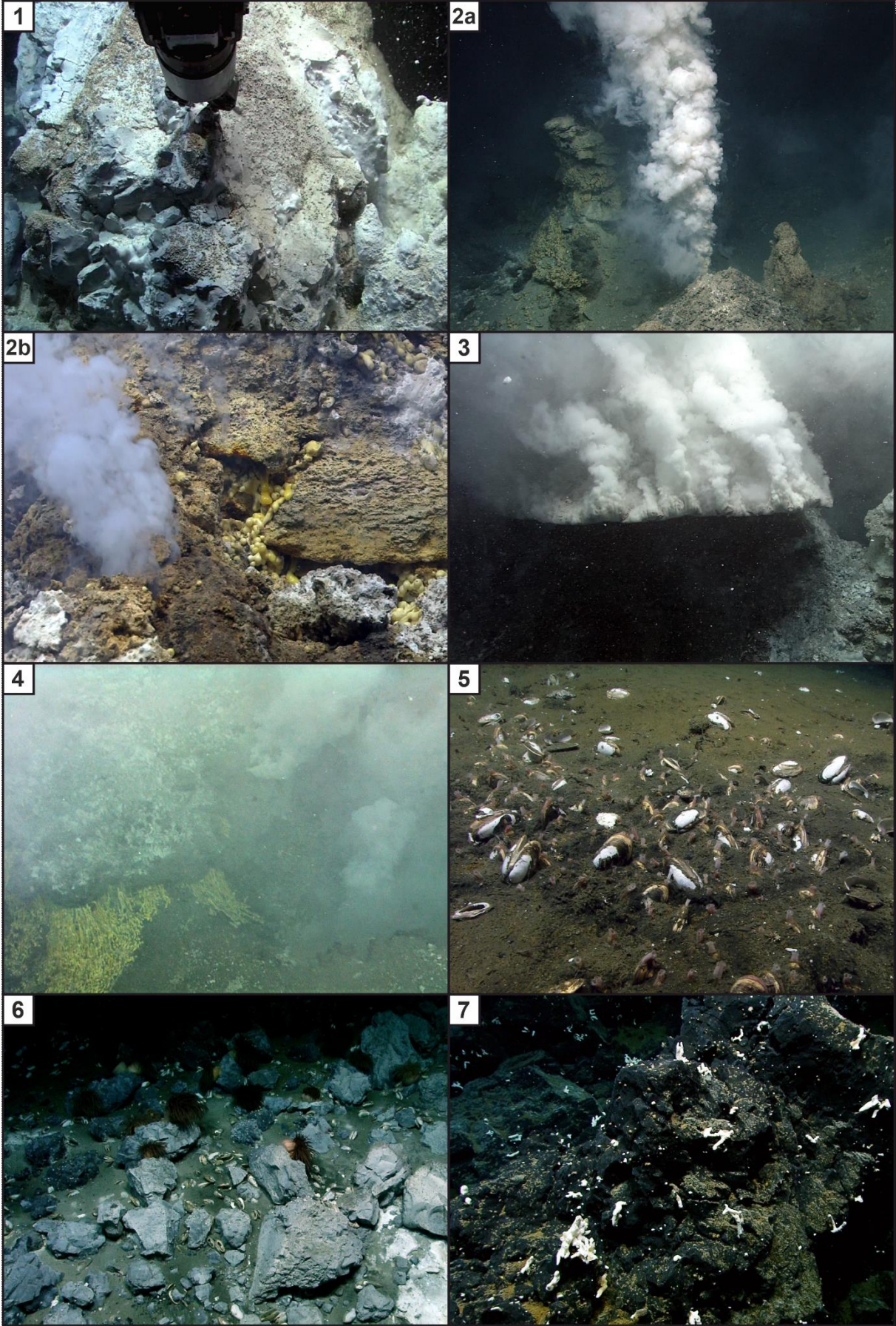


**Figure 3.5.** Seafloor images showing 1) Rock sampling from wall-like structure at Great Wall. The wall consists of weathered rock, which is partly covered by fine-crystalline sulfur, microbial mats and limpets, 2a) Actively venting white smoker at Toxic Castle, 2b) Liquid sulfur at Toxic Castle dripping out of the rock and rapidly cools to sulfur spherules, 3) Flange structure (Toxic Castle), from which hot water rises from below and turned into white smoke, 4) Liquid elemental sulfur at Winter Palace, similar to that found at Toxic Castle. However, the visibility was much worse here because of the turbidity caused by the actively venting white smokers. 5) Clam field with living clams on a sediment field northwest of Toxic Castle, 6) Sediment covered with boulders of different size, which are slightly to strongly weathered, and 7) Bedrock partly overgrown with sponges.

### *Flare site*

The Flare site is located at the NNW rim of the Kemp Caldera in a water depth between 1110 and 1190 m. Due to the detection of a gas flare at this site with the echosounder of the vessel, a ROV dive was deployed to further investigate the area. As seen in the map (Figure 3.6), there was not always visual ground contact because the first half of the dive was used to find the gas bubbles in the water column with use of the ROV mounted forward looking sonar. Hence, visual seafloor mapping of the Flare site was restricted to the second part of the dive.

The ROV dive 449 started in the northeastern part of the Flare site, trying to localize the source of the gas bubbles, which were unfortunately not detected. During short moments of ground visibility, bedrock outcrops (Figure 3.7-1) and old, inactive chimney structures (Figure 3.7-2) were visible. After finishing the search for the gas bubble source, the area was further investigated regarding possible hydrothermally active sites. In a water depth of ~1135 m, a new site was discovered, named Beehive Chimney. This actively venting beehive-shaped chimney is surrounded by bigger and smaller boulders, and inactive chimneys were found in immediate vicinity as well (Figure 3.7-4). The area south of Beehive Chimney is predominantly sediment covered with boulders lying on top (Figure 3.7-3). Further south, the boulders decrease in size or are no longer present, leaving some areas covered only by sediment (Figure 3.7-5). In the southwest of the Flare site area, a second vent field was found, named Devil's Horn (Figure 3.6). This area hosts a large field of high chimney structures, but none of them were actively venting. At the base of a particularly impressive chimney structure, shimmering water was observed (fluid temperature of 198.3 °C).

The Kemp Caldera, the southernmost arc caldera volcano from the South Sandwich island arc – New results from seafloor investigations

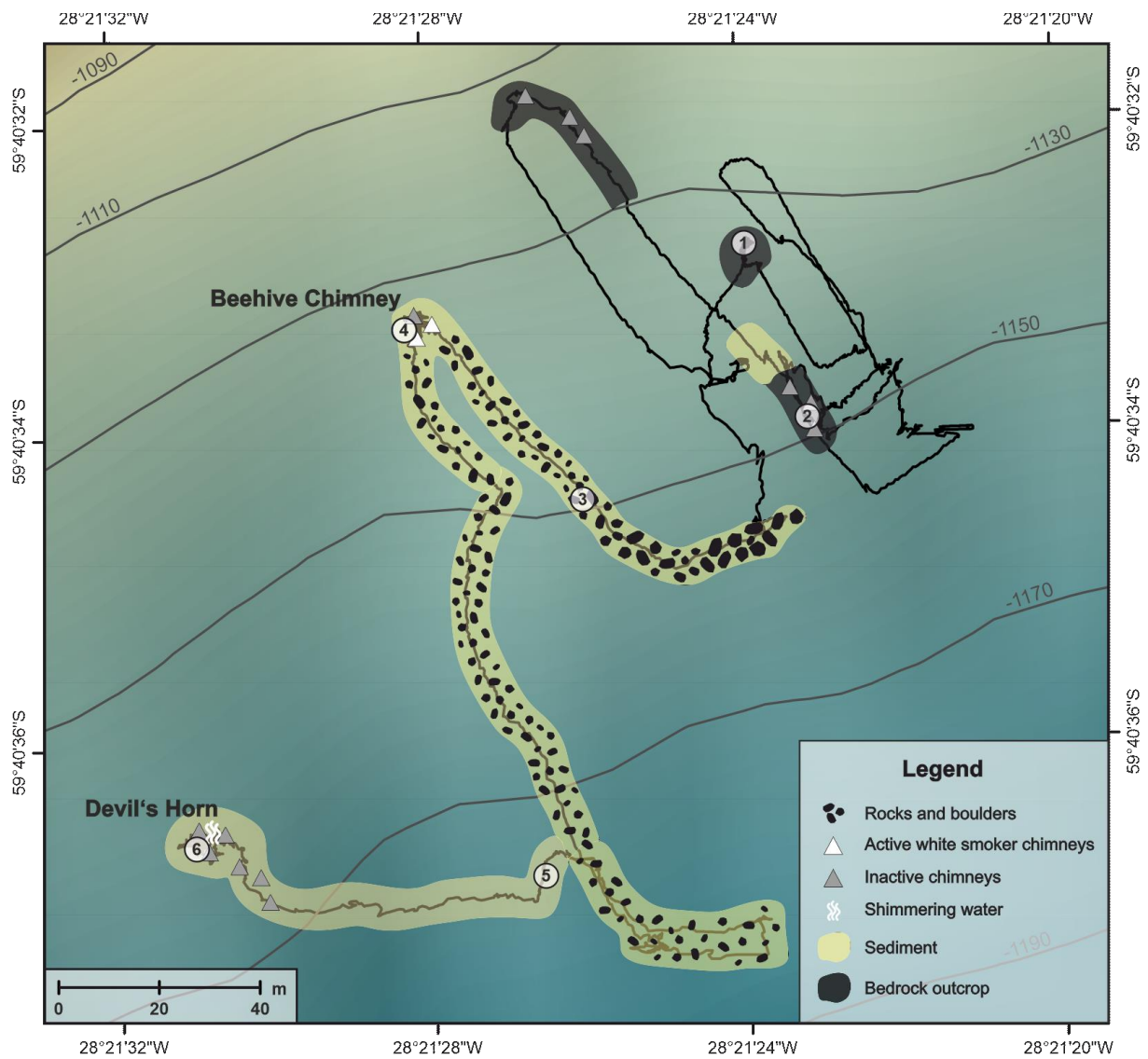


**Figure 3.6.** Map created from visual ROV seafloor observations (ROV 449) of the Flare site. During the first half of the dive, bottom visibility was not always assured as the water column was searched for the source of the flare. The numbers in this map refer to corresponding numbers of seafloor images in Figure 3.7.

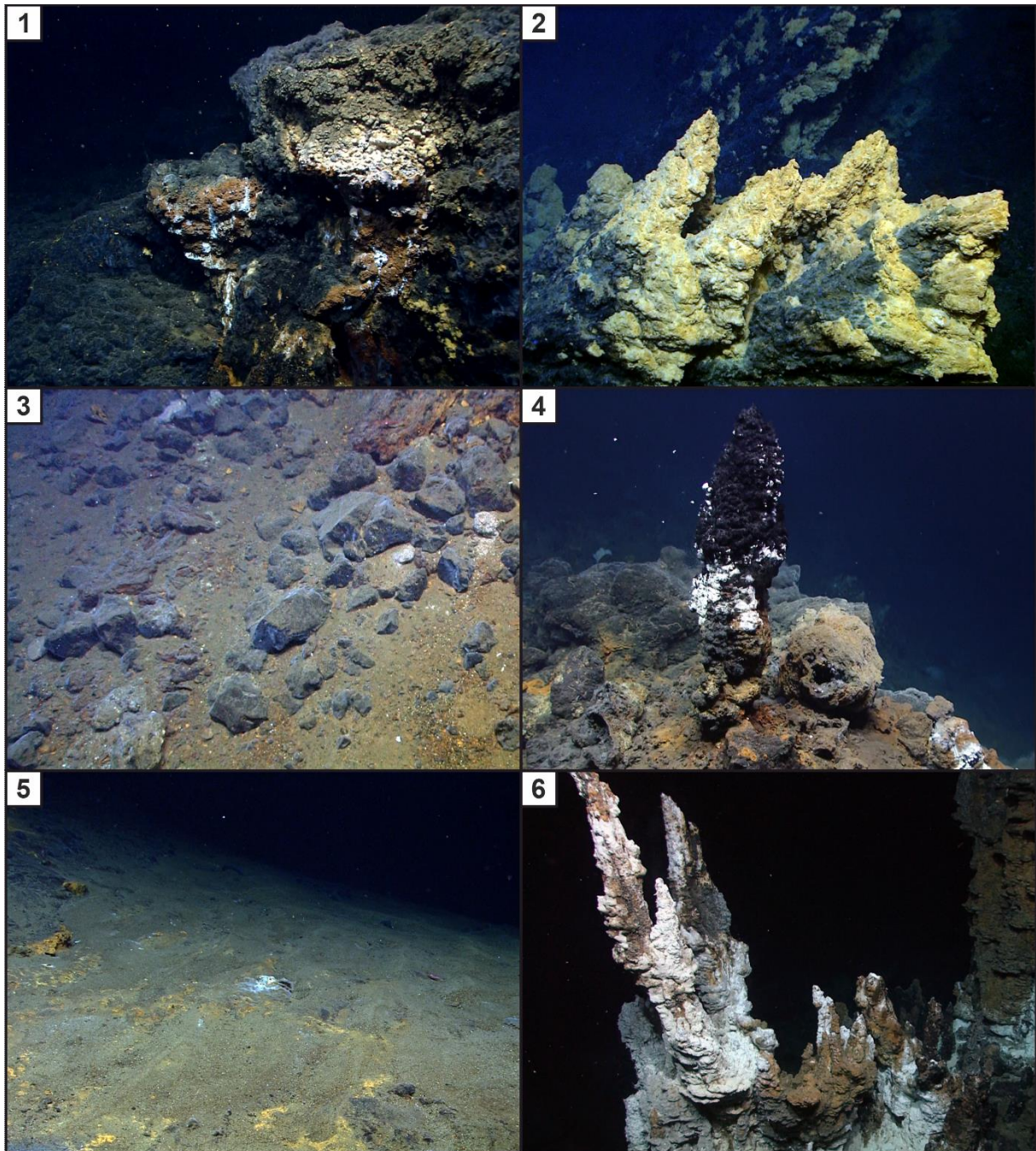


**Figure 3.7.** Underwater images from several areas within the Flare site. 1) Bedrock outcrop partly weathered with brownish stains, 2) Chimney-like structures partially weathered (yellowish material), 3) Sediment with boulders on top. The sediment shows a brownish discoloration in some places as well as some of the rock pieces (upper right corner of the image), 4) Actively venting beehive-shaped chimney at the newly discovered site Beehive Chimney. Beside this big chimney, some smaller also active chimneys were found next to old, inactive ones, 5) Wide sediment-covered area with only a few spots with discoloration and microbial mats, and 6) Oblique plan view of the biggest chimney structure at the location Devil's Horn.

### 3.4.4 Rock samples

Three rock samples were taken from the Vent site in the center of the Kemp Caldera. Polished thin sections were made of these samples and studied with transmitted light microscopy for mineral identification. Detailed microphotographs of the thin sections are shown in Figure 3.9. Further on, XRF analysis was used to determine the elemental composition of the rock samples. The XRF results are listed in Table 3.2.

Two of the three rock samples were taken from Great Wall. One rock piece (028-5R) was taken from the foot of the wall structure, the other one (028-6R) was sampled directly from the wall itself. Both samples have a dark gray to black color and occasionally brownish stains. The fine-crystalline sulfur adheres to the rough surface of the rocks (Figure 3.8). In the handpiece, the surfaces are slightly shiny and vesicles in the size of < 1 mm are visible.

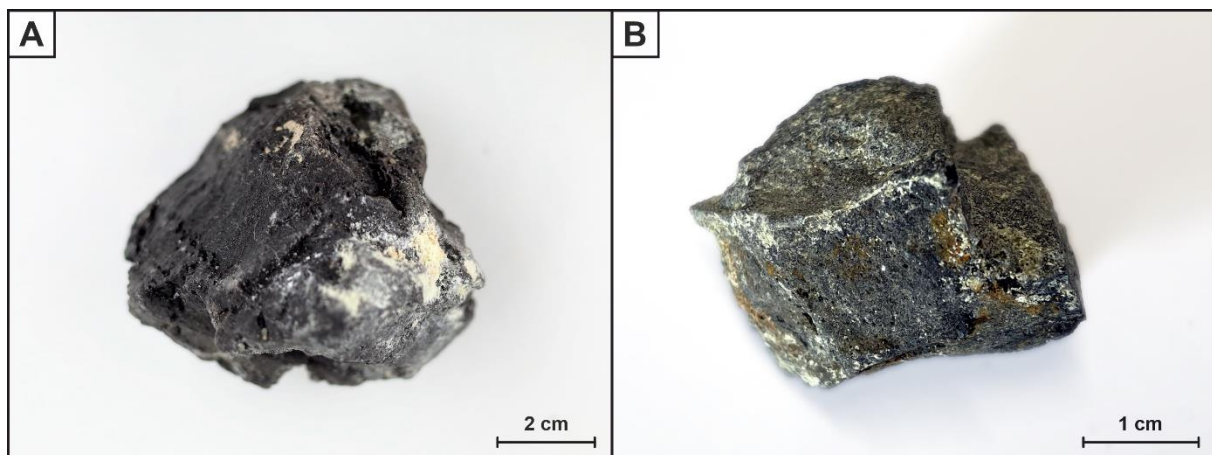


**Figure 3.8.** Rock samples from Great Wall. A) Sample 028-5R recovered from the foot of the wall structure, and B) Smaller piece of the sample 028-6R which was taken directly from the wall.

Both samples have a porphyritic texture. Their matrix is glassy and contains acicular plagioclase micro-phenocrysts (< 150  $\mu\text{m}$ ) that are locally aligned (Figure 3.9). Plagioclase and clinopyroxene in the size of > 200  $\mu\text{m}$  occur as single phenocrysts or in mineral accumulations (small xenoliths).

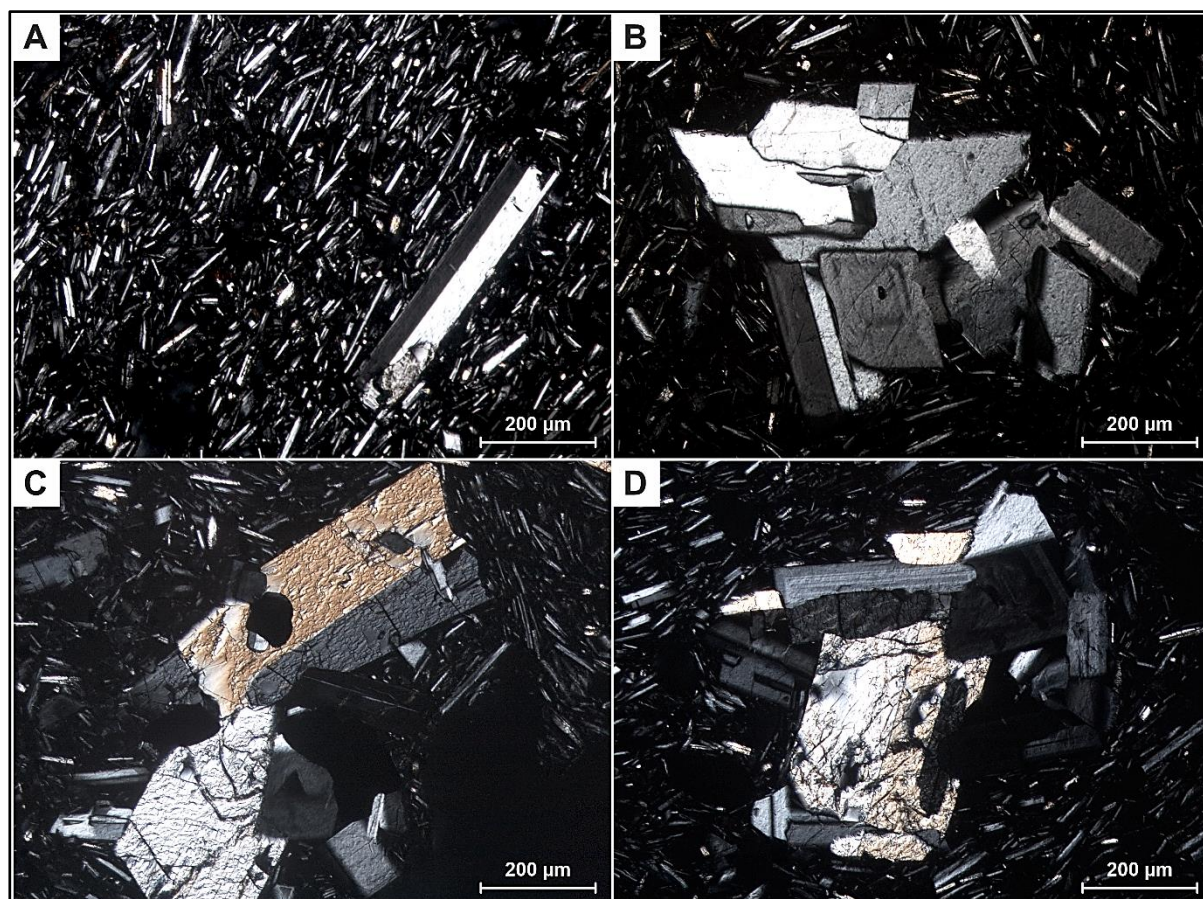


**Figure 3.9.** Detailed microscopic images (crossed polarized transmitted light) of thin sections made from Great Wall rock samples 028-5R and 028-6R. A) Glassy matrix and acicular plagioclase crystals with a plagioclase phenocryst. A slight intimation of a flow structure can be seen, as most of the plagioclase crystals are oriented in one direction, B) Accumulation of tabular to prismatic plagioclase crystals, C) Twinned clinopyroxene phenocrysts within plagioclase-rich matrix, and D) Mineral accumulation consisting of a ca. 500 µm sized twinned clinopyroxene crystal (resorption texture at right crystal edge) and several smaller plagioclases.

XRF data of the rocks sampled at the Vent field of the Kemp Caldera are listed in Table 3.2. An SiO<sub>2</sub> content of more than 67 wt% and alkali contents of ca. 5.2 wt% indicate a dacitic composition of the rocks, according to the total-alkali silica classification (TAS; LeBas et al., 1986). Considering the high content of Fe<sub>2</sub>O<sub>3</sub> and relatively low MgO content (Table 3.2), the Kemp Caldera samples from the resurgent cone fall in the tholeiitic field of the AFM diagram (cf. Vermeesch and Pease, 2021).

**Table 3.2**

XRF whole-rock data in weight%.

Sample ID	SiO <sub>2</sub>	TiO <sub>2</sub>	Al <sub>2</sub> O <sub>3</sub>	Fe <sub>2</sub> O <sub>3</sub>	MnO	MgO	CaO	Na <sub>2</sub> O	K <sub>2</sub> O	P <sub>2</sub> O <sub>3</sub>
028-5R	67.68	0.64	13.50	6.53	0.16	1.06	4.35	4.16	1.01	0.22
028-6R	67.40	0.64	13.39	6.38	0.15	1.09	4.35	4.19	1.02	0.23
033-3B	67.72	0.65	13.46	6.67	0.15	1.06	4.35	4.24	1.00	0.23

### 3.5 Discussion

#### 3.5.1 Geomorphology of the Kemp Caldera and distribution of hydrothermal vents

The morphology of the Kemp Caldera resembles that of a resurgent caldera (Cole et al., 2005). In the central part of a caldera, resurgence often occurs due to refilling of the subvolcanic magma reservoir, which causes uplift of the caldera floor (Smith and Bailey, 1968; Lipman, 1997; Acocella, 2021). However, the process of resurgence of a resurgent caldera usually results in an uplift and doming of the entire caldera floor, which is not the case for the Kemp Caldera. The asymmetry of the caldera floor in the Kemp Caldera could be caused by uplift, which affects only the western part of the caldera (Figure 3.10). The morphology of the central cone suggests that it is an extrusive (resurgent) cone as result of a post-caldera eruption, while the uplift of the western caldera floor may be caused by a spatially restricted shallow intrusion.

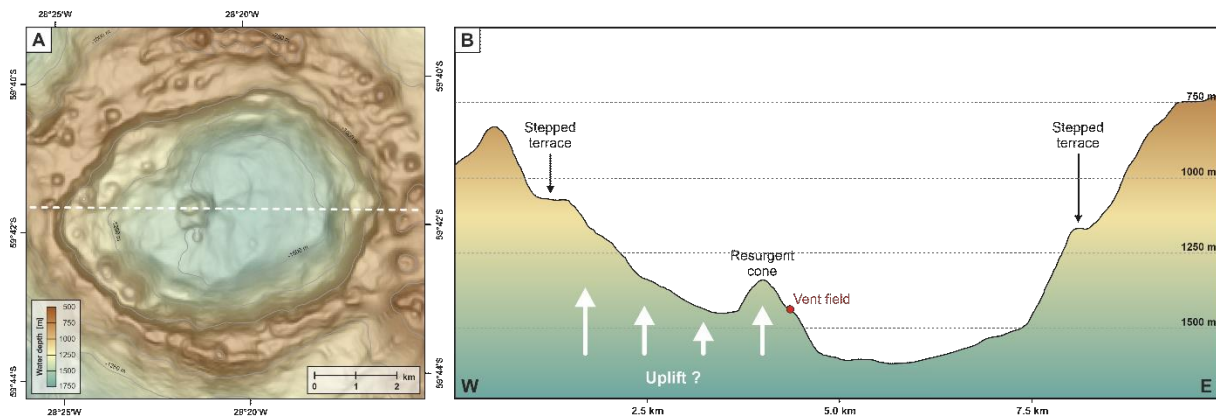


**Figure 3.10.** A) Bathymetric map of the Kemp Caldera showing the position of the profile (dashed white line) trending from W to E, and B) W-E bathymetric profile through the Kemp Caldera.

The fact that the caldera floor in the western part is generally shallower than the eastern caldera floor could depend on interaction of different factors in addition to uplifting processes due to a shallow magma intrusion. The post-caldera eruption, which leads to the formation of the resurgent cone in the center of the caldera, may be accompanied by uplift caused by refilling of the underlying magma chamber resulting in a shallow magma intrusion as abovementioned. This small intrusion led to inhomogeneous uplift of the caldera floor that affected only the western part of the caldera and left the eastern caldera floor nearly untouched. The instability of the caldera walls additionally modifies the morphology of the caldera floor and the caldera itself. Steep walls are formed during the first caldera forming event(s) and rapid subsidence of the inner caldera floor. These steep and prominent caldera walls are unstable, which could have resulted in gravitational mass wasting. Hence, the uplift-induced movement of the post-caldera eruption could trigger debris flow from the caldera wall

(and the resurgent cone), leading to mass wasting deposits inside the caldera within the uplifted area.

A stepped terrace is seen as a distinct edge at a water depth of ~1070 m to the west and ~1170 m to the east (Figure 3.10B). This terrace may represent a subsided block of the inner caldera wall or a former caldera floor from a previous collapse. Some calderas are formed not only from one single caldera-forming event, but undergo several effusive or explosive eruptions that cause repeated subsidence events (Branney and Acocella, 2015). Based on the observed morphology, it is suggested that the Kemp Caldera was formed due to at least one caldera collapse phase associated with magma withdrawal. A shallow magma chamber below the current caldera must have therefore existed. The collapse of a volcanic edifice due to withdrawal of magmatic supply has formed the caldera, resulting in ring faults and other fractures caused by subsidence (Branney, 1995; Acocella et al., 2012). However, such ring faults could not be identified by the ship's hull-mounted multibeam echosounder.

In most cases, these ring faults and fractures occur close to the caldera margin, as this is the area of main faulting and intense deformation (Branney and Acocella, 2015). These faults connect the subvolcanic magma reservoir with the seafloor and can act as pathways for infiltrating seawater and related hydrothermal fluids (e.g., de Ronde et al., 2011; Berkenbosch et al., 2015; Acocella, 2021; Klose et al., 2022). Consequently, hydrothermal activity and intense hydrothermal alteration in (submarine) calderas predominantly occur at the rim (Eddy et al., 1998; Berkenbosch et al., 2015; Branney and Acocella, 2015). At Kemp Caldera, such a hydrothermally active site probably related to faults close to the caldera rim has been identified, the Beehive Chimney at the Flare site at the NNW caldera rim. However, hydrothermal activity in the Kemp Caldera is not only found at its rim, but also within the Vent field around the resurgent cone. In calderas where resurgence occur, the uplifted area is typically intersected by minor faults and fissures (Branney and Acocella, 2015; Acocella, 2021). In case of the Kemp Caldera, this concerns the central area around the resurgent cone. Extrusive volcanism and the supply of fresh lava may have formed small faults around the cone, where hydrothermal flow and heat flow has been focused.

A temporal change in hydrothermal activity is especially seen in the Vent field hydrothermal fluids and their change in temperature. Fluids of Great Wall sampled and measured during the R/V *James Cook* cruise JC42 reached temperatures of 21.1 °C (Rogers, 2010; Cole et al., 2014), while the fluids of the same site measured in 2019 during the R/V *Polarstern* cruise PS119 have temperatures of 63 °C (Kürzinger et al., 2022). Simultaneously, a temperature increase is observed in the Toxic Castle fluids. This area was previously known as diffuse fluid flow area (Tyler, 2011; Hepburn, 2015), which generally indicate relatively low temperatures,

however, in 2019 fluid temperatures measured ranged from 207 to 237 °C (Kürzinger et al., 2022).

Hydrothermal activity present in the western part of the caldera in contrast to its eastern part is also seen in the results shown by mapping the oxidation-reduction potential (ORP) anomalies (Thomas Pape, personal communication). ORP anomalies are exclusively detected in the western part (Figure 3.11). Such anomalies were measured with ORP sensors that respond to the presence of reduced hydrothermal chemicals, e.g.,  $\text{HS}^-$ ,  $\text{H}_2$  and  $\text{Fe}^{2+}$  (Walker et al., 2007). Hence, ORP anomalies are related to hydrothermal activity, which in case of the Kemp Caldera mainly occur around the resurgent cone and close to the caldera rim (Thomas Pape, personal communication).

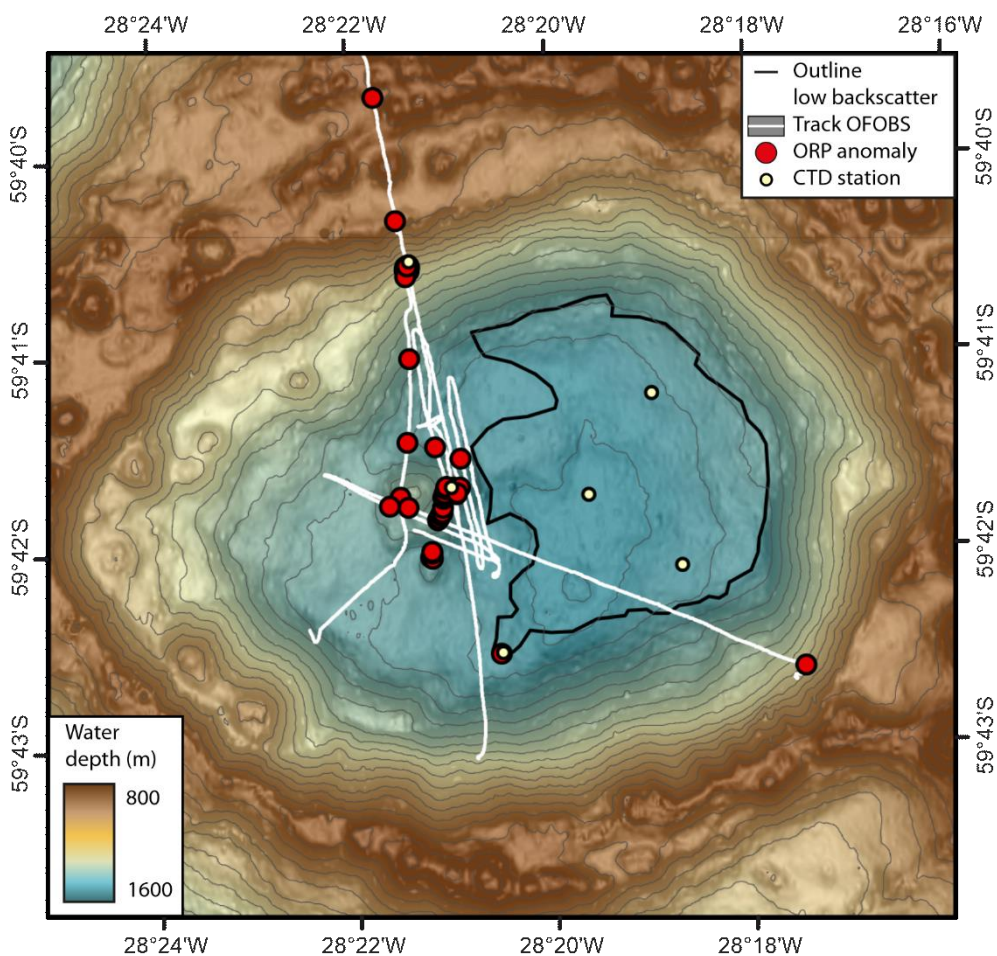


**Figure 3.11.** Distribution of ORP anomalies with  $dE/dt$  values  $< -0.02$  mV/S are plotted in the map (ORP anomaly data taken from Thomas Pape, personal communication).

### 3.5.2 Formation and evolution of the Kemp Caldera

Previously, it was assumed that the rock type of the Kemp Caldera is the same as that of the neighboring Kemp Seamount, which consists primarily of tholeiitic basalt and basaltic andesite

with SiO<sub>2</sub> contents between 50 and 53 wt% (Leat et al., 2004; Leat et al., 2013; Cole et al., 2014). The dacite samples from the Kemp Caldera Vent field, however, have a considerably higher SiO<sub>2</sub> content. With SiO<sub>2</sub> > 67 wt%, the sampled rocks clearly exceed the SiO<sub>2</sub> content of basalt or basaltic andesite and point to more silicic/felsic volcanic rocks. This matches our seafloor observations of relatively fresh blocky lavas around the cone structure (see Figure 3.3C), a feature typical for dacitic volcanism.

Even if the composition of the rocks from the caldera center are different from that of Kemp Seamount, there are unfortunately no rock samples from the outer rim of the caldera. The only information about Kemp Caldera rocks from the NW caldera wall is provided in the JR224 cruise report (Larter, 2009), which states on the basis of visual observation that the caldera walls consist of hexagonal basalt pillars. However, neither samples nor rock data exist. Considering that glassy dacite samples can also be dark in appearance, it cannot be completely ruled out that the rocks outside the center are dacitic and hence different from those of Kemp Seamount.

It can be assumed that both Kemp Seamount and the former “Kemp Volcano” were formed by the basaltic to rhyolitic volcanism resulting from the ongoing subduction of the South American Plate under the Sandwich micro-plate (Larter et al., 1998; Leat et al., 2004; Barry et al., 2006). The erupted material forming these two seafloor features had a rock composition of tholeiitic basalt to basaltic andesite (Leat et al., 2004; Leat et al., 2013; Cole et al., 2014). Later, magma withdrawal of the subvolcanic magma chamber caused the collapse of the “Kemp Volcano” and leads to the formation of the Kemp Caldera. Resurgence and uplift are commonly initiated relatively soon after the caldera collapse event(s), in the range of 10 a to 100 ka (Nielson and Hulen, 1984; Branney and Acocella, 2015). This uplift takes place when new magma refills the shallow reservoir. The now erupted material had a more felsic (dacitic) composition, which indicates that the magma resided in the partial drained subvolcanic magma reservoir remained there long enough to become more siliceous than the initially erupted magma (cf. Cole et al., 2005). Thus, this might lead to the two different rock types that are found within the Kemp Caldera.

Another possibility is that the entire Kemp Caldera is of dacitic composition. The composition of magmas that are associated with subduction-related volcanism vary with increasing distance to the subduction front (Duggen et al., 2007). Rear-arc magmas are generally more siliceous than the magmas of the volcanic arc itself (Duggen et al., 2007). Two examples of submarine caldera volcanos of broadly similar rock composition are Brothers volcano (Kermadec arc) and Niuatahi volcano (NE Lau Basin), which are similar in shape and size to Kemp Caldera. Brothers and Niuatahi are predominantly dacitic in composition and have also dacite post-caldera cones within the caldera (de Ronde et al., 2011; Berkenbosch et al., 2015;

de Ronde et al., 2019). Due to the rear-arc position of the Kemp Caldera, it appears possible that the Kemp Caldera was also formed by dacitic volcanism. Further rock sampling at Kemp Caldera and especially at its rim is needed to resolve its composition and finally its evolution.

### **3.6 Conclusion**

The results of this study provide detailed visual seafloor observations and descriptions of the bathymetric characteristics of the Kemp Caldera and the hydrothermal vent areas detected at the caldera rim and floor. The asymmetry of the caldera floor may result from uplift caused by a local intrusion. Additional mass wasting events may have occurred due to the instability of the caldera walls, enhancing the asymmetry of the floor.

The focus of hydrothermal activity is the dacitic resurgent cone in the central area of the Kemp Caldera and the NNW caldera rim, which is also confirmed by anomalies of mapped oxygen reduction potential. This cone may be the result of a post-caldera eruption of differentiated magma, resulting in the extrusion of blocky, dacitic lavas. Due to the post-caldera eruption, heat flow is focused at the resurgent cone, resulting in a temperature increase of hydrothermal fluids of the Vent field over time.

The former suggestion that Kemp Caldera may be composed of the same rock type as Kemp Seamount was based only on the fact that hexagonal columns, interpreted as basalt columns, have been seen on the NW caldera rim during the JR224 R/V *James Clark Ross* cruise in 2009 (Larter, 2009). However, to verify the rock composition of the entire caldera, it would be necessary to take further rock samples.

### **Acknowledgements**

Many thanks go to Captain M. Langhinrichs and the crew from the R/V *Polarstern* PS119 cruise. Their support and cooperation with the ROV *MARUM QUEST 4000* team was excellent. Special thanks go to P. Wintersteller, who was responsible for the acquisition of bathymetric data and supported the OFOBS dives during the PS119 expedition. Thanks also go to A. Klügel (University of Bremen, Germany), who supported the work with his knowledge about volcanoes and calderas. The PS119 expedition was funded by the German Federal Ministry of Education and Research Foundation (Deutsche Forschungsgemeinschaft, DFG) within the Cluster of Excellence (EXC-2077, project number 390741603 “The Ocean Floor – Earth’s Uncharted Interface”) at MARUM – Center for Marine and Environmental Sciences, University of Bremen.

## 4 MANUSCRIPT II

### SULFUR FORMATION ASSOCIATED WITH COEXISTING SULFIDE MINERALS IN THE KEMP CALDERA HYDROTHERMAL SYSTEM, SCOTIA SEA

Victoria Kürzinger<sup>1,2</sup>, Alexander Diehl<sup>1,2</sup>, Samuel I. Pereira<sup>3,4</sup>, Harald Strauss<sup>5</sup>, Gerhard Bohrmann<sup>1,2</sup>, Wolfgang Bach<sup>1,2</sup>

<sup>1</sup> MARUM Center for Marine Environmental Sciences, University of Bremen, Leobener Straße 8, 28359 Bremen, Germany

<sup>2</sup> Faculty of Geoscience, University of Bremen, Klagenfurter Straße 2-4, 28359 Bremen, Germany

<sup>3</sup> Department for Earth Sciences, University of Bergen, Realfagbygget, Allégaten 41, Bergen 5007, Norway

<sup>4</sup> Centre for Deep Sea Research, University of Bergen, Realfagbygget, Allégaten 41, Bergen 5007, Norway

<sup>5</sup> Institut für Geologie und Paläontologie, WWU Münster, Corrensstraße 24, 48149 Münster, Germany

#### Published in Chemical Geology

---

#### Abstract

The Kemp Caldera is a submarine caldera located in the southernmost part of the intra-oceanic South Sandwich arc, Scotia Sea. The caldera comprises a unique hydrothermal system in which elemental sulfur ( $S^0$ ) coexists with sulfide minerals at unusually high pH-values ( $pH_{25\text{ }^\circ\text{C}} > 5$ ). During the 2019 R/V *Polarstern* PS119 expedition, samples from the white smoker vent fields in the center of the caldera were recovered by a remotely operated vehicle. The sampling of elemental sulfur took place at the vent sites Great Wall and Toxic Castle, which are located < 80 m apart. At Great Wall, sulfur is fine-crystalline, while at Toxic Castle  $S^0$  occurs in liquid form, forming amorphous and globular structures. Here, tabular plates of covellite are found as inclusions in the quenched sulfur. The fluids from both sites have pH-values of about 5.4 to 5.7 (at 25 °C) and show a relatively wide temperature range from 63 to > 200 °C. The isotope values of sulfide and elemental sulfur range from 4.6 to 5.8 ‰, while sulfate concentrations at Great Wall are lower than in seawater.

Elemental sulfur in submarine arc/back-arc systems is commonly believed to form by disproportionation of  $SO_2$ . It generally shows negative  $\delta^{34}S$  values and precipitates from acid-sulfate type hydrothermal fluids with pH-values as low as < 1. This formation mechanism, however, cannot explain the high pH and low sulfate concentration of the Great Wall fluid alongside high  $\delta^{34}S$  values of elemental sulfur and massive sulfides found at Kemp. Instead, we suggest that  $S^0$  formation at Kemp Caldera can be attributed to synproportionation of  $SO_2$  and  $H_2S$ . This formation mechanism is thermodynamically feasible but has not been

demonstrated to actually take place in hydrothermal systems. The association of elemental sulfur with covellite is also uncommon, but not unexpected in magmatic-hydrothermal systems. The uncommonly high pH-value is likely responsible for the precipitation of the metal sulfides, which are unusual for known acid-sulfate systems studied to date. Our study shows that the geochemical behavior of sulfur in arc/back-arc hydrothermal systems is more diverse than previously recognized.

*Keywords:* South Sandwich arc; Kemp Caldera hydrothermal system; elemental sulfur; elevated pH; synproportionation

---

#### **4.1 Introduction**

Since the discovery of the Galápagos Spreading Center in the late 1970's, the deep sea has been explored extensively with more and more hydrothermal systems having been discovered. Deep-sea hydrothermal systems are strongly linked to geodynamic processes and volcanic activity. Hence, they are mainly located at mid-ocean ridges (MORs), e.g., at the Mid-Atlantic Ridge, volcanic arcs (e.g., Kermadec arc) and back-arc basins such as the Manus Basin and Lau Basin (Leat and Larter, 2003; Reid et al., 2013; de Ronde and Stucker, 2015; Diehl and Bach, 2020). Compared to MORs, fluids of subduction-related arc and back-arc hydrothermal systems are significantly enriched in metals and magmatic volatiles (e.g., de Ronde et al., 2001; de Ronde et al., 2003; Butterfield et al., 2011; Seewald et al., 2015; Pereira et al., 2022). Their environments are relatively shallow so that temperatures are lower and phase separation results in relatively large variation of Cl concentrations compared to MOR hosted hydrothermal systems (Hein and Mizell, 2013; Kleint et al., 2019; Diehl et al., 2020).

In general, arc- and back-arc-related submarine hydrothermal systems can be divided into two main types: magmatic-hydrothermal systems, in which influxing magmatic vapors provide heat and solutes to the fluids, and seawater-rock-dominated hydrothermal systems, where circulating seawater is heated by and reacts with hot rock in the subseafloor (Reeves et al., 2011; de Ronde et al., 2019; Kleint et al., 2019; Seewald et al., 2019). Magmatic-hydrothermal systems have a direct magmatic input and are characterized by acid-sulfate fluids, which have relatively low temperatures ( $< 250$  °C) and are highly acidic ( $\text{pH} \leq 1-3$ ) (Butterfield et al., 2011; Seewald et al., 2015). They are analogs of fumaroles and subaerial high-sulfidation environments in epigenetic porphyry-related systems (Resing et al., 2007; Seewald et al., 2015). Acid-sulfate fluids are metal-poor and contain oxidized sulfur species (especially  $\text{SO}_2$  and  $\text{HSO}_4^-$ ). Iron oxyhydroxide crusts and advanced argillic alteration assemblages are commonly found in magmatic-hydrothermal systems, while sulfide minerals are rare or even

absent (e.g., de Ronde et al., 2011; Seewald et al., 2019). The term “advanced argillic” refers to mineral associations that can include quartz, pyrophyllite, and alunite formed by alteration of volcanic rocks. Elemental sulfur ( $S^0$ ) is commonly associated with these minerals. Typically, sulfur also precipitates from acid-sulfate type fluids due to the disproportionation of magmatic  $SO_2$  upon cooling and reaction with  $H_2O$  (Kim et al., 2009; Seewald et al., 2015; Seewald et al., 2019). Besides elemental sulfur,  $H_2S$  can also form by disproportionation reactions, which invariably yield sulfuric acid. Isotopic fractionation results in isotopically lighter elemental sulfur and  $H_2S$  and isotopically heavier sulfate than the incoming  $SO_2$ , which is often around 4 ‰ in  $\delta^{34}S$ , but can be as heavy as 10 ‰ (Alt et al., 1993). Hence,  $\delta^{34}S$  values of  $S^0$  and  $H_2S$  are commonly  $< 0$  ‰ (de Ronde et al., 2005; de Ronde et al., 2011; McDermott et al., 2015). By contrast, seawater-rock-dominated hydrothermal systems (commonly seen as a later stage of magmatic-hydrothermal systems; de Ronde et al., 2019) are characterized by seawater-derived hydrothermal fluids with temperatures of  $> 300$  °C, although diffuse venting with lower temperatures ( $< 70$  °C) can also occur (de Ronde and Stucker, 2015). The fluids have pH-values around 3 and are enriched in dissolved metals and reduced sulfur species (e.g.,  $H_2S$ ), but elemental sulfur is typically absent (Seewald et al., 2019). Rapid cooling of these hydrothermal fluids due to mixing with cold seawater or conductive cooling can result in precipitation of typical sulfate-sulfide minerals (including Cu- and Zn-rich phases) on, or beneath, the seafloor (e.g., de Ronde and Stucker, 2015; McDermott et al., 2018; Seewald et al., 2019; Pereira et al., 2022). Common additional minerals are quartz, opaline silica, adularia and clay minerals as well as pyrite, (Fe-rich) sphalerite, galena, tennantite, chalcopyrite and bornite as sulfide minerals (de Ronde et al., 2005). Note that both types of hydrothermal systems involve water-rock interaction processes. Compared to seawater-rock-dominated hydrothermal systems, however, magmatic-hydrothermal systems receive an additional magmatic input and fluids are hence commonly not rock-buffered.

Two large submarine caldera volcanoes have been studied in some detail with respect to their hydrothermal systems: Niuatahi in the NE Lau Basin and Brothers volcano in the Kermadec arc, both host the two types of hydrothermal systems mentioned above (Peters et al., 2021). At Niuatahi (previously known as “Volcano O” or “MTJ-1 caldera”), alunite, silica and fine-grained pyrite were noted along with molten native sulfur, suggesting the formation of acid-sulfate type fluids due to disproportionation of magmatic  $SO_2$  (Kim et al., 2009; Seewald et al., 2019). At Brothers, both massive sulfides and advanced argillic assemblages were found at two different vent sites. The NW Caldera site is characterized by assemblages of chlorite-illite-smectite-barite-sulfides occurring with vent fluid pH-values  $> 3.2$ . By contrast, native sulfur, natroalunite and amorphous silica are dominant at the Upper Cone site where vent fluid pH-values are as low as 1.9 (de Ronde et al., 2005; de Ronde et al., 2011). At the Lower Cone site of Brothers, elemental sulfur is also present but here pH-values are more moderate

(e.g., pH 4–5) (de Ronde et al., 2011; Kleint et al., 2019). However, at both Cone sites, the  $\delta^{34}\text{S}$  values of elemental sulfur deposits are noticeably negative. The molten sulfur from Niuatahi has isotope values ranging from  $-8.2$  to  $-7.5$  ‰ (Kim et al., 2011). At Brothers, Lower Cone  $\delta^{34}\text{S}$  values range from  $-8.3$  to  $-3.9$  ‰ for  $\text{S}^0$  (de Ronde et al., 2005), and from  $-8.0$  to  $-4.8$  ‰ for the Cone vent fluids (de Ronde et al., 2011).

These two main types of hydrothermal systems can also be found in the Kemp Caldera (formerly McIntosh Crater/Caldera). The prominent caldera represents an arc caldera volcano, similar in shape and size to Brothers volcano or Niuatahi; it is the only known submarine arc caldera volcano in the (southern) Atlantic Ocean. The Kemp Caldera was discovered during a geophysical survey by the R/V *James Clark Ross* research cruise JR224 in 2009, and hydrothermal activity was first observed within this submarine volcanic crater (Larter, 2009; Cole et al., 2014). Since then, several biological investigations have been carried out, but from a geochemical, petrological and volcanological point of view, Kemp Caldera is still largely unknown.

This paper provides the first vent fluid compositional and isotopic data as well as mineralogical results of hydrothermal precipitates collected at Kemp Caldera hydrothermal vent fields during the R/V *Polarstern* PS119 expedition in 2019. The focus of this study is on the formation mechanisms of elemental sulfur, which coexists with covellite and pyrite.

## 4.2 Geologic setting and sampling locations

The Kemp Caldera is an arc caldera volcano, which is part of the intra-oceanic South Sandwich arc in the Scotia Sea (Figure 4.1). The Scotia Sea region, situated in the Atlantic part of the Southern Ocean, is an area of oceanic lithosphere (Leat et al., 2000; Barker, 2001). It comprises four interacting plates: the Antarctic and the South American Plate as well as the Scotia and the Sandwich Plate (Pearce et al., 2000; Barker, 2001; Thomas et al., 2003). The South American Plate in the north and the Antarctic Plate in the south enclose the small Scotia Plate and the even smaller Sandwich micro-plate.

Sulfur formation associated with coexisting sulfide minerals in the Kemp Caldera hydrothermal system, Scotia Sea

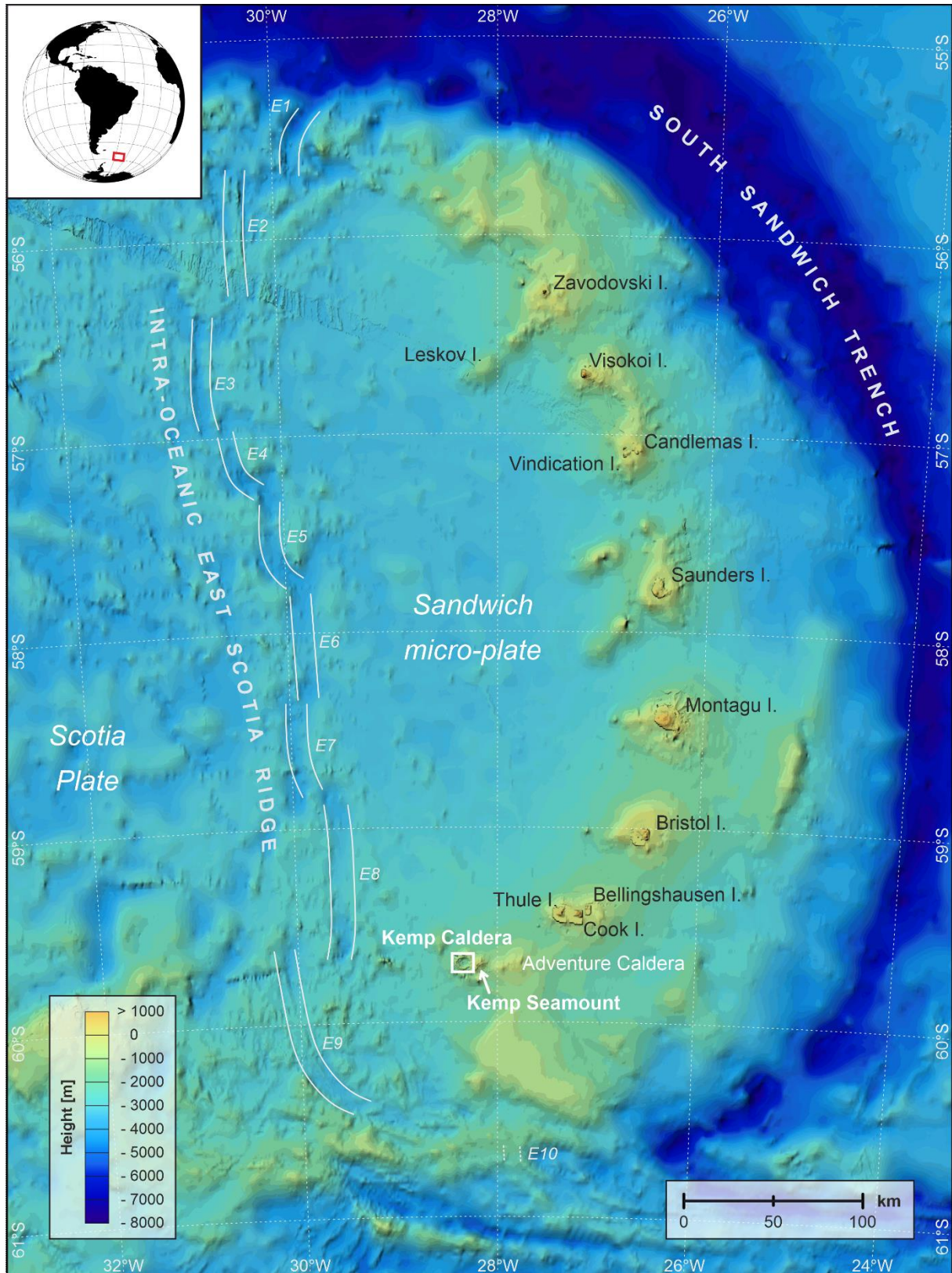


**Figure 4.1.** Bathymetric map of the Sandwich micro-plate with the working area: location of the Kemp Caldera, Scotia Sea. The caldera belongs to the submerged southern part of the South Sandwich island arc.

The entire area is tectonically very active. In the west, the Sandwich micro-plate is separated from the Scotia Plate by the East Scotia Ridge, an active, intra-oceanic spreading center (Figure 4.1) (Bruguier and Livermore, 2001; Larter et al., 2003; Leat et al., 2010; Leat et al., 2016). This spreading is associated with the subduction zone in the east of the micro-plate, where the Sandwich micro-plate overrides the subducting South American Plate (Pearce et al., 2000; Livermore, 2003; Leat et al., 2016). Spreading started about 15 Ma ago and currently has an average spreading rate of about 62–70 mm/a (Larter et al., 1998; German et al., 2000; Bruguier and Livermore, 2001; Thomas et al., 2003; Cole et al., 2014). The crustal lithology has a basaltic to basalt-andesitic composition and belongs primarily to the tholeiitic series (Leat et al., 2000; Fretzdorff et al., 2002). The East Scotia Ridge itself consists of ten segments, from E1 in the north to E10 in the south, each separated by (no stable) transform faults (Livermore, 2003; James et al., 2014; Leat et al., 2016). A number of hydrothermal vent fields are known to be hosted by the back-arc spreading center. Specifically, the segments E2 and E9 are hydrothermally active sites where actively venting chimneys occur (German et al., 2000; Rogers et al., 2012; James et al., 2014; Pereira et al., 2022).

On the eastern side of the Sandwich micro-plate, the South Sandwich Trench is developed. This trench is a result of the westward movement of the South American Plate subducting beneath the Sandwich micro-plate at a rate of 70–85 mm/a (Pearce et al., 2000; Fretzdorff et al., 2002). Older oceanic crust (ca. 80 Ma) of the South American Plate is subducted in the north, while younger lithosphere (ca. 27 Ma) is subducted in the south (Leat et al., 2004; Barry et al., 2006). These age differences are also reflected in the depth of the trench. That is, the South Sandwich Trench is deeper in the north (> 8 km) than in the south (< 7 km), a result of the different dip angle of the subducting plate (Leat et al., 2010; Leat et al., 2016). Colder lithosphere is subducted in the north, causing a steeper dip compared to the south, where warmer, younger crust is subducted (Barry et al., 2006). Dehydration of the subducted slab causes partial melting of the overlying mantle wedge, which gives rise to the formation of the South Sandwich island arc, situated about 120–130 km west of the South Sandwich Trench (Leat et al., 2003; Leat et al., 2013). This island arc consists of eleven volcanic islands, the South Sandwich Islands, and several seamounts (Baker et al., 1964; Holdgate and Baker, 1979; Barry et al., 2006). The rock composition of the South Sandwich island arc varies from basaltic to rhyolitic and ranges from low-K tholeiitic over tholeiitic to calc-alkaline (Larter et al., 1998; Leat et al., 2004; Barry et al., 2006). Hydrothermal activity is also recorded from the South Sandwich island arc, especially in the submarine Kemp Caldera west of Kemp Seamount (Larter, 2009; Cole et al., 2014).

Kemp Caldera is situated in the southernmost part of the South Sandwich volcanic arc. It is located 25 km west of the main arc (represented by Adventure Caldera) in the rear-arc and ~65 km east to the East Scotia Ridge. Without any data, the rock types of the Kemp Caldera are assumed to be the same as for the Kemp Seamount, which is located directly east of the caldera. It mainly consists of tholeiitic basalt and basaltic andesite (Leat et al., 2004; Leat et al., 2013; Cole et al., 2014). The crater has a rim-to-rim extension of roughly 6.5 km from N to S and an E-W width of ~8.6 km (Figure 4.2). The inner caldera floor reaches a depth of about 1600 m whereas the rim depth (with several secondary cones) lies between 800 and 900 m below the water surface. A small volcanic edifice, interpreted as resurgent cone, occurs in the middle of the caldera (Hawkes et al., 2014; Linse et al., 2019). Extinct chimneys and white smoker vent fields like Great Wall or Toxic Castle are located around this cone, but are poorly imaged in the bathymetry of the ship's multibeam data (Tyler, 2011; Cole et al., 2014; Bohrmann, 2019; Linse et al., 2019).

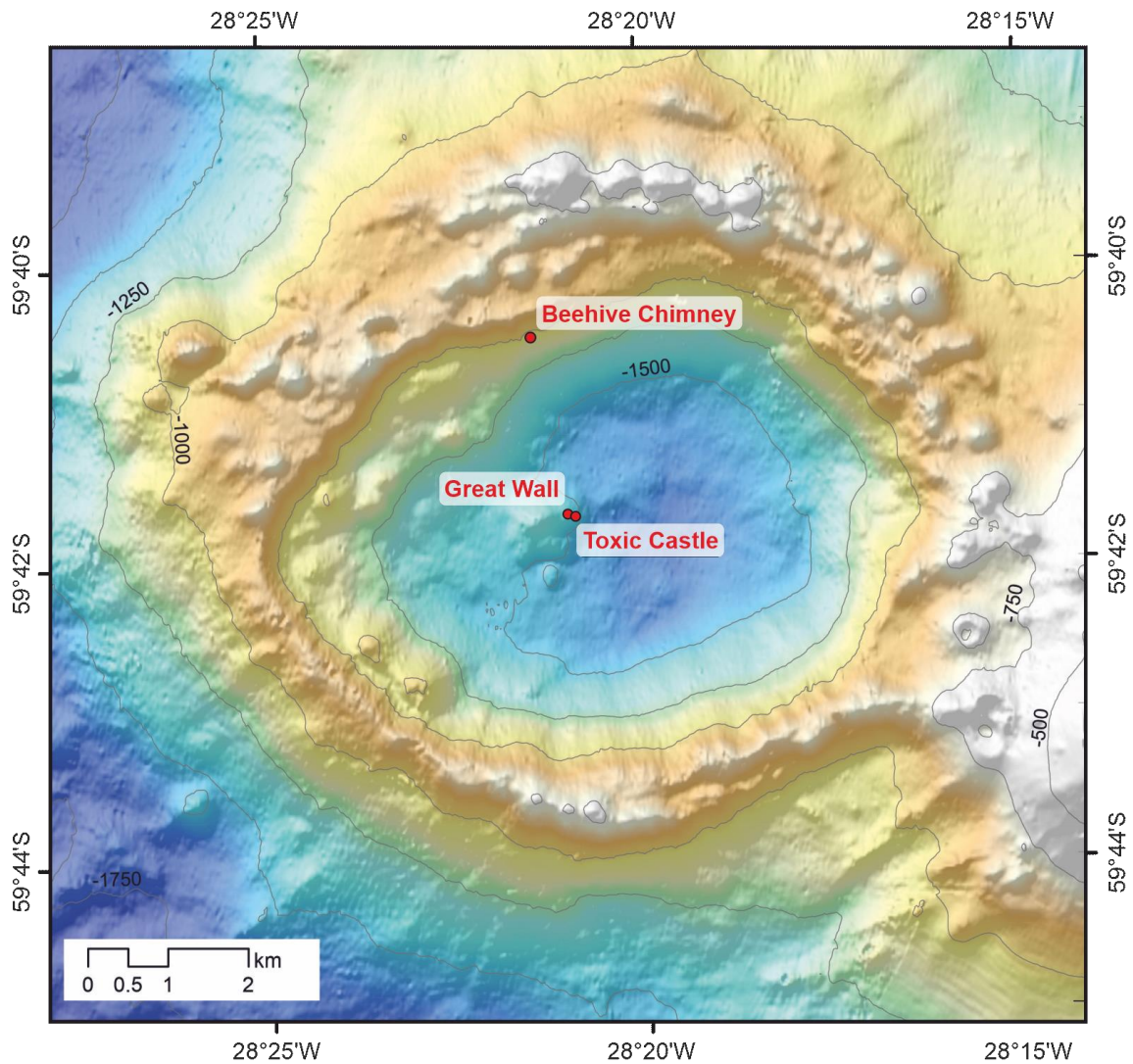


**Figure 4.2.** Bathymetric map showing Kemp Caldera including the sampling locations at Beehive Chimney (59°40.553'S, 28°21.467'W), Great Wall (59°41.678'S, 28°21.095'W) and Toxic Castle (59°41.685'S, 28°21.014'W).

#### **4.2.1 Great Wall**

The Great Wall area owes its name to a < 1 m high wall-like structure, which mainly consists of weathered rock oriented along a seafloor fissure. This structure is partly covered by crystalline elemental sulfur (Cole et al., 2014) and white microbial mats (Rogers, 2010; Hepburn, 2015; Linse et al., 2019). Great Wall is dominated by diffuse fluid flow with relatively low fluid temperatures of 21 to 40 °C (Rogers, 2010; Tyler, 2011; Cole et al., 2014). During the PS119 cruise, temperatures of more than 60 °C were measured at Great Wall.

#### **4.2.2 Toxic Castle**

This site is located at the foot of the eastern flank of the cone. It was previously known as an area of diffuse fluid flow where white smoker structures were found, some of them composed of crystalline, elemental sulfur (Tyler, 2011; Hepburn, 2015). However, during the 2019 research cruise PS119, we measured fluid temperatures > 200 °C (see below). Sulfur occurs in solidified or liquid form around the active vents, dripping out of the rock into the cold seawater. S<sup>0</sup> is also found as crusts on nearby basalt outcrops, or disseminated in the surrounding sediments (Hepburn, 2015).

#### **4.2.3 Beehive Chimney**

Beehive Chimney was discovered during the R/V *Polarstern* PS119 expedition. We detected bubble streaming above the NNW rim of the caldera using the multibeam echo sounder. This area had not been explored by previous expeditions. Using a remotely operated vehicle, an actively venting beehive-shaped chimney was found. The smoke was slightly black, but the expelled fluids were generally very clear. Smaller, white-coated active chimneys are found in close vicinity.

### **4.3 Materials and Methods**

A total of five precipitate samples were collected from the Kemp Caldera during the research cruise PS119 in April/May 2019: one from Great Wall, two from Toxic Castle and two from the newly discovered site Beehive Chimney (Table 4.1), as well as vent fluid samples from these three locations. Samples were collected using the ROV (Remotely Operated Vehicle) *MARUM QUEST 4000*. Comprehensive investigations of these samples were done using geochemical and mineralogical analysis such as XRD, optical light microscopy and SEM-EDX.

**Table 4.1**

Names and positions of sampling locations at the three vent sites investigated in Kemp Caldera and sample numbers.

Location	Ship station	Latitude	Longitude	Water depth	Sample ID	Description
Great Wall	PS119/028	59°41.678'	28°21.096'	1416.3 m	028-7R	Elemental sulfur from the "wall"
	PS119/028	59°41.677'	28°21.095'	1419.5 m	028-8F	Fluid sample
Toxic Castle	PS119/028	59°41.690'	28°21.008'	1422.9 m	028-11R	Small, black chimney from flange structure
	PS119/028	59°41.685'	28°21.015'	1422.8 m	028-17F	Fluid sample
	PS119/028	59°41.685'	28°21.014'	1423.1 m	028-18R	Rock sample with sulfur spherules
Beehive Chimney	PS119/042	59°40.554'	28°21.467'	1128.1 m	042-1F	Fluid sample
	PS119/042	59°40.554'	28°21.467'	1129.7 m	042-2R	Inactive chimney next to Beehive
	PS119/042	59°40.555'	28°21.467'	1139.1 m	042-3R	Small, active chimney next to Beehive

#### 4.3.1 Sampling of precipitates, chimney material and vent fluids

Samples were taken using the ROV either with its hydraulic manipulator arm or by a scoop, then placed in a basket at the front of the vehicle to be transported to the surface. The active chimney at the newly discovered Beehive Chimney location could only be sampled for its vent fluid, however, we were able to sample a smaller chimney located less than 2 m away.

During the ROV dives, fluids were collected with isobaric gas-tight (IGT) hydrothermal fluid samplers. These samplers are made of titanium and can recover up to 150 ml of hydrothermal fluids up to 400 °C (Seewald et al., 2001). A thermocouple was used to measure *in-situ* temperatures of the fluids during sampling. Furthermore, IGT fluid samplers are suitable for determination and quantification of dissolved gases in the hydrothermal fluids because the samplers are gas-tight up to 450 bars and maintain *in-situ* pressure during recovery and later laboratory analysis (Seewald et al., 2001).

For all fluid samples we recovered full IGTs except sample 028-17F from Toxic Castle, where only 2 ml of a diluted fluid could be sampled due to clogging of the nozzle by liquid elemental sulfur.

#### 4.3.2 Chemical analyses of vent fluids

Concentrations of dissolved H<sub>2</sub> were determined onboard by gas chromatography following a headspace extraction. A 7820 Agilent gas chromatograph was used with a Molsieve 60/80 column (Sigma-Adrich, St. Louis, MO) and N<sub>2</sub> as the carrier gas. Hydrogen was measured using a thermal conductivity detector (method adapted after Reeves et al., 2011). The setup was calibrated daily with reference gases of 253 mol-ppm H<sub>2</sub>. For each sample multiple

measurements were performed with the methods precision shown to be better than 5 % relative ( $2\sigma$ ) for the species. Samples for  $\Sigma\text{H}_2\text{S}$  ( $\Sigma\text{H}_2\text{S} = \text{H}_2\text{S} + \text{HS}^- + \text{S}^{2-}$ ) quantification were prepared on board. Fluid aliquots were transferred into evacuated glass vials and acidified with 25 wt% phosphoric acid. The aliquots were sparged with  $\text{N}_2$  gas and  $\Sigma\text{H}_2\text{S}$  was precipitated as  $\text{Ag}_2\text{S}$  following the procedure described in Seewald et al. (2015). Gravimetric measurements were performed post-cruise. The precision of the method is dependent on the quantity of  $\text{Ag}_2\text{S}$  but was always better than 15 % relative ( $2\sigma$ ). Due to low sample volume recovered at Toxic Castle,  $\Sigma\text{H}_2\text{S}$  was analyzed photometrically using the methylene blue method (see Cline (1969) for further details). Measurements of pH were calibrated daily using a “seven2go” pH electrode (Mettler Toledo) immediately after the aliquot was recovered from the sampler and had an analytical uncertainty of better than  $\pm 0.1$  on an absolute level. Concentrations of Mg were determined using inductively coupled plasma optical emission spectroscopy (ICP-OES, Varian Vista Pro, radial plasma observation). Sulfate was determined using ion chromatography (IC, Metrohm Compact IC) with a ‘METROSEP A Supp 5-150/4.0’ column. The analytical uncertainties ( $2\sigma$ ) for Mg and  $\text{SO}_4$  are  $\pm 2$  %. The analyses were conducted at MARUM, University of Bremen.

#### **4.3.3 Geochemical and mineralogical analyses of precipitates**

Reflected light microscopy was the preferred method of the mineralogical identification of the samples. Thus, polished thin sections of selected samples were prepared and examined regarding their mineral phases as well as textural features.

The samples were initially described macroscopically while onboard, photographed and air dried. Once onshore, polished thin sections of select samples were made. We studied these thin sections with a LEICA DMRX stereomicroscope (reflected-light microscopy with plane polarized (ll-pol) and crossed polarized (x-pol) light), and with a SEM-EDX (Zeiss SUPRA 40) for mineral identification as well as textural features. Element mapping was also carried out with the SEM-EDX at the University of Bremen, showing the spatial distribution of elements such as As, Ba, Cu, Fe and S in the sample 028-11R from Toxic Castle.

#### **4.3.4 Sulfur isotopes from fluids and precipitates**

Sulfur isotope measurements were conducted at the WWU Münster. For the measurements, approximately 50  $\mu\text{g}$  of elemental sulfur and 300 to 400  $\mu\text{g}$  of sulfide were homogeneously mixed with 400 to 800  $\mu\text{g}$  of  $\text{V}_2\text{O}_5$  in a tin cup. The measurements were then performed by elemental analyzer isotope ratio mass spectrometry using a Flash EA IsoLink elemental analyzer connected to a Thermo Fisher Scientific Delta V Advantage mass spectrometer. The reproducibility determined by repeated measurements was generally better than 0.3 ‰ ( $1\sigma$ ).

Analytical performance was monitored using international reference materials IAEA-S1, IAEA-S2, IAEA-S3 and NBS 127 as well as lab-internal standards.

#### 4.3.5 Computational methods

SUPCRT92, a software used in calculating standard thermodynamic properties of aqueous species, gases, minerals and reactions (Johnson et al., 1992), was used for the calculation of the standard free energy of the synproportionation reaction over a temperature range from 0 to 300 °C. SUPCRT92 was also used to compute Log K values for a total of 293 acid-based, redox and mineral reactions for a pressure of 25 MPa, which were compiled in a dataset for Geochemist's Workbench (GWB). GWB was used to construct activity-activity diagrams and conduct reaction path model calculations. A Rayleigh fractionation model was constructed to test the likelihood of different reactions for the formation of elemental sulfur in terms of isotopic composition. The fractionation model was conducted as described by McDermott et al. (2015) and Kleine et al. (2021). GWB was used to predict the speciation of sulfur and formation of elemental sulfur as well as the associated isotopic evolution (using the isotope.dat database extended by fractionation coefficients from Table A4.1) along reaction paths of magmatic vapor addition to seawater at elevated temperatures. The key modeling results are presented in the Discussion section; further details about the calculations are provided in the appendix.

### 4.4 Results

#### 4.4.1 Composition of the vent fluids

At Toxic Castle and Beehive Chimney, fluid temperatures range from 207 to 237 °C (Table 4.2). Toxic Castle was previously dominated by diffuse fluid flow (Tyler, 2011), thus has experienced a considerable increase in temperature over an 8 year period. The diffuse-flow area Great Wall is still characterized by relatively low fluid temperatures of 63 °C, although an increase in temperature of 42 °C is observed here over the same time interval (Rogers, 2010). This could be owned to the fact that not the exact same orifice was sampled in the two studies. The lowest pH-value ( $\text{pH}_{25\text{ }^\circ\text{C}} = 2.3$ ) was measured at the NNW caldera rim Beehive Chimney site. The fluids of the white smoker vent fields in the center of the caldera (Great Wall and Toxic Castle site) show moderate pH-values of 5.4 to 5.7 (at 25 °C). However, the high pH of the Toxic Castle fluid is likely due to entrainment of ambient seawater during the comprised fluid sampling (see above). The actual pH-value of the hydrothermal fluid could therefore be lower.

The low Mg concentration of the Beehive Chimney fluid is matched with low concentration of SO<sub>4</sub> (Table 4.2), which is typical for seawater-derived hydrothermal fluids. The sampled fluid at Great Wall contains lower Mg than seawater, but is enriched in Mg relative to Beehive Chimney (almost six times higher). At Toxic Castle, the fluid has a Mg concentration close to that of seawater and a SO<sub>4</sub> concentration higher than seawater values.

Concentrations of dissolved gases (H<sub>2</sub> and ΣH<sub>2</sub>S) vary considerably between the different locations. Relatively low concentrations of H<sub>2</sub>S (2.7 to 4.2 mmol/kg) were measured at Beehive Chimney and Toxic Castle, compared to Great Wall (26.6 mmol/kg). The H<sub>2</sub>S content of the fluids at Great Wall at the time of sampling were more than three times higher than that measured in 2010 (cf. Hepburn, 2015). This difference in concentration and also in temperature may be due to a (temporal) change in the hydrothermal system. The highest H<sub>2</sub> values were measured at Toxic Castle (14.1 μmol/kg), whereas concentrations at Great Wall and Beehive Chimney were equally low at 1.0 μmol/kg.

**Table 4.2**

Measured concentrations of hydrothermal fluids sampled at Kemp Caldera. Concentrations were originally measured in mmol/L and converted to mmol/kg.

Location	Sample ID	T <sub>max</sub> °C	pH <sub>25</sub> °C	Mg mmol/kg	SO <sub>4</sub> mmol/kg	H <sub>2</sub> μmol/kg	ΣH <sub>2</sub> S mmol/kg
Bottom seawater		0.5	7.7	53.2	28.0	0.0	0.0
Great Wall	028-8F	63	5.4	39.1	20.8	1.0	26.6
Toxic Castle	028-17F	207–237	5.7	52.7	30.5	14.1	4.2
Beehive Chimney	042-1F	231	2.3	6.7	3.6	1.0	2.7

#### 4.4.2 Sulfur isotopes

Sulfur isotopic compositions were determined for elemental sulfur, sulfates and H<sub>2</sub>S. The latter was formerly dissolved in the vent fluid and precipitated as Ag<sub>2</sub>S for isotopic measurements (Table 4.3). δ<sup>34</sup>S values for S<sup>0</sup> precipitates are relatively high and range from 5.5 ‰ (liquid sulfur from Toxic Castle) to 5.8 ‰ (fine-crystalline sulfur from Great Wall). The lowest value of 5.2 ‰ was measured from a small sample of liquid sulfur, which clogged the IGT-nozzle while sampling the fluids at Toxic Castle. Considering the analytical error, the δ<sup>34</sup>S values for elemental sulfur are in the range from ca. 5 to 6 ‰.

The isotope signatures for sulfates from Toxic Castle show slightly more positive values than present-day seawater (δ<sup>34</sup>S = 21±1 ‰; Present et al., 2020) with a δ<sup>34</sup>S value of 22.4 ‰. For Beehive Chimney, with 19.9 ‰ the δ<sup>34</sup>S<sub>SO<sub>4</sub></sub> value is less than that of Toxic Castle and present-day seawater.

Sulfur formation associated with coexisting sulfide minerals in the Kemp Caldera  
hydrothermal system, Scotia Sea

**Table 4.3**

Isotopic results of sulfur species of fluid (F) and hydrothermal precipitates (R) from Kemp Caldera.

Location	Sample ID	Analyzed minerals	T <sub>max</sub> °C	pH <sub>fluid</sub>	δ <sup>34</sup> S <sub>S</sub> ‰	δ <sup>34</sup> S <sub>SO4</sub> ‰	δ <sup>34</sup> S <sub>H2S</sub> ‰
Great Wall	028-8F	--	63	5.4	--	--	4.6
Great Wall	028-7R	S <sup>0</sup>	63	5.4	5.8	--	--
Toxic Castle	028-17R	S <sup>0</sup>	207–237	5.7	5.2	--	--
	028-18R	S <sup>0</sup> , barite	207	5.7	5.5	22.4	--
Beehive Chimney	042-2R	Barite	231	2.3	--	19.9	--

δ<sup>34</sup>S measured against VCDT.

### 4.4.3 Mineralogy of vent precipitates

Photographs of individual sample locations as well as representative microphotographs showing cross-sectional views through the chimney structures and detailed (microscopic) images are shown in Figures 4.3 to 4.8. The results of the studied vent precipitates show the range of minerals associated with hydrothermal activity in Kemp Caldera. Minerals associated with the five precipitate samples are summarized in Table 4.4.

**Table 4.4**

Sample locations, sample numbers, temperatures and pH<sub>25 °C</sub> of the fluids, and mineral precipitates found at the Kemp Caldera locations.

Location	Sample ID	T <sub>fluid</sub> °C	pH <sub>fluid</sub>	Minerals
Great Wall	028-7R	63	5.4	S <sup>0</sup>
Toxic Castle	028-11R	--	--	Anh, Bar, Bn, Cc, Cpy, Cv, (Mar, Py), Ten
	028-18R	207	5.7	Anh, Bar, Cv, Sph, S <sup>0</sup>
Beehive Chimney	042-2R	231	2.3	Bar, Mar, Sph
	042-3R	231	2.3	Bar, (Bn), Cpy, Mar, (Py), Sph

Abbreviations: Anh = anhydrite, Bn = bornite, Bar = barite, Cc = chalcocite, Cpy = chalcopyrite, Cv = covellite, Mar = marcasite, Py = pyrite, Sph = sphalerite, S<sup>0</sup> = elemental sulfur, Ten = tennantite. The minerals written in brackets are accessory minerals at the respective locations.

#### *Great Wall*

The sample collected from Great Wall (028-7R) is dominated by fine-crystalline sulfur (Figure 4.3). However, the “wall” of Great Wall is not entirely composed of elemental sulfur. Rather, it is made up of a volcanic neck composed of hydrothermally altered rock which is covered in several places by a sulfur crust.

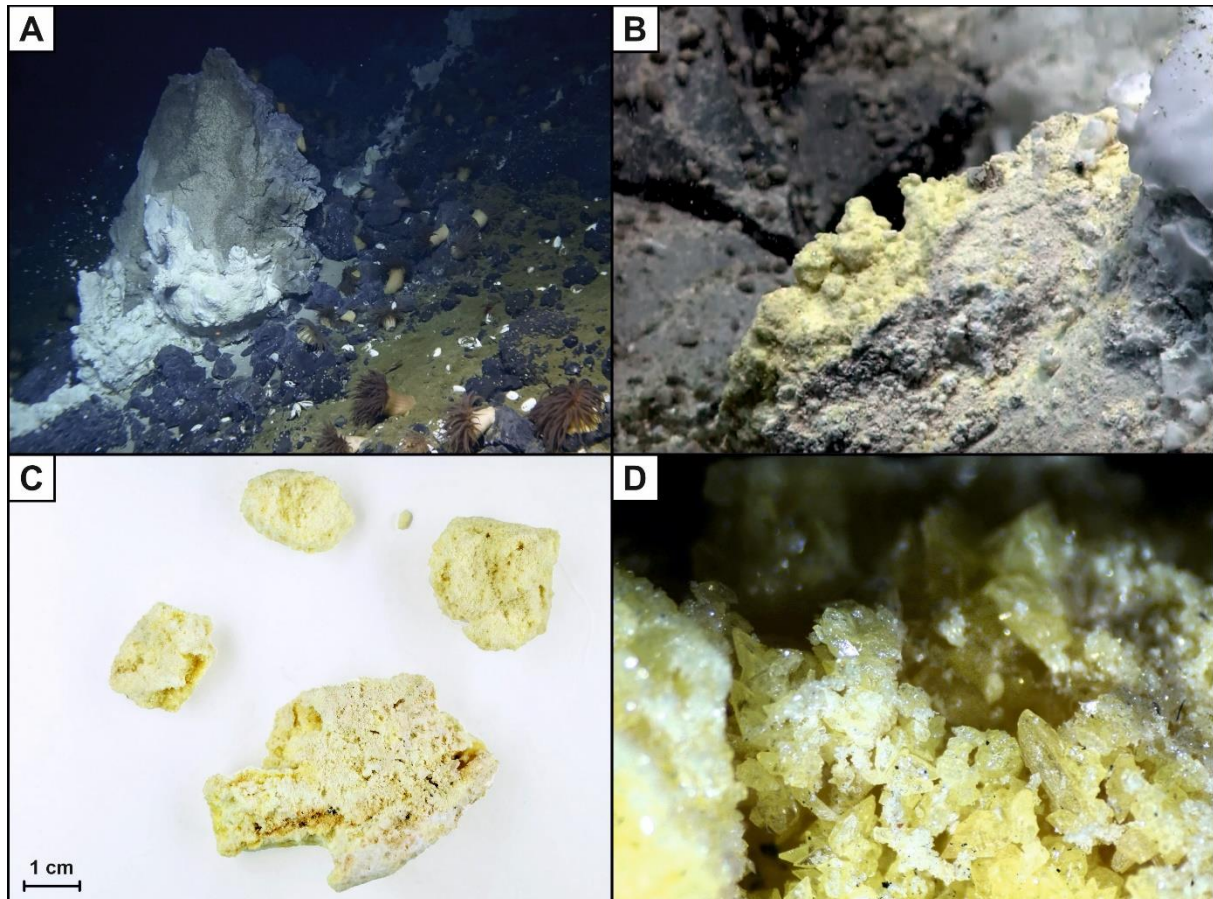


**Figure 4.3.** A) View of the wall-like structure from Great Wall surrounded by blocks of basalt, B) Close-up of the actively venting site where the sample was taken. Altered volcanic rock covered with limpets can be seen in the background, C) Sample 028-7R which was taken directly from the wall structure, and D) Close-up of the crystalline elemental sulfur.

#### *Toxic Castle*

A small chimney (028-11R) was sampled from a flange structure at the Toxic Castle site and is mainly composed of bornite (Figure 4.4). While no distinct layers are recognizable, a slight mineral zonation is visible where the outermost part is composed of barite and anhydrite, whereas the inner part of the chimney is dominated by Cu-bearing sulfide minerals such as bornite, chalcopyrite, covellite and tennantite.

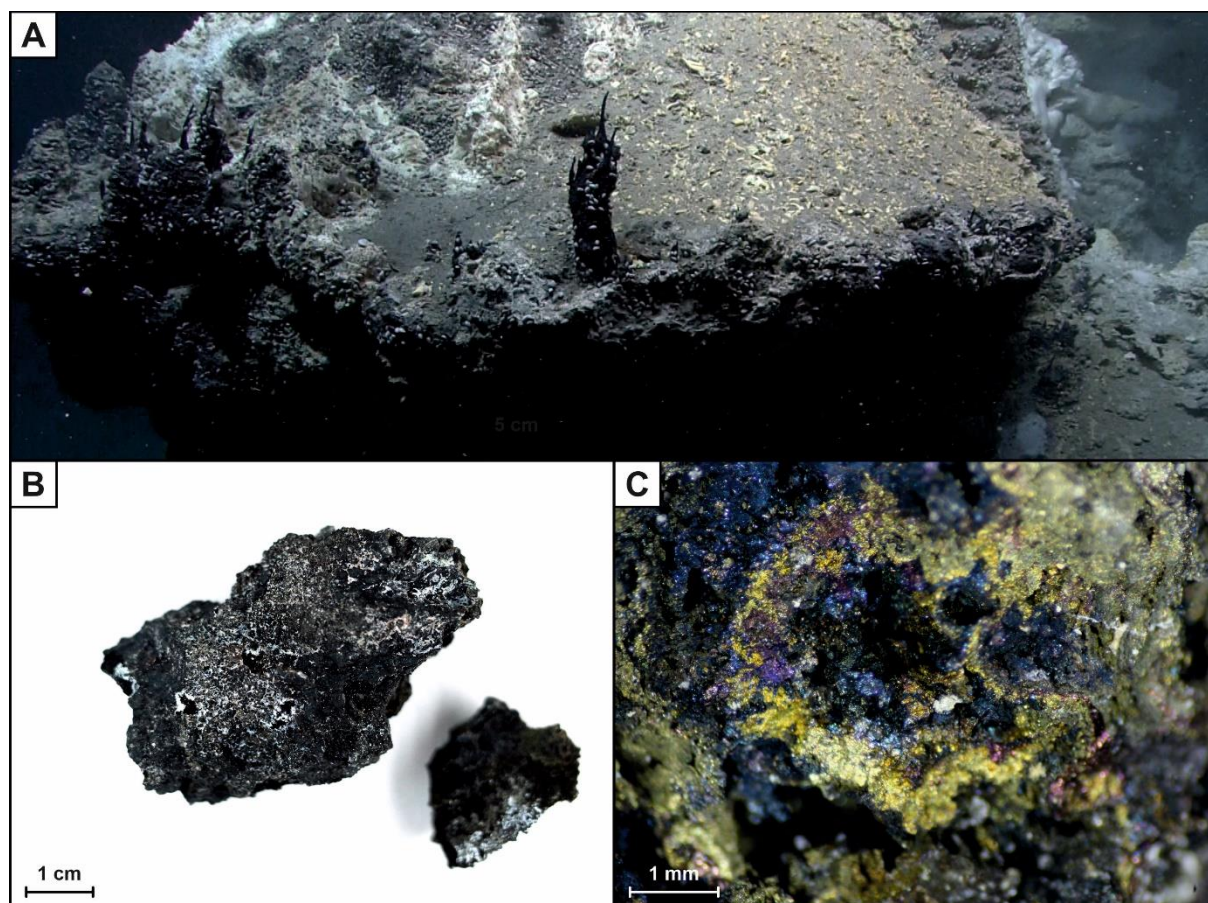


**Figure 4.4.** A) Underwater photo of the flange structure with the small black chimney on top, which was later sampled, B) Close-up of the small chimney sample shown in (A). Partial remains of the barite crust (white patches) are visible, and C) Close-up view of the chimney's center. The Cu-bearing sulfide minerals are clearly visible as iridescent tarnish colors.

The center of the chimney is highly porous with the texture becoming more massive towards the chimney margins. The innermost part is dominated by bornite, covellite and tennantite. Covellite is preferentially found within cavities and cracks and replacing bornite along grain boundaries. Tennantite occurs as near-cubic crystal accumulating in close vicinity to, or within, the cavities. However, covellite and tennantite are rarely seen together. Chalcopyrite becomes more dominant near the exterior of the chimney. With increasing distance from the chimney center, large chalcopyrite lamellae (on average 18–60  $\mu\text{m}$  long) occur as oleander-leaf shaped intergrowth within a bornite matrix, commonly surrounded by chalcocite (Figure 4.5). Bornite is not only formed by the replacement of chalcopyrite, but is also itself replaced by chalcocite. Towards the chimney margins, alteration from bornite to chalcocite intensifies and, in some places, chalcocite itself is altered to covellite. Only in the outermost part of the chimney rare pyrite and marcasite is found. Pyrite occurs as small (< 25  $\mu\text{m}$ ), euhedral to subhedral crystals. It acts as a nucleus for the precipitation of marcasite which crystallizes in a radial orientation around the pyrite grains.

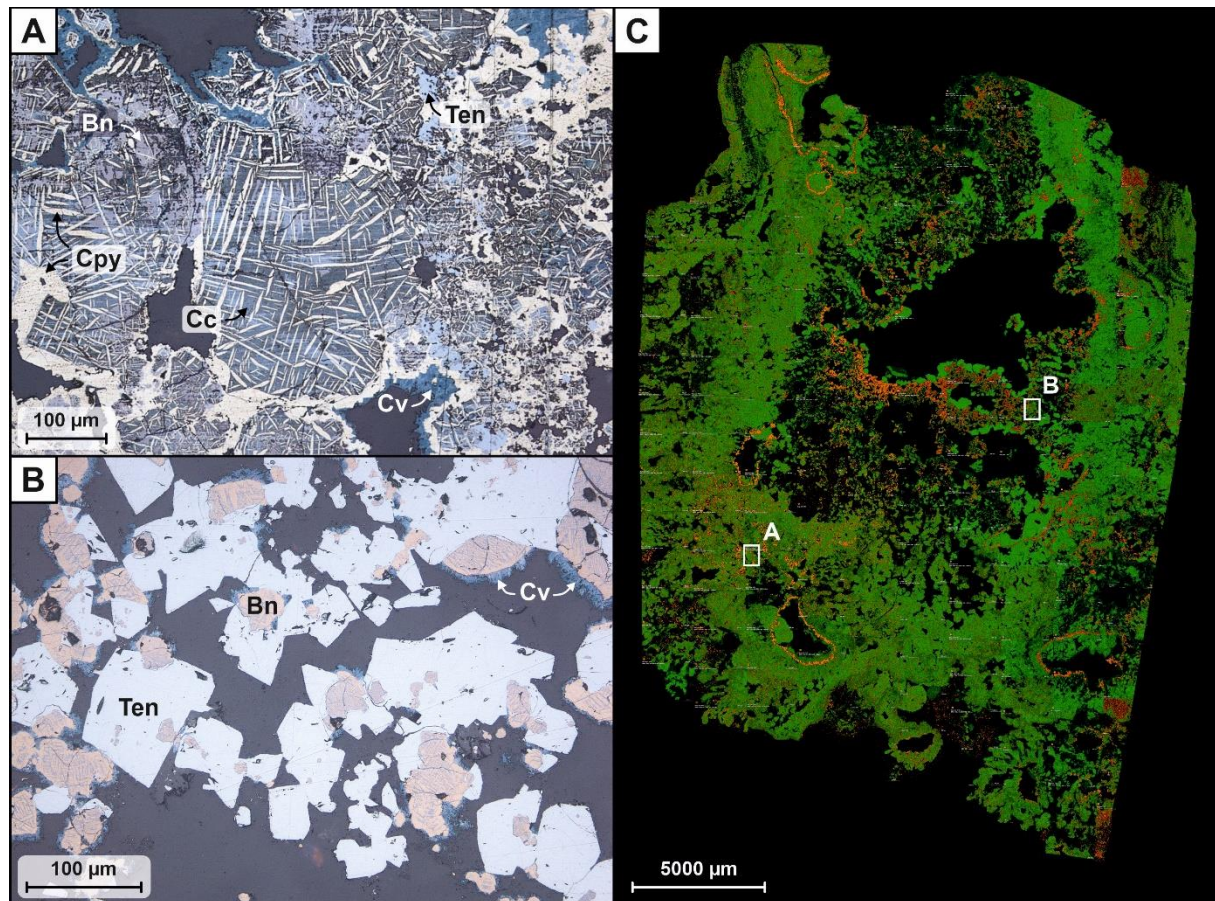


**Figure 4.5.** Microscopic images from a thin section made from the small chimney sampled at Toxic Castle (see Figure 4.4A). The thin section was made from a central cross section through the chimney to check for possible zonation. A) Photomicrograph taken under plane polarized (Il-pol), reflected light. Bright golden yellow chalcopyrite (Cpy) lamellae within a pink-brown bornite (Bn) and whitish blue chalcocite (Cc) matrix. Indigo covellite (Cv) was found along grain boundaries, in cavities and cracks, while light gray tennantite (Ten) is mainly seen near cavities, B) Pink and gray tennantite-bornite associations with covellite seen at grain boundaries of bornite, and C) SEM-EDX image of the element mapping for Cu (green) and As (orange). Copper-rich domains are rich in bornite, chalcocite, chalcopyrite and covellite whereas tennantite is abundant in the orange domains. The outlined areas (A) and (B) are locations for the abovementioned thin sections.

A second sample (028-18R) was taken from Toxic Castle, less than 10 m from where 028-11R was collected. A special feature of this site is the occurrence of liquid sulfur. We observed the sulfur dripping into the surrounding seawater, forming small sulfur spherules and pearl-like structures (Figure 4.6). Covellite was also found at this location, where it is enclosed by a sulfur matrix. Covellite rarely forms well-shaped crystals, however, here it crystallizes into thin hexagonal and tabular plates. Barite and less anhydrite are found only in patches as rosette-like aggregates. The sample is encrusted with a brownish layer which we believed to be Fe-oxhydroxides, however, iron is completely absent with only sphalerite found in the sample as crust.

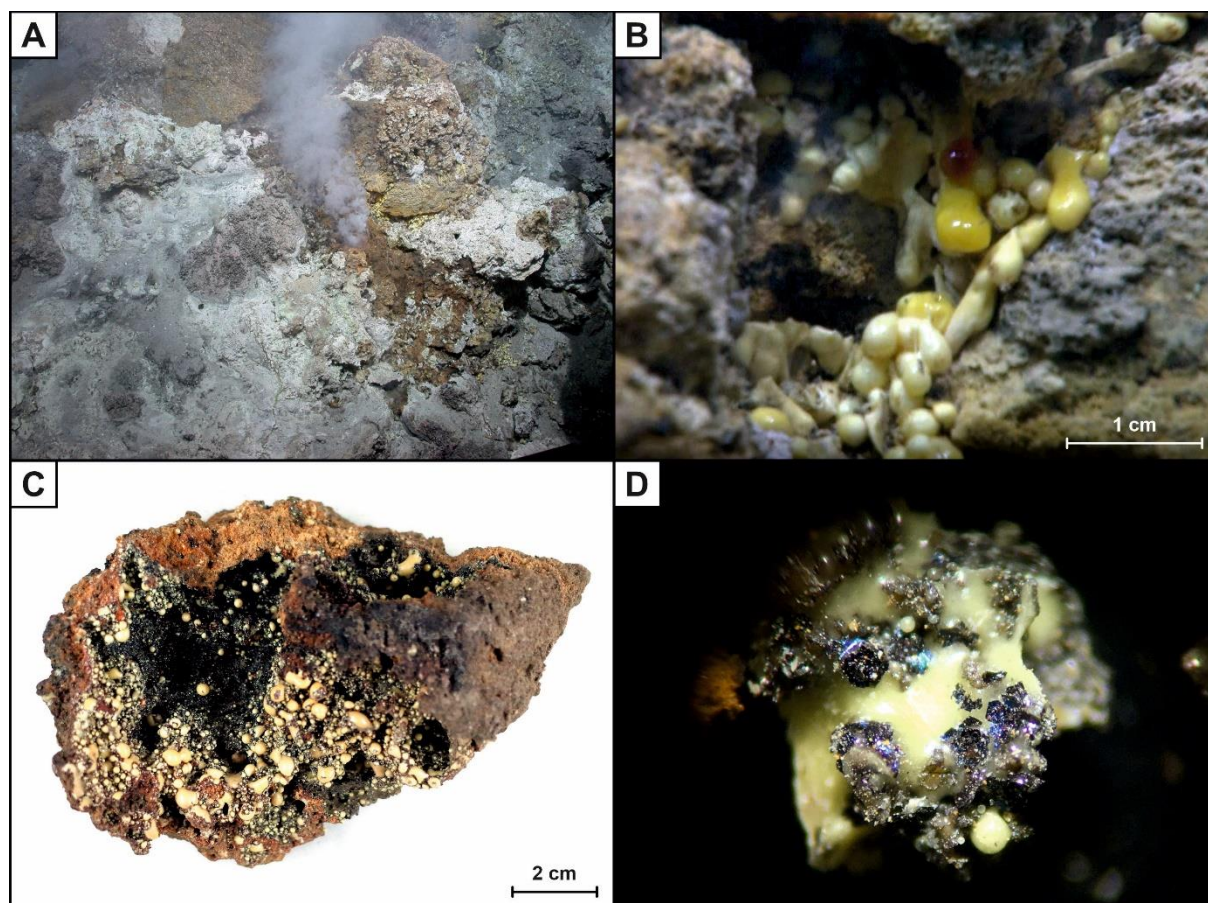


**Figure 4.6.** Elemental liquid sulfur at Toxic Castle. A) Oblique plan view of a white smoker in Toxic Castle with droplets of elemental sulfur on the exterior of the mound, B) Liquid sulfur dripping out of the rock and changing color from blood red to yellow while rapidly cooling, C) Sample 028-18R recovered from Toxic Castle covered with solidified drops of sulfur, and D) Covellite crystals enveloped by the quenched sulfur.

#### *Beehive Chimney – NNW caldera rim*

At this site we found an actively venting beehive-shaped chimney (Figure 4.7A). The fluids discharging at this site were generally clear, although showed a hint of gray smoke. Compared to the other sample locations, the fluid at this location had the highest stable temperature at 231 °C. Fluid sampling was successful here, but unfortunately sampling of the beehive-shaped chimney was not achieved. However, we found smaller white-coated chimneys nearby (Figure 4.7) and sampled one of these.

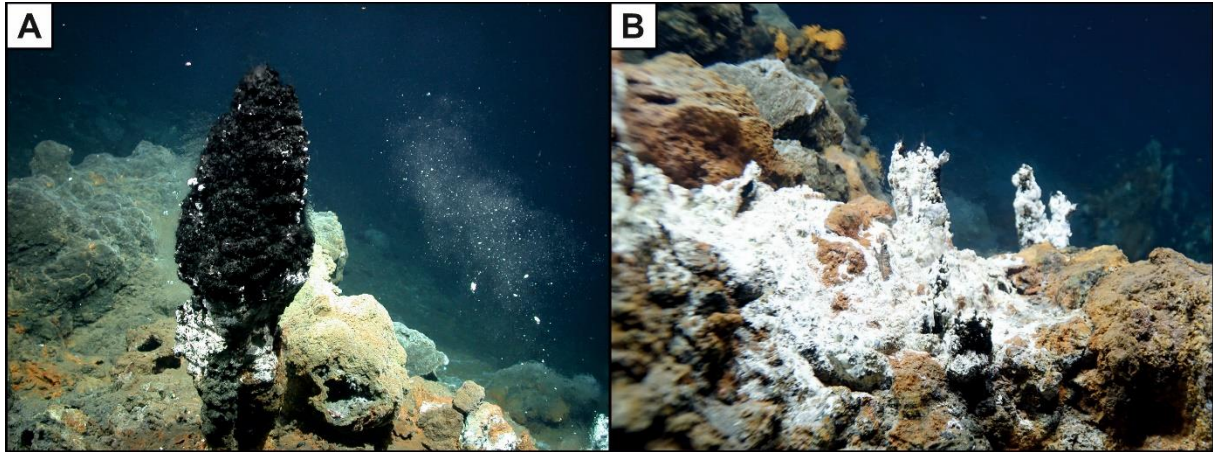


**Figure 4.7.** Beehive Chimney site located on the NNW caldera rim. A) Clear to slightly gray venting of Beehive Chimney, and B) White-coated actively venting chimney in close proximity (< 2 m away) to Beehive Chimney. One of these small chimneys (042-3R, left-hand side) was sampled and analyzed for its geochemistry and mineralogy.

The outer wall of the small chimney (042-3R) at the Beehive Chimney site consists predominantly of barite. Smaller, rosette-like aggregates of this mineral occur throughout the thin section and bigger, lath-shaped crystals are found in most of the cavities. The chimney is highly porous and has several bigger (1 to 8 mm in diameter) cavities. The inner part is dominated by fine-grained, granular chalcopyrite. At some smaller voids, chalcopyrite forms a thin layer as “cavity coating”. Chalcopyrite becomes intergrown with marcasite near the cavities, resulting in a colloform textured chalcopyrite-marcasite layer (Figure 4.8A). Towards the chimney margin, chalcopyrite grades into marcasite which appears as cockscomb-shaped crystals with an iridescent tarnish (Figure 4.8B). Bornite is found in this layer as well, but only in two places, locally replacing chalcopyrite. A thin but distinct layer near the chimney’s exterior is made up of colloform marcasite and disseminated sphalerite, given by a distinct marcasite-barite transition (Figure 4.8C); the outermost layer is dominated by barite. Pyrite is found only in patches as euhedral to subhedral crystals adjacent to the cavities within the small chimney, or close to the outer margin.

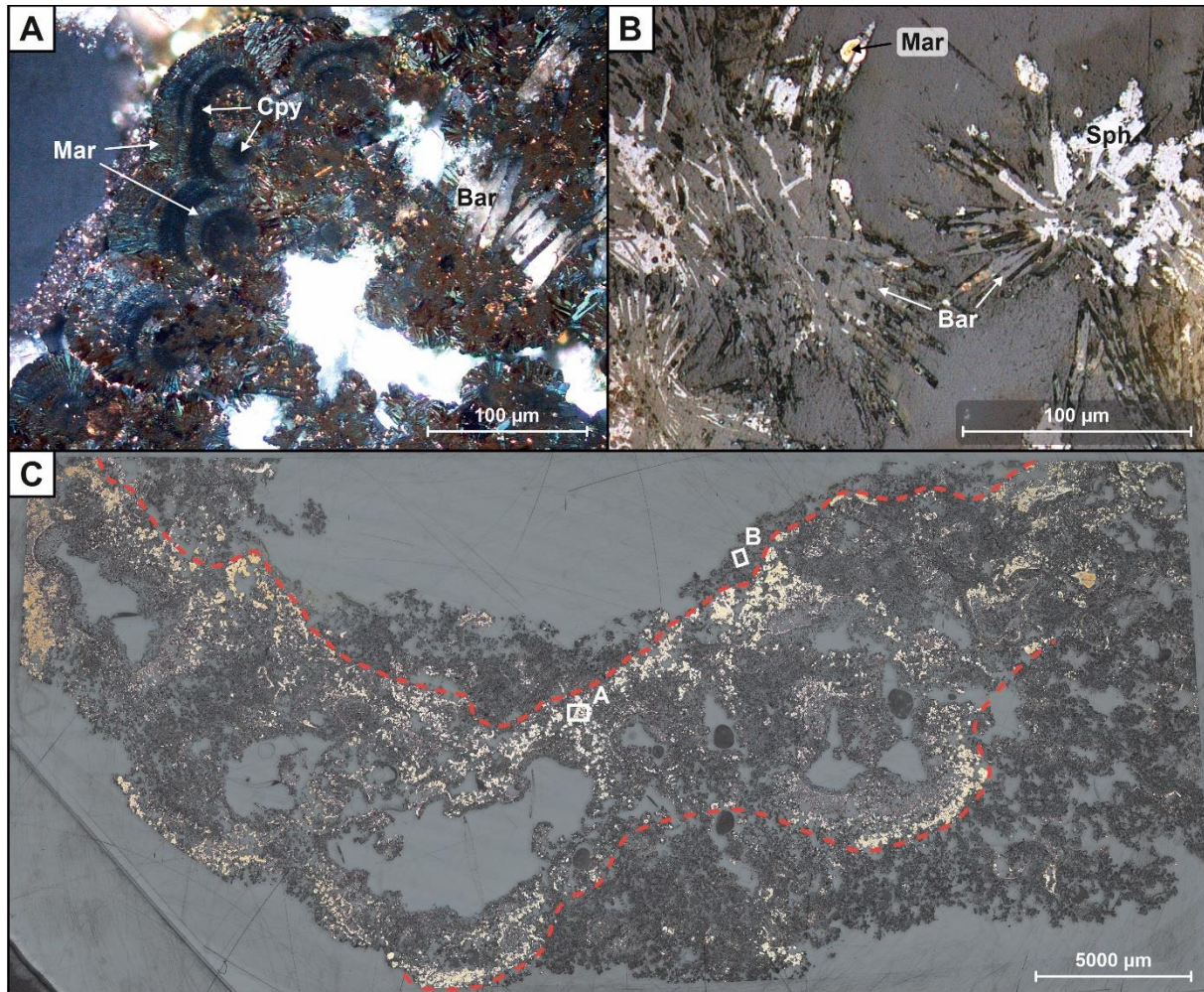


**Figure 4.8.** Detailed and larger-scale microscopic images of the thin section made from the small chimney recovered from the Beehive Chimney site. A) Colloform chalcopyrite-marcasite layer with whitish barite laths (Bar) in between. Chalcopyrite appears dark blue-gray under cross-polarized reflected light, while marcasite shows its typical anisotropy effect with colors ranging from pale to dark green, B) Detailed microscopic image under II-pol reflected light. Dark gray barite crystals (Bar) in rosette-like aggregates with disseminated, light gray sphalerite (Sph). Rare, pale yellow marcasite (Mar) also occurs in the outer part of the chimney, and C) Wider microscopic image of the thin section made from sample 042-3R. Reflected light (II-pol). The inner part, marked by the dashed line, is dominated by chalcopyrite interspersed with marcasite towards the exterior, while the chimney's outer part consists of barite and dispersed sphalerite. Areas shown in (A) and (B) are marked in this photograph.

## **4.5 Discussion**

### **4.5.1 Mineral zonation and mineral patterns of small chimneys**

The chimney samples recovered from Toxic Castle and Beehive Chimney sites show similarities to the typical mineral zonation pattern observed in other black smoker chimneys (cf. Graham et al., 1988; Tivey, 1995; Berkenbosch et al., 2012; James et al., 2014). Anhydrite and especially barite form the outermost layer of the small chimney 028-11R from Toxic Castle (Figure 4.9A). However, only a thin layer of barite wall exists due to dissolution processes and replacement by subsequently precipitating sulfides in the chimney's center, or because the chimney grew so quickly it did not have time to form a sulfate-rich rim (cf. Berkenbosch et al., 2012). A common feature that can be seen throughout most of the cross-section of this sample is the replacement of chalcopyrite by bornite and later chalcocite. It appears that near the chimney exterior "early" chalcopyrite was replaced by bornite. Here, Bn occurs mainly as small to medium-length lamellae (7–25  $\mu\text{m}$ ) surrounded by chalcocite. Later, secondary chalcopyrite lamellae have then formed that are intergrown with bornite. This exsolution and overgrowth texture occurs in the form of oleander-leaf shaped intergrowths (Figure 4.5 and 4.9B). In the chimney's center, chalcopyrite is entirely replaced or overgrown by bornite (Figure 4.9C).

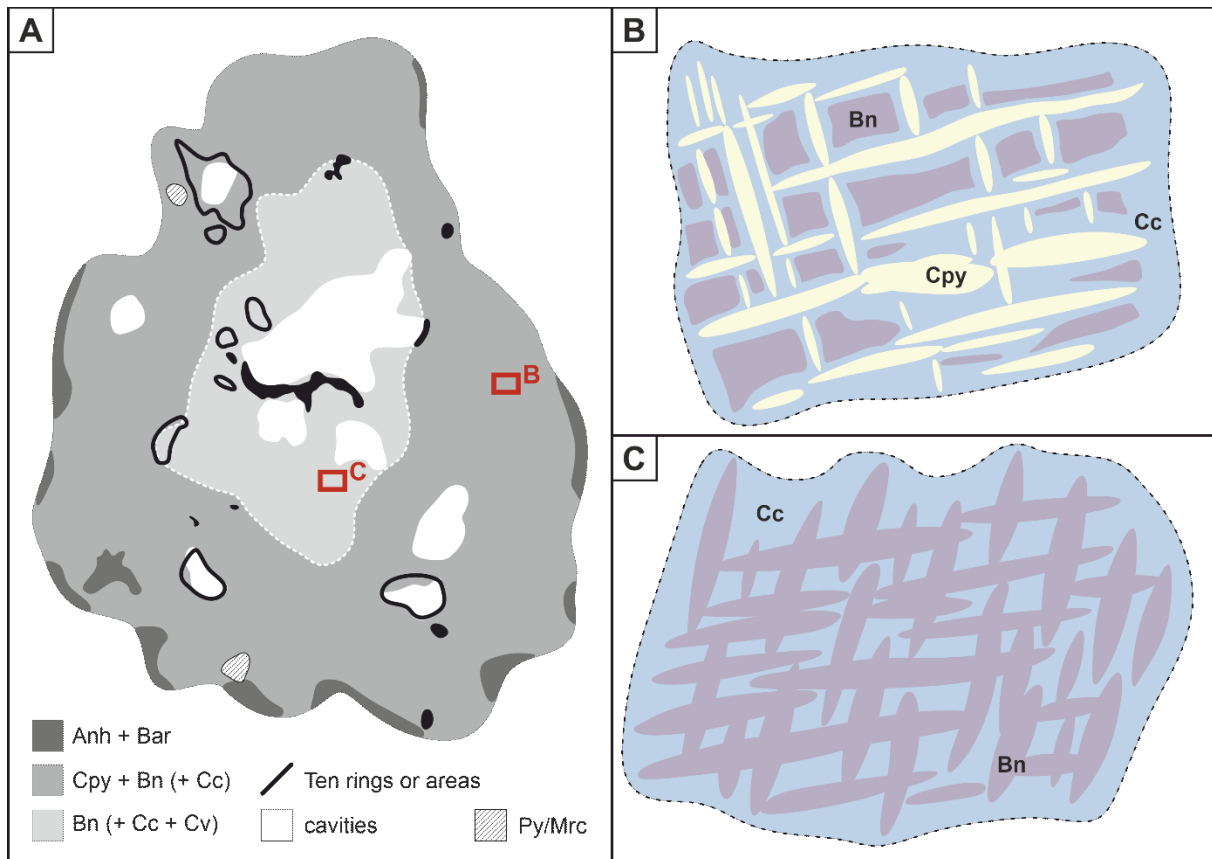


**Figure 4.9.** Sketch of the zonation and mineral patterns of the small 028-11R chimney from Toxic Castle. A) The center of the chimney is highly porous (inner part of the white dashed line) and consists mainly of bornite (Bn) partly replaced by chalcocite (Cc). Tennantite (Ten) accumulates around or within the cavities, while tiny covellite crystals (Cv) are found within cracks. Towards the outside, the texture becomes more massive. This layer is made of chalcopyrite (Cpy), which is partly replaced by bornite and later chalcocite. The outermost layer is mainly formed by barite, B) Observed Cpy-Cc-Bn texture in form of oleander-leaf shaped intergrowth, and C) Mineral pattern in the chimney's center. Bornite and later chalcocite have replaced the chalcopyrite with the same oleander-leaf shape texture.

Copper typically replaces iron in pre-existing sulfide minerals in reduced environments (Zhao et al., 2014a). The replacement of chalcopyrite or bornite by chalcocite and covellite is a consequence of this process (Amcoff, 1988; Li et al., 2018). The released iron is then transported to the outer, more oxidizing parts of the chimney, where it is re-precipitated as sulfide minerals in the form of pyrite or marcasite (Graham et al., 1988).

The replacement of chalcopyrite by bornite and chalcocite could happen at ambient seafloor temperature after hydrothermal flow ceased or after the chimney collapsed. Oxidation would transform chalcopyrite into Cu-oxide or sulfate, and bornite and chalcocite would then represent intermediate phases of this oxidation process. As chimney 028-11R from Toxic Castle was actively venting prior to its recovery, oxidative alteration of chalcopyrite to bornite and chalcocite can likely be ruled out.

The transition from chalcopyrite to bornite and chalcocite can also happen at high temperatures while the chimney is still active. High  $H_2$  and  $H_2S$  activities in the conduit of the discharging hydrothermal fluids would result in chalcopyrite stability. Hydrogen and  $H_2S$  activities in seawater surrounding the chimney are exceedingly low. An advective-diffusive gradient will establish itself between the inner conduit and the outer wall of the chimney. Advection of vent fluids is usually not fast enough across the chimney walls although diffusive losses of  $H_2$  and  $H_2S$  from inside to outside the chimney are to be expected (Tivey, 1995). Figure 4.10 shows that constant  $f_{S_2}$  is maintained when  $H_2$  and  $H_2S$  diffuse at the same rate. As  $H_2$  can be expected to diffuse faster than  $H_2S$ , the actual gradient in  $H_2$  and  $H_2S$  activities across the chimney wall may be a little steeper than the isopotentials shown in Figure 4.10. Regardless, our results show that the expected diffusive gradient in dissolved gases alone is enough to generate the observed replacement reaction sequence and hence the observed zonation. The idea of these reactions happening at high temperatures can explain why Zhao et al. (2014b) always observed the chalcopyrite-bornite reaction in the 200–320 °C range. This gradient across the chimney wall drives the solution-controlled dissolution and precipitation process proposed by Zhao et al. (2014b).

The onset of mineral zonation can also be observed in sample 042-3R from Beehive Chimney. The outer barite wall protects the sulfide minerals in the center of the small chimney and preserves higher temperatures in the inner part (cf. Berkenbosch et al., 2012). At the Beehive Chimney site, predominantly marcasite occurs as iron sulfide towards the chimney exterior, not pyrite (Figure 4.8). The precipitation of marcasite is pH- and temperature-dependent and represents the metastable phase of pyrite at temperatures above 150 °C (Fleet, 1970; Schoonen, 2004). While only pyrite is formed at pH-values above 6, marcasite primarily precipitated from more acidic solutions with  $pH < 4$  (Schoonen and Barnes, 1991; Schoonen, 2004; Kürzinger, 2019). This is consistent with the measured  $pH_{25\text{ °C}}$ -value of 2.3 at this location.

The co-occurrence of elemental sulfur and metal sulfides is rather uncommon. The fluids at the Great Wall site have very high  $H_2S$  and low  $H_2$  contents, which equates to very high sulfur fugacities (Figure 4.10). This is a hallmark of magmatic-hydrothermal systems where native sulfur is often observed (de Ronde and Stucker, 2015). Our calculations show that sulfur fugacities  $> 10^{-5.66}$  bar are needed to have liquid sulfur become stable at 200 °C. The stable assemblage in the Cu-Fe-S-O-H system is sulfur next to CuS and  $FeS_2$  phases. Below the bold sulfur fugacity line,  $S^0$  is stable and coexists with covellite and pyrite (Figure 4.10). This matches our observation.

In general, magmatic-hydrothermal systems are dominated mainly by elemental sulfur, Al-rich sulfates, silica, Fe-oxyhydroxides, clay minerals as well as pyrite/marcasite as the only representatives of sulfide minerals (Hedenquist et al., 2000; Resing et al., 2007; de Ronde and Stucker, 2015). Other sulfide minerals are rare or absent. However, Cu-Zn-(Au) mineralization characterizes the water-rock-dominated hydrothermal system, while  $S^0$  does not occur or only in extremely small quantities. But coexistence and paragenesis of elemental sulfur together with sulfide minerals are reported in previous studies. For example, Kim et al. (2011) reported the occurrence of covellite, pyrite and small quantities of tennantite enclosed in a sulfur matrix. Pyrite is a sulfide mineral that not uncommonly occurs together with trace metals in (molten) sulfur mainly in subaerial hydrothermal systems (de Ronde et al., 2015; Mandon et al., 2020). Something similar can be observed in the Kemp Caldera. Despite the distinction between magmatic- and water-rock-dominated hydrothermal systems (also due to the different temperatures and pH ranges), elemental sulfur and (Cu-bearing) sulfides can coexist. The crucial factors here are temperature and sulfur fugacity. Different sulfide mineral assemblages require lower or higher sulfur fugacities to form (Lusk and Bray, 2002). Clearly, there is the possibility that covellite at Toxic Castle originates from the nearby Bn-Cpy-Cv chimneys. The covellite could have been picked up by the molten sulfur on its way to the seafloor, where it is now embedded in a sulfur matrix. However, the diagram in Figure 4.10 shows that paragenesis of the named minerals is possible, and sulfur can form together with pyrite, covellite and even bornite.

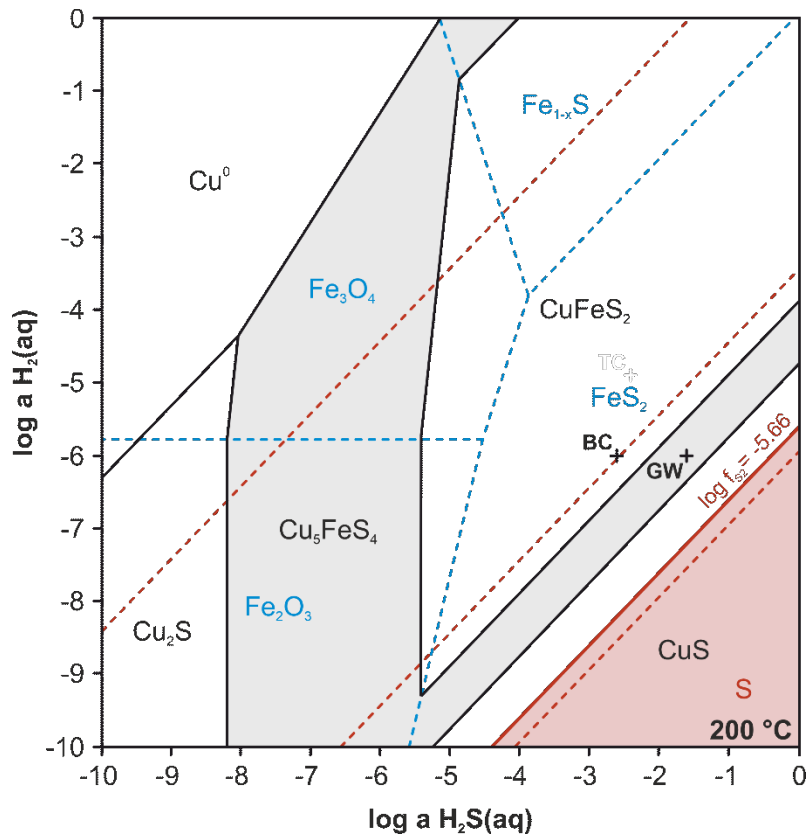


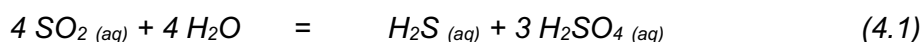
**Figure 4.10.** Log a H<sub>2</sub> – log a H<sub>2</sub>S diagram showing stability fields of Fe- and Cu-bearing (sulfide) minerals and S<sup>0</sup>. Reported fluid data from Great Wall (GW) and Beehive Chimney (BC) are plotted in this figure. Fluid data from Toxic Castle are not displayed because of the compromised sample due to seawater entrainment. Stability fields of the mineral phases were calculated with GWB for 200 °C and 250 bar. The black lines mark the stability fields of the Cu-bearing minerals, the dashed lines in blue indicate iron sulfides and oxides. The red areas show the stability fields of the elemental sulfur, and the dashed lines are the isopotentials (log f<sub>S<sub>2</sub></sub> = –20, –10, –5). Below the bold red line (log f<sub>S<sub>2</sub></sub> = –5.66), sulfur is stable (red-colored area) and can occur in paragenesis with covellite (CuS) and pyrite (FeS<sub>2</sub>). Bornite (Cu<sub>5</sub>FeS<sub>4</sub>; gray area) is just above the main stability field of sulfur, so under favorable conditions bornite can occur in paragenesis with S<sup>0</sup>. Note that for Great Wall the stability fields look different due to the lower temperature of only ~70 °C. The GW data would then lie within the sulfur stability field.

#### 4.5.2 Formation of elemental sulfur

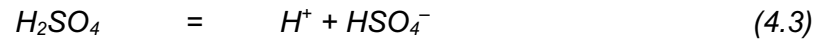
In the Kemp Caldera, sulfide minerals coexist and may occur in paragenesis with elemental sulfur, as previously discussed. The sulfur is a special feature of Kemp due to its formation conditions and is found at Great Wall and Toxic Castle. These two sites are < 80 m apart, but nevertheless, S<sup>0</sup> occurs in different forms. At Great Wall, the sulfur is fine-crystalline, while at Toxic Castle it appears in liquid form at the seafloor. An obvious difference between these two locations and an explanation of the different appearance of S<sup>0</sup> is temperature. That is, Great Wall is dominated by diffuse fluid flow with maximum temperatures of 63 °C which causes the crystallization of orthorhombic sulfur. At Toxic Castle, the white smoker vent fluids can reach temperatures of more than 200 °C, which is above the melting point of sulfur and which is why it occurs there in liquid form. Moreover, pH-values of the fluids where the sulfur is found (at

Great Wall and Toxic Castle) are remarkably high ( $\text{pH}_{25\text{ }^\circ\text{C}} > 5$ ). The fluid venting at Great Wall have high Mg concentrations (39.1 mmol/kg). These high Mg concentrations could be a result of either sub-surface mixing prior to venting or a result of seawater entrainment while sampling. It is however unlikely that huge volumes of seawater were entrained during sampling since a steady temperature reading was recorded. These high Mg values at Great Wall rather reflects sub-surface mixing of hydrothermal fluids with bottom seawater. Samples collected in 2010 at Great Wall show similar high Mg concentrations (50.1 mmol/kg), although are much higher than that sampled in 2019 (Cole et al., 2014). This sub-surface mixing of seawater would result in the high pH-value measured at this site. Although the fluid collected at Toxic Castle may be compromised by possible seawater entrainment during sampling, the  $\text{SO}_4$  concentration (30.5 mmol/kg) higher than that of bottom seawater clearly shows that sulfate was not removed, as is the case for Beehive Chimney, but added to the vent fluid. Acid-sulfate fluids can have sulfate concentrations that are much higher than 28 mM, i.e. seawater (Seewald et al., 2015). Butterfield et al. (2011) have shown that the excess sulfate is derived from disproportionation of sulfite, which was added to the system by the influx of  $\text{SO}_2$  through a magmatic vapor. Where these high sulfate concentrations have been observed in vent fluids before, disproportionation of sulfite resulted in very low pH-values of around 1 and lower (Butterfield et al., 2011; Seewald et al., 2015). These low pH-values are inconsistent with the high pH measured in the Great Wall and Toxic Castle fluids, although a lower pH at Toxic Castle cannot be ruled out due to the poor quality of the fluid sample. The isotopic compositions of  $\text{S}^0$  and barite are also inconsistent with  $\text{SO}_2$  degassing and disproportionation (see below). The high sulfate concentration is hence suggested to be caused by dissolution of sulfate-bearing minerals in the sub-surface. Sulfate minerals that precipitate at relatively high temperatures (e.g., anhydrite at temperatures  $> 150\text{ }^\circ\text{C}$ ) and dissolve as the system cools, resulting in a  $\text{SO}_4$  concentration in the fluid higher than seawater (de Ronde et al., 2011; Kleint et al., 2019).

The formation of native sulfur is a signature feature of hydrothermal systems influenced by magmatic degassing. Typical volatiles derived from magma degassing are  $\text{H}_2\text{O}$ ,  $\text{CO}_2$ ,  $\text{SO}_2$ ,  $\text{H}_2\text{S}$  and  $\text{HCl}$  (Reeves et al., 2011; Fischer and Chiodini, 2015; Seewald et al., 2015; Wallace et al., 2015; Seewald et al., 2019). With decreasing temperatures, magmatic  $\text{SO}_2$ , which preferentially stays in the aqueous phase as a solution, reacts with water to produce reduced and oxidized sulfuric compounds (Reeves et al., 2011; Seewald et al., 2015). Moreover,  $\text{S}^0$  occurs as a disproportionation product of magmatic  $\text{SO}_2$  (de Ronde et al., 2005; Resing et al., 2007; Butterfield et al., 2011; de Ronde et al., 2011; de Ronde and Stucker, 2015; Seewald et al., 2015).



The more water and dissolved SO<sub>2</sub> is in the system the more the reactions (4.1) and (4.2) are pushed in the direction of the products. Hence, the acidity increases because sulfuric acid dissociates and releases protons (de Ronde et al., 2005; Resing et al., 2007).



These chemical reactions explain the formation of elemental sulfur and the acidic nature of these hydrothermal fluids (e.g., acid-sulfate fluids with pH-values as low as < 1; Seewald et al., 2015). Brothers volcano in the Kermadec arc has sulfur accumulations around vent sites hosted in a resurgent cone (de Ronde et al., 2005; de Ronde et al., 2011; Kleint et al., 2019). These vent fluids have low pH (e.g., around 2 at the Upper Cone site) and moderate pH (e.g., pH 4–5 at the Lower Cone site) (Kleint et al., 2019). In case of the Kemp Caldera, S<sup>0</sup> is forming in hydrothermal environments with fluid pH<sub>25 °C</sub>-values of > 5. This is similar to the Lower Cone site at Brothers, where initial work reported temperatures just below 70 °C and pH-values around 5 for samples collected in 2004 (de Ronde et al., 2011). Samples sampled in 2017 had fluids with pH ranging from 3.8 to 4.8, which were venting at 70–80 °C (Kleint et al., 2019).

Although the occurrence of elemental sulfur at moderate pH in the Kemp Caldera is similar to the Lower Cone site at Brothers, the isotopic composition of the sulfur is not. That is, elemental sulfur accumulations from Lower Cone at Brothers as well as H<sub>2</sub>S from respective fluids have δ<sup>34</sup>S values ranging from –8.3 to –3.9 ‰ for S<sup>0</sup> (de Ronde et al., 2005) and from –8.0 to –4.8 ‰ (de Ronde et al., 2011). These negative δ<sup>34</sup>S values of elemental sulfur and sulfide are expected if resulting from disproportionation of magmatic SO<sub>2</sub> (de Ronde et al., 2005; de Ronde et al., 2011; McDermott et al., 2015). Furthermore, the δ<sup>34</sup>S values of sulfate minerals have to be considered. At the temperatures in the hydrothermal root zones (e.g., > 300 to 350 °C), δ<sup>34</sup>S<sub>SO<sub>4</sub> is 16 to 21 ‰ heavier than δ<sup>34</sup>S<sub>S</sub> (Kusakabe et al., 2000), and thus sulfate minerals forming in systems affected by SO<sub>2</sub> disproportionation should show δ<sup>34</sup>S values considerably lower than seawater (~21 ‰), which they do for the Cone site at Brothers, with δ<sup>34</sup>S values for natroalunite ranging between 14.7 and 17.9 ‰ (de Ronde et al., 2005). At Toxic Castle, however, the δ<sup>34</sup>S<sub>SO<sub>4</sub> value of barite is higher than that of seawater. Moreover, the δ<sup>34</sup>S values of both elemental sulfur and H<sub>2</sub>S of the Kemp Caldera hydrothermal system are positive: S<sup>0</sup> data (*n* = 3) are between 5.2 and 5.8 ‰, while δ<sup>34</sup>S<sub>H<sub>2</sub>S</sub> from the Great Wall fluid is only slightly lower at 4.6 ‰.</sub></sub>

The SO<sub>2</sub> disproportionation reactions are strongly dependent on temperature, pH, redox state and total sulfur content (Kusakabe et al., 2000; Seewald et al., 2015; Peters et al., 2021). At high temperatures (> 300 °C), reaction (4.1) is preferred (producing H<sub>2</sub>S), whereas with further cooling of magmatic fluids, reaction (4.2) and the formation of S<sup>0</sup> becomes more important (Seewald et al., 2015; Seewald et al., 2019; Peters et al., 2021). This is consistent with

observations from submarine hydrothermal vent fields, e.g., at SuSu Knolls (NS1) and DESMOS (D2) in the Eastern Manus Basin and Cone site at Brothers (Kermadec arc), where elemental sulfur is likely a result of  $\text{SO}_2$  disproportionation occurring at temperatures as low as  $83\text{ }^\circ\text{C}$  (Gena et al., 2006; de Ronde et al., 2011; Seewald et al., 2015; Kleint et al., 2019; Peters et al., 2021). Molten sulfur from Niuatahi caldera volcano (NE Lau Basin), Daikoku, Nikko and NW Rota-1 (Mariana arc) is formed at temperatures between  $\sim 180$  and  $200\text{ }^\circ\text{C}$  (Resing et al., 2007; Butterfield et al., 2011; Kim et al., 2011; de Ronde et al., 2015; de Ronde and Stucker, 2015). At all these sites,  $\text{S}^0$  shows negative  $\delta^{34}\text{S}$  values (see Figure 4.11). The only known exception is the Niuatahi volcanic edifice (Niuatahi North) located in the northeast of Niuatahi volcano in the NE Lau Basin. There, a sulfur sample with a positive  $\delta^{34}\text{S}$  value of  $3.1\text{ }‰$  was found at a site of diffuse hydrothermal venting ( $T = 80\text{ }^\circ\text{C}$ ,  $\text{pH}_{25\text{ }^\circ\text{C}} = 2.2$ ) (Peters et al., 2021).

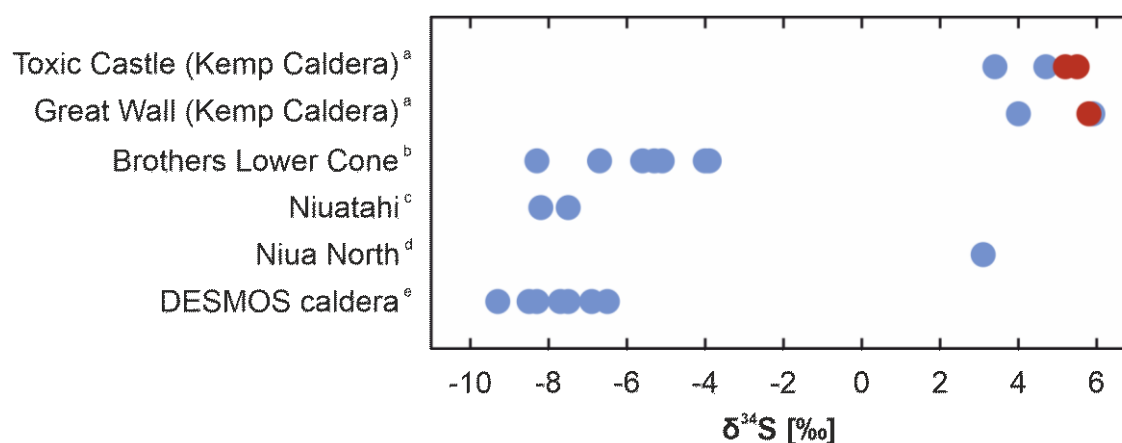


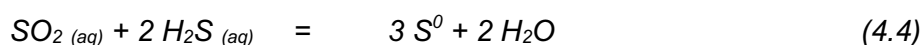
**Figure 4.11.**  $\delta^{34}\text{S}$  ranges for elemental sulfur from comparable submarine hydrothermal sites. <sup>a</sup> taken from Hepburn (2015), <sup>b</sup> taken from de Ronde et al. (2005) and de Ronde et al. (2011), <sup>c</sup> taken from Kim et al. (2011), <sup>d</sup> taken from Peters et al. (2021) and <sup>e</sup> taken from Gena et al. (2006). In red: values we measured (presented in this work).

The Kemp Caldera system is different from other sulfur-forming acid-sulfate vents in that the fluid is high in pH, and the isotopic compositions are uncommonly heavy. The high  $\text{pH}_{25\text{ }^\circ\text{C}}$  measured in Toxic Castle is likely compromised by sampling problems, but the fluids sampled at Great Wall are not affected by fluid sampling artefacts and also show a high pH trend. Subseafloor mixing of seawater can increase the pH of fluids venting in acid-sulfate areas. The Lower Cone fluids at Brothers volcano, for example, have pH-values of 4–5 (de Ronde et al., 2011; Kleint et al., 2019). However, the sulfur deposited around the Lower Cone vent site shows the isotopic signature of  $\text{SO}_2$  disproportionation. Such evidence is lacking at Kemp Caldera. Therefore, disproportionation of  $\text{SO}_2$  is very unlikely the source of sulfur at Toxic Castle and Great Wall because the isotopic composition of  $\text{SO}_2$  or the conditions of disproportionation are highly unusual. These values appear incompatible with  $\text{SO}_2$  disproportionation (McDermott et al., 2015).

At 300 °C, the difference between the  $\delta^{34}\text{S}$  values of  $\text{S}^0$  and  $\text{SO}_4$  ( $\Delta^{34}\text{S}_{\text{S-SO}_4}$ ) should be between 20 and 22.5 ‰ (McDermott et al., 2015). Considering  $\delta^{34}\text{S}$  values of 4 to 10 ‰ for arc lavas (Hannington et al., 2005),  $\text{SO}_2$  with a  $\delta^{34}\text{S}$  value of 5 ‰ would make  $\text{S}^0$  with ca. -6 ‰ and  $\text{SO}_4$  with 15 ‰. These are typical values for native sulfur and sulfate minerals from various sites of acid-sulfate venting (e.g., McDermott et al., 2015). However, the sulfur at Toxic Castle is 5.5 ‰, and the barite is 22.4 ‰ (Table 4.3). These values lie outside of the isotopic range established for acid-sulfate venting. The only way to explain the Toxic Castle data by  $\text{SO}_2$  disproportionation is to assume that the degassing  $\text{SO}_2$  has a  $\delta^{34}\text{S}$  value of ~17 ‰. The  $\text{S}^0$  would then be 5.5 ‰, and the sulfate 26.5 ‰ (the lower  $\delta^{34}\text{S}$  values of the barite could reflect mixing with seawater). However, we consider it is highly unlikely that magmatic  $\text{SO}_2$  could possibly be as heavy as 17 ‰. Hence, we conclude that this process is not responsible for the formation of native sulfur at the Kemp Caldera hydrothermal vent field.

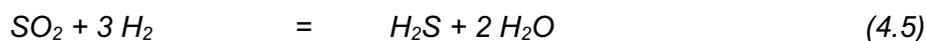
Another possibility for the formation of elemental sulfur here could be the oxidation of  $\text{H}_2\text{S}$ . It has been previously shown that partial oxidation of  $\text{H}_2\text{S}$  by  $\text{O}_2$  is one of the major mechanisms that leads to elemental sulfur formation in (subaerial) hydrothermal systems at a range of pH and low temperatures (Zeng et al., 2007; Markússon and Stefánsson, 2011).  $\text{H}_2\text{S}$  oxidation to  $\text{S}^0$  is associated with very small isotopic fractionation of < 2 ‰ (Ohmoto and Rye, 1979). Hence, the small differences in  $\delta^{34}\text{S}$  between  $\text{H}_2\text{S}$  (at Great Wall) and  $\text{S}^0$  (at Toxic Castle) could point to  $\text{H}_2\text{S}$  oxidation. However, the high temperature and presence of abundant liquid sulfur make it unlikely that  $\text{H}_2\text{S}$  oxidation could be the source of that sulfur. Given the high  $\text{H}_2\text{S}$  content of the hydrothermal fluids at Kemp, dissolved oxygen with its low concentration (< 200  $\mu\text{M}$ ) is the limiting reactant in the system. A very large influx of cold deep-sea water would hence be required to oxidize enough  $\text{H}_2\text{S}$  to account for the massive occurrence of  $\text{S}^0$ . This would result in a drastic decrease in temperature. Such high fluxes of cold oxygenated seawater (which is a highly efficient coolant) are inconsistent with the high temperatures > 200 °C and high heat flux required for the accumulation of liquid sulfur at Kemp Caldera.

A third possibility is that synproportionation of  $\text{SO}_2$  and  $\text{H}_2\text{S}$  to sulfur occurs in the Kemp Caldera magmatic-hydrothermal system. The reaction stoichiometry of the synproportionation reaction (4.4) indicates that, unlike in the disproportionation reaction, protons are not released, which could explain the relatively high pH of the vent fluids:



As a precondition for the reaction, both reactants must be present in sufficiently large amounts, which requires simultaneous release of both sulfur species in the course of magma degassing. Indeed, it is common that both sulfur-bearing phases are released during magma degassing, but the ratio depends on the relative magmatic oxygen fugacity (Wallace et al., 2015). At more

oxidizing conditions and/or higher temperatures, mainly SO<sub>2</sub> is present in relation to H<sub>2</sub>S (Nilsson and Peach, 1993; Aiuppa et al., 2005; Wallace et al., 2015). During magma degassing at high temperatures, the reaction (4.5)



may reach equilibrium (Aiuppa et al., 2005; Butterfield et al., 2011). As the temperature (or the oxygen fugacity) increases, the equilibrium of the reaction shifts toward the higher entropy, i.e., to the left. Decreasing pressure will also favor the formation of SO<sub>2</sub> and H<sub>2</sub> (Gaillard and Scaillet, 2014).

The Kemp Caldera comprises an arc/back-arc hydrothermal system as part of the South Sandwich island arc. Arc lavas have relatively high δ<sup>34</sup>S values (4 to 10 ‰; Hannington et al., 2005) compared to MORB (mean δ<sup>34</sup>S = -0.91±0.5 ‰; Labidi et al., 2012). Due to the relatively high δ<sup>34</sup>S of arc lavas and the small isotopic fractionation factor during synproportionation at high mol fraction of SO<sub>2</sub> and H<sub>2</sub>S, sulfur isotopes of elemental sulfur as well as of hydrogen sulfide give positive values of δ<sup>34</sup>S.

To test the likelihood of different formation mechanisms of elemental sulfur in terms of isotopic composition, a Rayleigh fractionation model was applied (Figure 4.12). The results of these calculation suggest that both disproportionation of SO<sub>2</sub> and oxidation of H<sub>2</sub>S fall short of accounting for the high δ<sup>34</sup>S values obtain for the sulfur sampled at Kemp. Synproportionation of SO<sub>2</sub> and H<sub>2</sub>S, however, may explain the observed isotopic composition of sulfur.

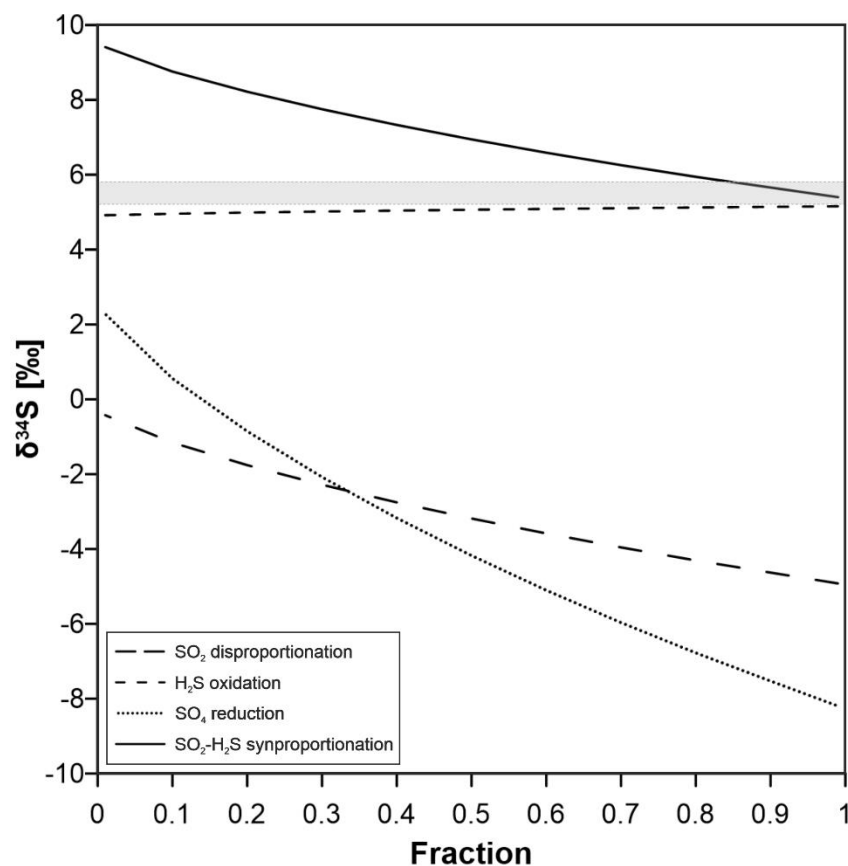


**Figure 4.12.** Range of  $\delta^{34}\text{S}$  values of elemental sulfur at various fractions ( $f = 0.01$  to  $0.99$ ) upon  $\text{SO}_2$  disproportionation,  $\text{H}_2\text{S}$  oxidation and  $\text{SO}_2$ - $\text{H}_2\text{S}$  synproportionation at  $220^\circ\text{C}$ . The gray-shaded area indicates the range of measured  $\delta^{34}\text{S}$  values of  $\text{S}^0$  ( $\delta^{34}\text{S} = 5.2$  to  $5.8$  ‰) at the Kemp Caldera. We assumed a mean isotopic composition of  $7.5$  ‰ for  $\text{SO}_2$  and a  $\delta^{34}\text{S}$  value of  $4.5$  ‰ for  $\text{H}_2\text{S}$ . Disproportionation of  $\text{SO}_2$  is expected to produce sulfur with negative  $\delta^{34}\text{S}$  values, where  $\text{H}_2\text{S}$  oxidation to sulfur has a very small isotope effect (Ohmoto and Rye, 1979) and hence the computed values are close to the  $\delta^{34}\text{S}$  value of the influxing  $\text{H}_2\text{S}$  ( $4.5$  ‰). The only formation process that results in heavy sulfur  $\geq 5.2$  ‰ is the synproportionation of  $\text{SO}_2$  and  $\text{H}_2\text{S}$ . The resulting  $\delta^{34}\text{S}$  values are between  $5.4$  and  $9.4$  ‰. Further details of the calculations are provided in the appendix.

To further examine if the reaction of  $\text{SO}_2$  with  $\text{H}_2\text{S}$  to form elemental sulfur and water is plausible for Kemp Caldera (and perhaps other arc hydrothermal systems), the energetics of this reaction are investigated (Figure 4.13).

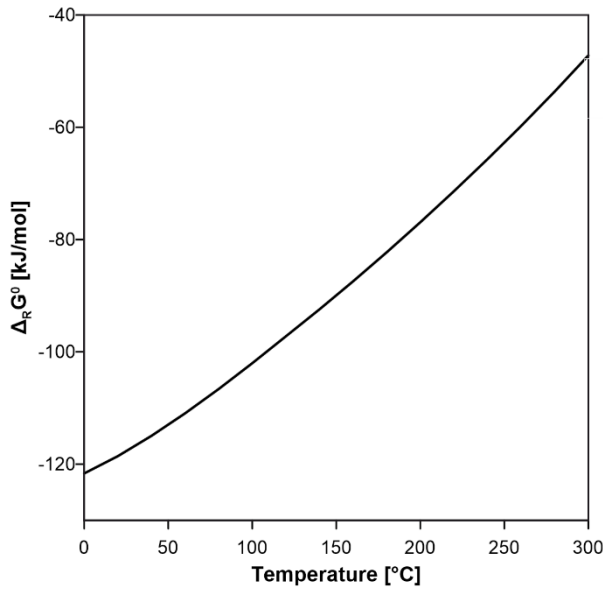


**Figure 4.13.** Temperature dependency of the free standard reaction enthalpy ( $\Delta_R G^0$ ) of the synproportionation reaction (4.4). Calculations were made at isobaric conditions (143 bar) using SUPCRT.

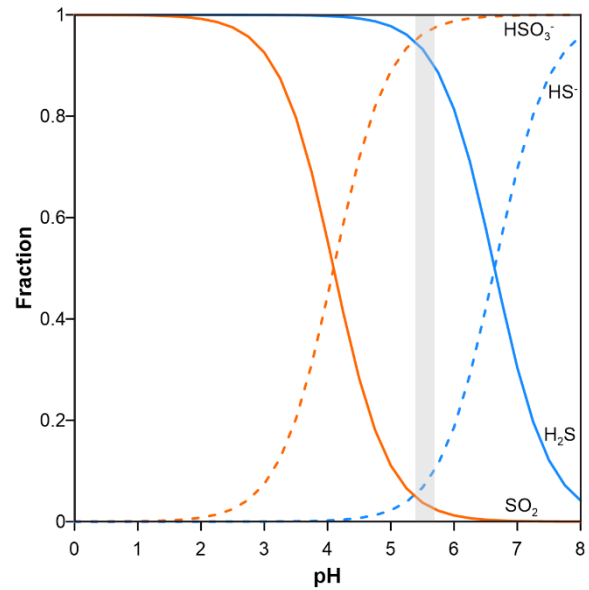
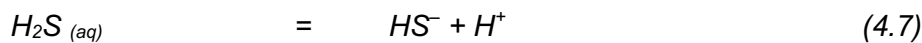
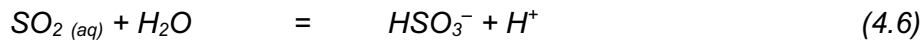


**Figure 4.14.** Influence of pH on the speciation of  $H_2S$  and  $SO_2$  at 220 °C. The shaded bar indicates the pH range of pH-values from Toxic Castle and Great Wall.

The sulfur concentrations and speciation also affect the energetics of this reaction. Hence, the Gibbs energy ( $\Delta_R G$ ) was calculated for a range of conditions. The pH dependency of the sulfite and sulfide speciation was taken into account:



Under the conditions at Great Wall and Toxic Castle ( $pH_{25\text{ °C}} = 5.4\text{--}5.7$ ),  $HSO_3^-_{(aq)}$  is the dominant sulfite species and  $H_2S$  is the dominant sulfide species. With increasing pH, the fraction of  $H_2S$  becomes smaller, while  $SO_2$  and  $H_2S$  are the dominant species at low pH (Figure 4.14).

For the above reactions, measured concentrations of  $H_2S$  dissolved in the fluids were included in the calculations. Sulfur dioxide concentrations could not be determined, so an average value of 15 mM was assumed based on the finding by Butterfield et al. (2011). Values for  $\Delta_R G$  of the synproportionation reaction according to equation (4.4) were then calculated from the standard state thermodynamic data and activities of the involved sulfuric species (Figure 4.15).

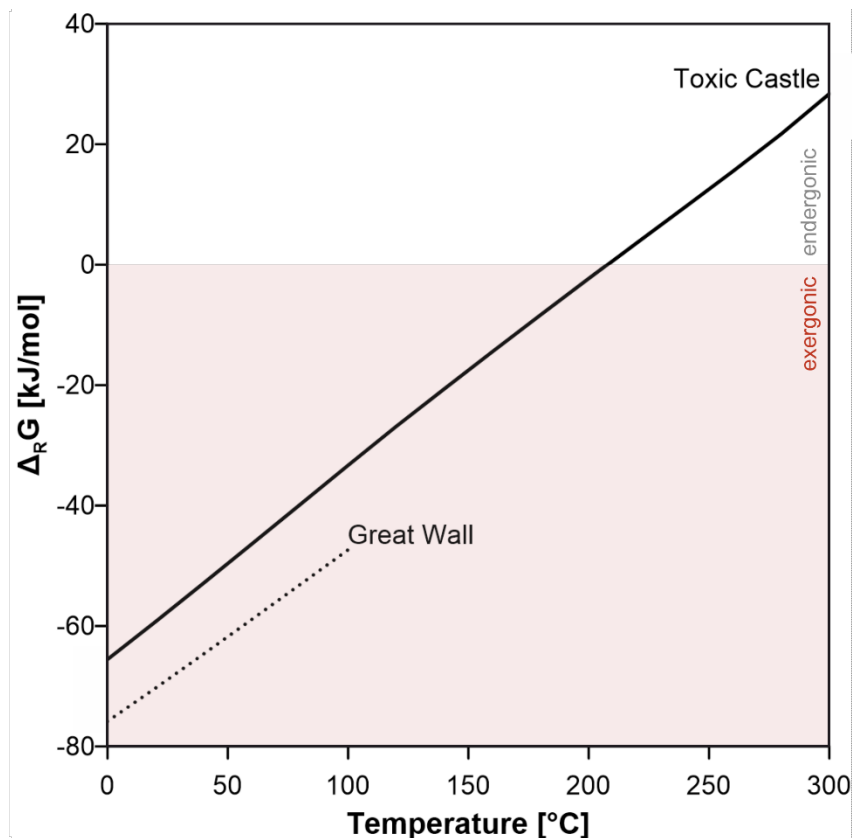


**Figure 4.15.** Free reaction enthalpy of synproportionation as a function of temperature. The reaction is entirely exergonic for Great Wall. At Toxic Castle it is near chemical equilibrium for the maximum temperatures in the range of 207–237 °C.

For temperatures below ~208 °C, synproportionation reactions are exergonic for both locations. At Toxic Castle, however, the reaction is closer to chemical equilibrium in the measured temperature range of 207–237 °C. Unfortunately, only 2 ml of fluid sample could be collected from Toxic Castle, which means that interpretation of the data should be viewed with caution. All element and gas concentrations are assumed to be significantly higher. In that case, the synproportionation reaction at Toxic Castle would also be exergonic for the entire temperature range.

Finally, we tested the feasibility for  $S^0$  formation essentially by synproportionation in a reaction path model (Figure 4.16). Influxing of 2 moles of  $H_2S$  and 1 mole of  $SO_2$  per kg of seawater-derived fluid will generate almost 3 moles of  $S^0$  with an isotopic composition of 5.4 ‰, and the final fluid will have a pH of 2.2. Influxing of a more  $SO_2$ -dominated vapor (0.2 moles  $H_2S$ , 1 mole  $SO_2$ ) will generate < 0.6 moles of  $S^0$  with an isotopic composition of -4.5 ‰ and the fluid will have a final pH of 0.5. If this fluid is allowed to mix with seawater, an additional 0.01 mol of  $S^0$  will form, but it will develop towards isotopically lighter compositions.

It should be noted that this type of computation finds the equilibrium speciation and sulfur abundance in a reaction network of the S-O-H system, in which sulfur is allowed to have four

different redox states (-2, 0, +4, +6). These four species are linked by six redox reactions with H<sub>2</sub> as electron donor and a total of four possible disproportionation and synproportionation reactions. The result of reaction path computation hence clearly suggests that synproportionation of SO<sub>2</sub> and H<sub>2</sub>S is predicted to predominate in systems in which both H<sub>2</sub>S and SO<sub>2</sub> are fluxed in. If the H<sub>2</sub>S influx is low, disproportionation of SO<sub>2</sub> predominates.

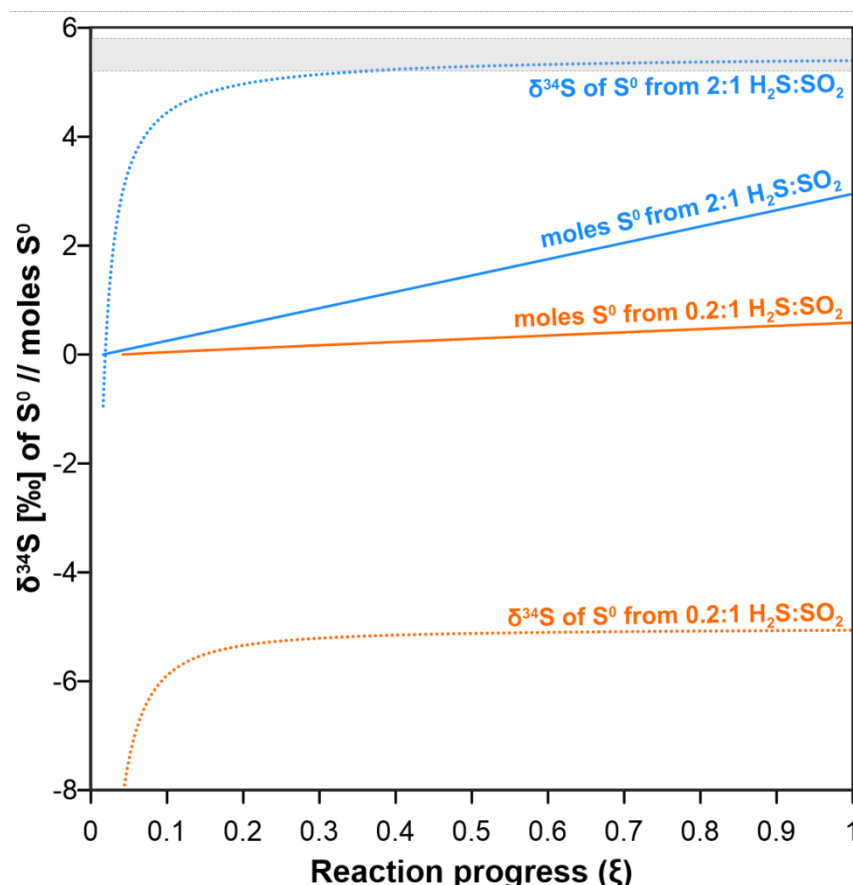


**Figure 4.16.** Reaction path model for H<sub>2</sub>S-dominated (2:1 H<sub>2</sub>S:SO<sub>2</sub> displayed in blue) and SO<sub>2</sub>-dominated (0.2:1 H<sub>2</sub>S:SO<sub>2</sub> displayed in orange) reactions resulting in different molar mass and different isotopic composition of the generated elemental sulfur. The ratio 2:1 H<sub>2</sub>S:SO<sub>2</sub> produces 3 moles of S<sup>0</sup> with  $\delta^{34}\text{S} = 5.4 \text{ ‰}$ , while a ratio of 0.2:1 generates less than 0.6 moles of sulfur with an isotopic value of  $-4.5 \text{ ‰}$ .

Based on these results, the formation of elemental sulfur by direct influx of H<sub>2</sub>S and SO<sub>2</sub> appears the most plausible mechanism for explaining the copious amounts of isotopically heavy sulfur in Kemp Caldera. The mechanism can also explain the “higher-than-common” pH. Most acid-sulfate fluids venting in submarine arc volcano-hosted hot springs are very acidic and have isotopically light sulfur and sulfide. This points to degassing of SO<sub>2</sub>, as previously suggested (e.g., McDermott et al., 2015; Peters et al., 2021). We show that deviations from this common feature do exist and are most plausibly explained by higher relative proportions of influxing H<sub>2</sub>S. A small fraction of this H<sub>2</sub>S may get oxidized to S<sup>0</sup> by

oxygen dissolved in entrained seawater, but the majority of the elemental sulfur is formed by oxidation of H<sub>2</sub>S with sulfite or sulfate (synproportionation).

#### 4.6 Summary and conclusions

Our results provide a first overview of the minerals occurring at the Kemp Caldera hydrothermal vent field. The center of the caldera is dominated by white smoker vent fields commonly seen in other magmatic-hydrothermal systems, yet the mineral assemblage seen at Kemp Caldera are atypical for such an environment. It seems that they are the result of a combination between magmatic- and water-rock-dominated hydrothermal systems. Analyses of minerals and hydrothermal vent fluids show the occurrence of elemental sulfur adjacent to Cu- and Zn-rich sulfides, considering thermodynamic properties. Under favorable conditions (elevated temperatures and high sulfur fugacity) it is possible that elemental sulfur can coexist with sulfide minerals such as bornite, covellite and pyrite. Due to high sulfur fugacities and hydrothermal alteration of (pre-existing) minerals, sulfur is segregated and precipitated in liquid or solid form next to sulfide mineral assemblages or in paragenesis.

Despite the high pH<sub>25 °C</sub>-values of > 5 of the hydrothermal fluids, S<sup>0</sup> is found at the Great Wall and Toxic Castle sites with the former finely crystalline and the latter molten. Disproportionation of SO<sub>2</sub> is accompanied by the generation of protons. Hence, the sulfur formation is usually associated with acidic conditions at arc/back-arc hosted hydrothermal systems. However, in case of the Kemp Caldera hydrothermal system, S<sup>0</sup> is formed by synproportionation. Sulfur dioxide and H<sub>2</sub>S react to form elemental sulfur and water. Low temperatures favor a synproportionation reaction, but it also proceeds at temperatures of 200 °C if sufficient dissolved sulfuric species are contained in the vent fluids. In addition to the uncommonly high pH-values, other evidence for synproportionation comes from the positive δ<sup>34</sup>S isotope values of elemental sulfur and H<sub>2</sub>S. This δ<sup>34</sup>S<sub>S</sub> range from 5.2 to 5.8 ‰ is in contrast to the typically negative δ<sup>34</sup>S values that would indicate disproportionation of magmatic SO<sub>2</sub>. Experiments are needed to gain better insight into the processes of synproportionation of SO<sub>2</sub> and H<sub>2</sub>S. The elemental sulfur produced in such experiments could then be analyzed for its δ<sup>34</sup>S composition to evaluate the possible role of synproportionation in arc/back-arc hydrothermal environments.

## **Acknowledgements**

We thank Captain M. Langhinrichs and his crew from the R/V *Polarstern* for their support and excellent cooperation with the ROV *MARUM QUEST 4000* team on cruise PS119, which was responsible for the sampling. Special thanks go to K. Linse (British Antarctic Survey, UK) and A. Lichtschlag (National Oceanography Centre, UK) for their support and planning during the ROV dives. Our thanks also go to Prof. Dr. Jill McDermott, Lehigh University, USA, who provided us IGT samplers. The PS119 expedition was funded by the German Federal Ministry of Education and Research (grant number 03G0880A) and by the German Research Foundation (Deutsche Forschungsgemeinschaft, DFG) within the Cluster of Excellence (EXC-2077, project number 390741603 “The Ocean Floor – Earth’s Uncharted Interface”) at MARUM – Center for Marine and Environmental Sciences, University of Bremen.

## 5 MANUSCRIPT III

### EXPERIMENTAL STUDY OF SULFUR ISOTOPIC COMPOSITION OF WHITE SMOKER PRECIPITATES IN THE KEMP CALDERA (SCOTIA SEA)

Victoria Kürzinger<sup>1,2</sup>, Christian T. Hansen<sup>1,2</sup>, Harald Strauss<sup>3</sup>, Shi-Jun Wu<sup>4</sup>, Wolfgang Bach<sup>1,2</sup>

<sup>1</sup> MARUM Center for Marine Environmental Sciences, University of Bremen, Leobener Straße 8, 28359 Bremen, Germany

<sup>2</sup> Faculty of Geoscience, University of Bremen, Klagenfurter Straße 2-4, 28359 Bremen, Germany

<sup>3</sup> Institut für Geologie und Paläontologie, WWU Münster, Corrensstraße 24, 48149 Münster, Germany

<sup>4</sup> State Key Laboratory of Fluid Power and Mechatronic Systems, Zhejiang University, Hangzhou 310027, China

#### In preparation for submission

---

#### Abstract

Elemental sulfur ( $S^0$ ) is known to be formed by disproportionation of magmatic  $SO_2$ . Due to isotopic fractionation processes at temperatures above 200 °C,  $S^0$  shows an isotopic composition considerably lower than the influxing  $SO_2$ , which results in  $\delta^{34}S_S$  values typically  $< 0$  ‰. The peculiarity of the occurrence of relatively heavy sulfur in the Kemp Caldera hydrothermal system ( $\delta^{34}S_S > 5$  ‰) or Niua North ( $\delta^{34}S_S = 3.1$  ‰) led to the assumption that disproportionation is not the only sulfur forming process in submarine hydrothermal systems. We assume that sulfur formation in the Kemp Caldera results from synproportionation of  $SO_2$  and  $H_2S$ . Thermodynamically, this formation mechanism is conceivable, but it has not yet been confirmed that this process actually occurs in submarine hydrothermal systems. Experiments were conducted at *in-situ* conditions mimicking the formation of  $S^0$  in a hydrothermal environment. Isotopic fractionation between produced fractions of  $SO_4^{2-}$ ,  $SO_2$ ,  $H_2S$  and  $S^0$  were determined to assess the involvement of potential sulfur forming processes, including  $SO_2$  disproportionation,  $H_2S$  oxidation and  $SO_2$ - $H_2S$  synproportionation. In conjunction with the experiments, a Rayleigh fractionation model was applied to predict the isotopy of sulfur species expected for the different formation pathways and thus enable a comparison with measured experimental values. Only synproportionation can explain the experimentally generated sulfur isotopic signatures and therefore it is likely responsible for the isotopically heavy sulfur occurring in arc/back-arc hydrothermal environments.

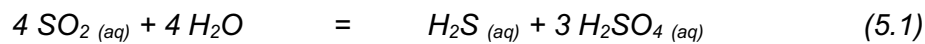
**Keywords:** Elemental sulfur; Kemp Caldera; positive  $\delta^{34}S$  values; synproportionation; experimental geochemistry

---

## 5.1 Introduction

In general, hydrothermal systems in arc/back-arc settings are enriched in volatiles like H<sub>2</sub>O, CO<sub>2</sub>, SO<sub>2</sub> and H<sub>2</sub>S as a result of magma degassing. Hydrogen sulfide is not necessarily a direct product of magma degassing, but can also form through reduction of seawater sulfate or sulfur leaching from the host volcanic rock (Shanks et al., 1981).

It is established that SO<sub>2</sub> is a major gaseous species in arc magmas (e.g., Fischer et al., 1998). Upon cooling and mixing with aqueous solutions in magmatic-hydrothermal systems, it is expected to disproportionate to sulfuric acid and both H<sub>2</sub>S and elemental sulfur (see eq. 5.1 and 5.2; Gamo et al., 1997; Kusakabe et al., 2000; Gena et al., 2006; Butterfield et al., 2011; de Ronde et al., 2011; Seewald et al., 2019):



Sulfate minerals in submarine magmatic-hydrothermal systems formed through disproportionation reactions are characterized by elevated  $\delta^{34}\text{S}$  values (between ca. 17 and 25 ‰; de Ronde et al., 2005; McDermott et al., 2015; Peters et al., 2021) relative to the influxing magmatic SO<sub>2</sub> (4 to 10 ‰; Hannington et al., 2005). Elemental sulfur produced alongside sulfate can have very low  $\delta^{34}\text{S}$  values typically < 0 ‰ like at the DESMOS caldera ( $\delta^{34}\text{S}_\text{S} = -9.3$  ‰; Gena et al., 2006) or at the Cone sites of Brothers volcano ( $\delta^{34}\text{S}_\text{S} = -8.0$  ‰; de Ronde et al., 2011).

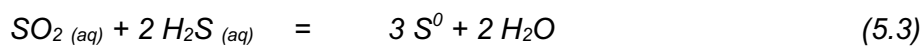
Although sulfides and elemental sulfur have  $\delta^{34}\text{S}$  values < 0 ‰, positive values for S<sup>0</sup> have been documented in Niua, a volcano located in the northernmost Tonga arc, and the Kemp Caldera in the Scotia Sea. The native sulfur at Niua North exhibits a  $\delta^{34}\text{S}$  value of 3.1 ‰, while S<sup>0</sup> at the Great Wall and Toxic Castle white smoker vent fields have even higher  $\delta^{34}\text{S}$  values ranging from 5.2 to 5.8 ‰ (Figure 1; Kürzinger et al., 2022).

Likewise, dissolved sulfide and sulfide minerals in arc-hosted hydrothermal vent fluids typically show negative  $\delta^{34}\text{S}$  values ( $\delta^{34}\text{S} = -9.9$  to  $-0.4$  ‰; de Ronde et al., 2005; Gena et al., 2006; de Ronde et al., 2011), indicating SO<sub>2</sub> disproportionation (cf. de Ronde et al., 2005; de Ronde et al., 2011; McDermott et al., 2015).

Peters et al. (2021) explained the large range of sulfur isotopic composition of sulfate, sulfide and native sulfur by variable SO<sub>2</sub> flux, disproportionation conditions, and host rock compositions. Their SO<sub>2</sub> disproportionation model for S<sup>0</sup>, however, cannot fully explain the  $\delta^{34}\text{S}$  value (3.1 ‰) of elemental sulfur at Niua North, unless the ingassing of a, unusually <sup>34</sup>S-enriched SO<sub>2</sub> is assumed (Peters et al., 2021).

Even higher  $\delta^{34}\text{S}$  values for elemental sulfur were recently reported from Kemp Caldera at the South Sandwich island arc in the Scotia Sea (Kürzinger et al., 2022). The most hydrothermally active area of the Kemp Caldera is located in the center at the eastern flank of a resurgent cone represented by the white smoker vent fields Great Wall and Toxic Castle (Figure 5.1). Fluid venting at low to intermediate temperatures (60 to  $\sim 220$  °C) is associated with precipitation of elemental sulfur (Kürzinger et al., 2022). The 60 °C warm fluids at Great Wall have comparably high pH ( $\text{pH}_{25\text{ }^\circ\text{C}} = 5.4$ ), similar to the Toxic Castle fluid, but the sample quality of the latter was compromised by sampler clogging with liquid sulfur. This molten  $\text{S}^0$  from Toxic Castle shows  $\delta^{34}\text{S}$  values between 5.2 and 5.5 ‰. An even higher value of 5.8 ‰ was measured at Great Wall from a fine-crystalline sulfur sample taken from the wall-like structure. These high  $\delta^{34}\text{S}$  values suggest that disproportionation of magmatic  $\text{SO}_2$  is unlikely the source of elemental sulfur at these sites. Oxidation of  $\text{H}_2\text{S}$ , proposed as a mechanism to explain  $^{34}\text{S}$ -enriched elemental sulfur in terrestrial geothermal sites (Kleine et al., 2021) is implausible for submarine vent sites (Kürzinger et al., 2022).

Kürzinger et al. (2022) suggested synproportionation of  $\text{SO}_2$  and  $\text{H}_2\text{S}$  to elemental sulfur and water as an alternative to explain the observed high  $\delta^{34}\text{S}$  values of the  $\text{S}^0$ :



They showed that this reaction may be exergonic in submarine magmatic-hydrothermal systems that have high concentrations of  $\text{SO}_2$  and  $\text{H}_2\text{S}$  and used a Rayleigh fractionation model to demonstrate that the isotopic composition of the native sulfur measured is consistent with the synproportionation model (Kürzinger et al., 2022).

To test the idea that elemental sulfur in submarine magmatic-hydrothermal systems may form by synproportionation, we conducted autoclave experiments in which we reacted  $\text{SO}_2$  and  $\text{H}_2\text{S}$  under elevated p-T conditions. We measured sulfur concentrations and  $\delta^{34}\text{S}$  values of reactants and reaction products to discern plausible reaction pathways with respect to the fate of  $\text{SO}_2$  (disproportionation versus synproportionation).

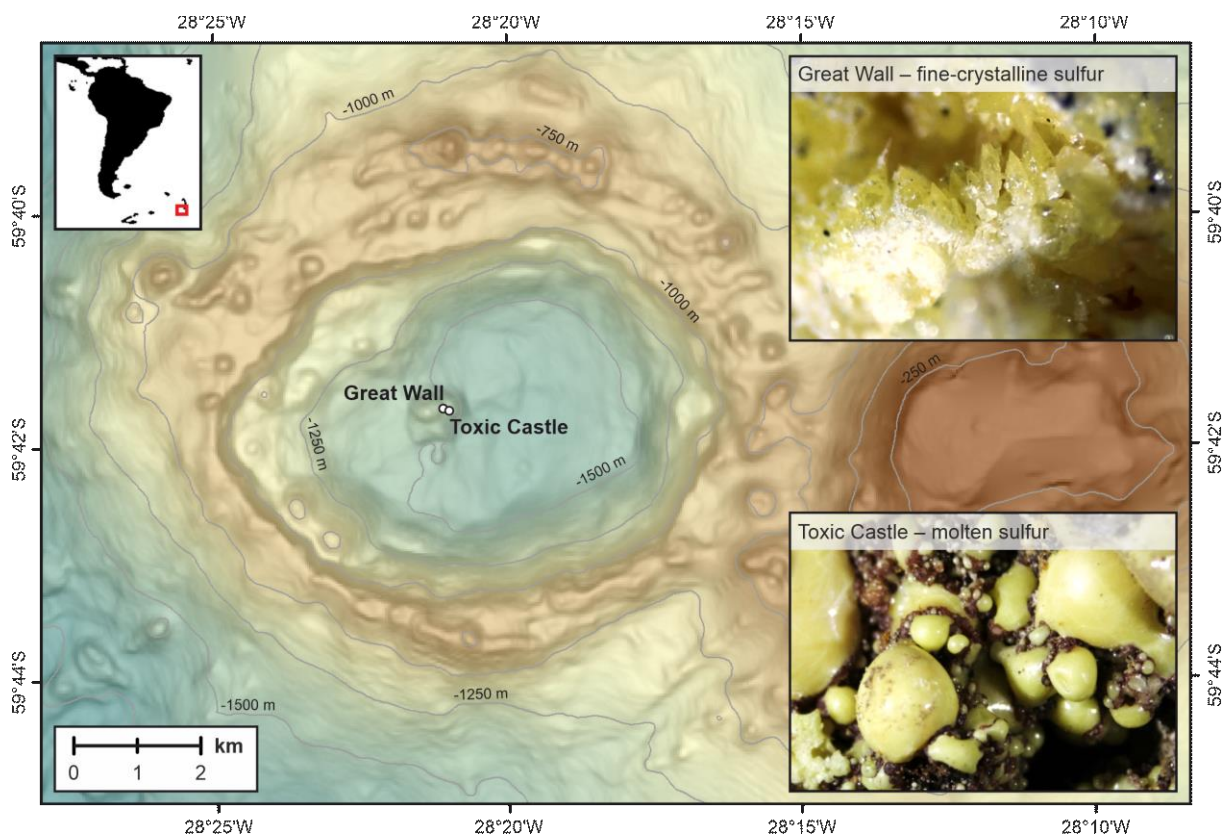


**Figure 5.1.** Bathymetric map of the submarine Kemp Caldera, which is located at the southernmost tip of the intra-oceanic South Sandwich arc. Elemental sulfur was sampled at the active white smoker vent fields Great Wall and Toxic Castle in the caldera center during the R/V *Polarstern* PS119 expedition in 2019.

## 5.2 Methods

### 5.2.1 Experimental setup: Dickson-type reactor (titanium reaction cell)

Experiments were conducted using a modified Dickson-type experimental setup that allows simulations of *in-situ* hydrothermal environment conditions (Dickson et al., 1963; Seyfried et al., 1987). Reactants (fluids and solids) reside within a collapsible container, which is sealed and mounted into a stainless-steel pressure vessel filled with water (see Figure 5.2). Pressure of the water reservoir and the temperature of the vessel can be controlled independently (up to 400 °C and 56.5 MPa). As the pressure is isostatically transferred to the collapsible cell, fluid sampling is enabled through a titanium access tube and an attached custom fitted valve. Due to the reactivity of gold in H<sub>2</sub>S-rich hydrothermal solutions we used a collapsible titanium foil cell ( $V_{\text{tot}} \sim 60$  mL) instead of the more widely used cells made of gold (Hayashi and Ohmoto, 1991; Wu et al., 2016). The Ti-cell was thoroughly cleaned with hydrochloric acid and heated to 400 °C in air to create a surface layer of titanium oxide that is sufficiently inert under the targeted experimental conditions.

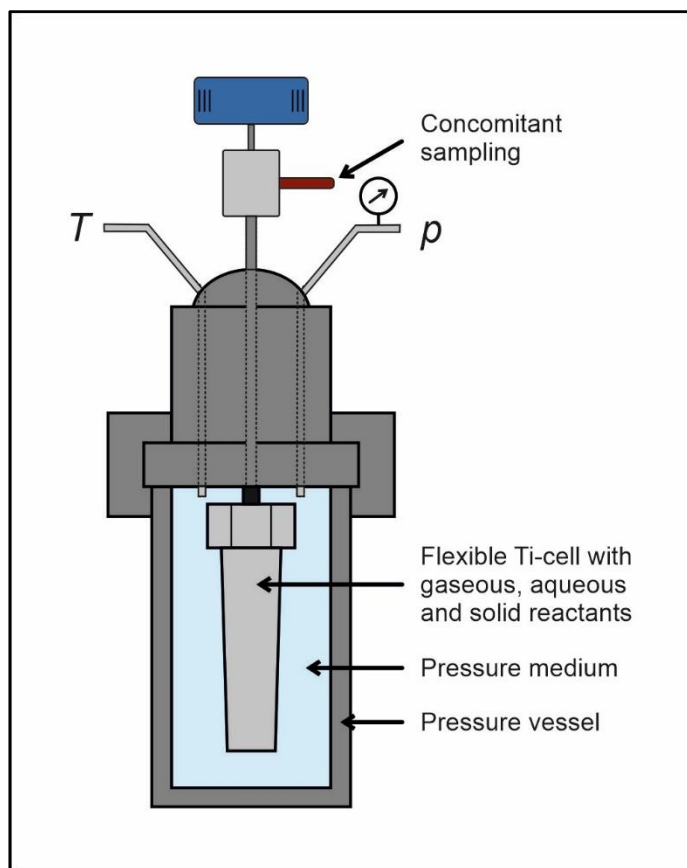


**Figure 5.2.** Scheme of the used hydrothermal reactor. The complete experimental setup is made up of the modules for pressure and temperature control together with the hydrothermal Dickson-type reactor containing a titanium reaction cell.

### 5.2.2 Sampling procedure and handling

The experiments were designed to investigate the isotopic fractionation of  $\text{SO}_2$ ,  $\text{H}_2\text{S}$  and  $\text{S}^0$ , respectively, during the synproportionation reaction. The reactants sodium sulfide hydrate ( $\text{Na}_2\text{S} \cdot 3 \text{H}_2\text{O}$ ), sodium sulfite ( $\text{Na}_2\text{SO}_3$ ) and elemental sulfur ( $\text{S}^0$ ) were weighed and transferred into the titanium cell prefilled with  $\sim 60$  mL of  $\text{O}_2$ -free ultrapure water (purged with  $\text{N}_2$ ). The weight of reactants was chosen to target a sulfide molarity ratio of 20 mmol/L vs. 10 mmol/L sulfite on  $\sim 60$  mL of fluid (Table 5.1). A vanishingly small amount of elemental sulfur was added as a crystallization nucleus.

**Table 5.1**

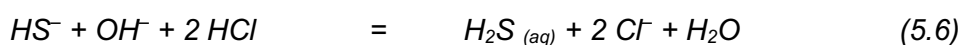
Preparation of experiments: amount of  $\text{O}_2$ -free ultrapure water, amount of HCl as well as the weighted portions of sodium sulfide hydrate ( $\text{Na}_2\text{S} \cdot \text{H}_2\text{O}$ ), sodium sulfite ( $\text{Na}_2\text{SO}_3$ ) and elemental sulfur ( $\text{S}^0$ ).

		Experiment #1	Experiment #2	Experiment #3
Water	[mL]	60.9	58.8	59.7
25% HCl	[ $\mu\text{L}$ ]	245.0	780.0	780.0
$\text{Na}_2\text{S} \cdot 3 \text{H}_2\text{O}$	[mg]	159.1	159.0	158.9
$\text{Na}_2\text{SO}_3$	[mg]	76.3	76.0	76.0
$\text{S}^0$	[mg]	2.4	0.9	0.9

Upon dissolution under hydrothermal conditions, these reactants provide the naturally occurring sulfide and sulfite for the experiments:



The OH<sup>-</sup> released by reaction (5.4) and (5.5) makes the starting solution alkaline, which prevents the degassing loss of sulfide and sulfite. However, the hydrothermal fluids are acidic (cf. reactions 5.1 and 5.2) and the fully protonated species H<sub>2</sub>S and SO<sub>2</sub> dominate. The pH was adjusted by adding a small aliquot of 25 % HCl right before the Ti-foil cell was sealed within the pressure vessel.



The setup was then heated to approximately 220 °C, while the pressure was maintained between 20 to 30 MPa. For the characterization of sulfur, sulfide and sulfate, 10 mL of sample were taken with a gastight syringe at experimental conditions after a minimum of 24 hrs.

The sample was transferred into a vacuumed vial with a septum and 1 mL of 85 % H<sub>3</sub>PO<sub>4</sub> was added for a quantitative extraction of the dissolved sulfide by means of N<sub>2</sub> purging (20 min) through a gas wash bottle prefilled with 20 mL of 5 % AgNO<sub>3</sub> solution. Sulfide precipitated as Ag<sub>2</sub>S flakes and was collected on a pre-weighed polycarbonate filter enabling a subsequent gravimetric quantification. Next, 5 mL of this N<sub>2</sub>-purged solution were transferred to a second vacuumed vial and 300 µL of a 1M BaCl<sub>2</sub> solution were added to precipitate any potentially present sulfate. For the last experiment (experiment #3), we did not split the purged solution and added 600 µL of a 1M BaCl<sub>2</sub> solution to the 10 mL sample in order to maximize the amount of sulfate for the isotopic characterization.

### 5.2.3 Sulfur isotopes

For sulfur isotope measurements, ca. 50 µg of elemental sulfur or 300 to 400 µg of sulfide are mixed with 400 to 800 µg of V<sub>2</sub>O<sub>5</sub> and homogenized within a tin cup. Isotope measurements were carried out via elemental analyzer isotope ratio mass spectrometry (EA-IRMS) using a Flash EA IsoLink attached to a Thermo Fisher Scientific Delta V Advantage mass spectrometer. The reproducibility determined by replicate measurements was usually better than 0.3 ‰ (1σ). Analytical performance was controlled with IAEA-S1, -S2, -S3 and NBS 127 as international reference materials and with laboratory internal standards.

Using the initial isotopic composition of the reactants, we constructed a Rayleigh fractionation model (cf. McDermott et al., 2015; Kleine et al., 2021; Kürzinger et al., 2022). With this fractionation model we were able to predict sulfur isotopic compositions for all potential formation pathways classify the measured values accordingly. Further details of the calculations are given in the appendix.

Gibbs energies of reaction under experimental conditions were calculated for the sulfur formation reactions (syn- and disproportionation) as well as for the dissociation reactions of all involved sulfur species using the SUPCRT92 software package (Johnson et al., 1992).

## 5.3 Results

### 5.3.1 Experimental results

Photographs of the experimental results as well as representative SEM images of elemental sulfur formed during the experiments are shown in Figure 5.3 and 5.4.

For each experimental run, the individual steps were carried out as described above. During the first experiment (#1), precipitation of sulfur was not observed, although H<sub>2</sub>S clearly had formed (strong characteristic smell) and the solution acquired a yellowish color. Sulfur precipitation only occurred following acidification with phosphoric acid for H<sub>2</sub>S expulsion. Apparently, the synproportionation reaction does not proceed under alkaline conditions or kinetics are too sluggish for significant reaction turnover (previous pH ~ 7.8, see Table 5.2).

Accordingly, the follow-up experiments (#2 and #3) were run at conditions energetically more favorable for the synproportionation reaction we suspect to take place at Toxic Castle in the Kemp Caldera hydrothermal system. As described in Kürzinger et al. (2022), the pH at Toxic Castle is likely lower than measured in 2019 (pH<sub>25 °C</sub> = 5.7) due to seawater entrainment during sampling. Following a conservative estimate, we hence set the target condition at a pH<sub>25 °C</sub> < 2 to ensure the necessary thermodynamic drive for the reaction. As a result, small sulfur flakes were even visible in the reaction concomitant fluid sample extracted at 220 °C (“hot sample”). Abundant fine-crystalline sulfur could then be recovered from the open titanium cell after terminating the experiment (Figure 5.3). Sulfate, only present in dissolved form, could be precipitated as BaSO<sub>4</sub> for a subsequent quantification. In addition, very small amounts of H<sub>2</sub> could be quantified (5–10 µmol/L).

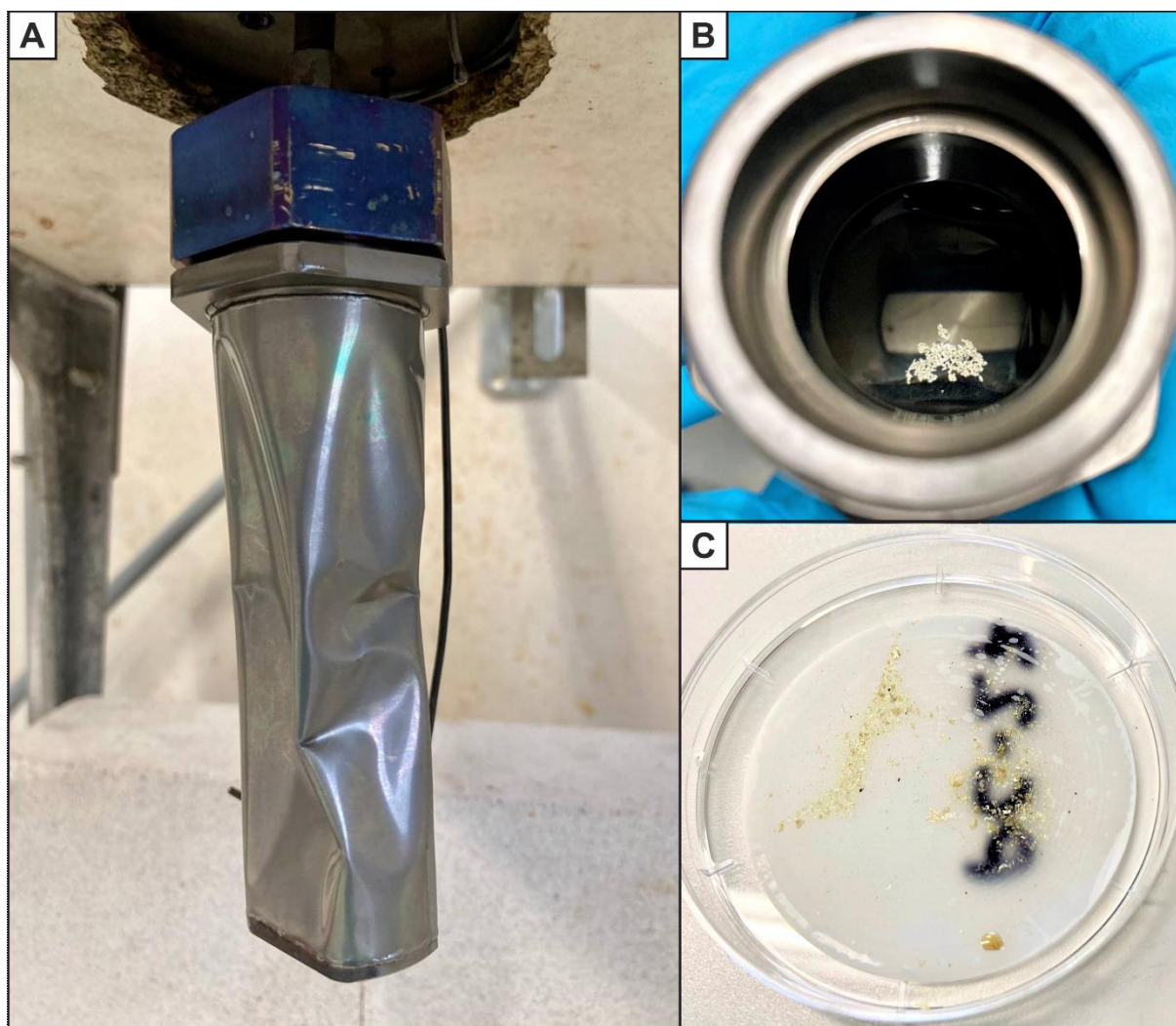


**Figure 5.3.** Images of the titanium reaction cell and the elemental sulfur formed during the last experiment. A) Collapsed titanium cell after finishing the experiment, B) View into the opened cell: Elemental sulfur floats on the solution, more sulfur formed during the experimental run was found on the Ti-cell wall and bottom, and C) Fine-crystalline elemental sulfur from the Ti-cell pictured in (B) on a polycarbonate filter.

The sulfur recovered from experiments #2 and #3 had a very similar appearance compared to the sulfur samples from the Kemp Caldera (Figure 5.4). With the “hot sample” we also sampled some very fine-grained elemental sulfur (fitting through the 2  $\mu\text{m}$  in-line Ti-filter) into the syringe or some precipitated there from the solution upon rapid cooling and depressurization. This sulfur resembles the liquid  $\text{S}^0$  at Toxic Castle (Figure 5.4A). On the other hand, the sulfur from the cooled reaction cell is fine-crystalline as it is at Great Wall (Figure 5.4B).

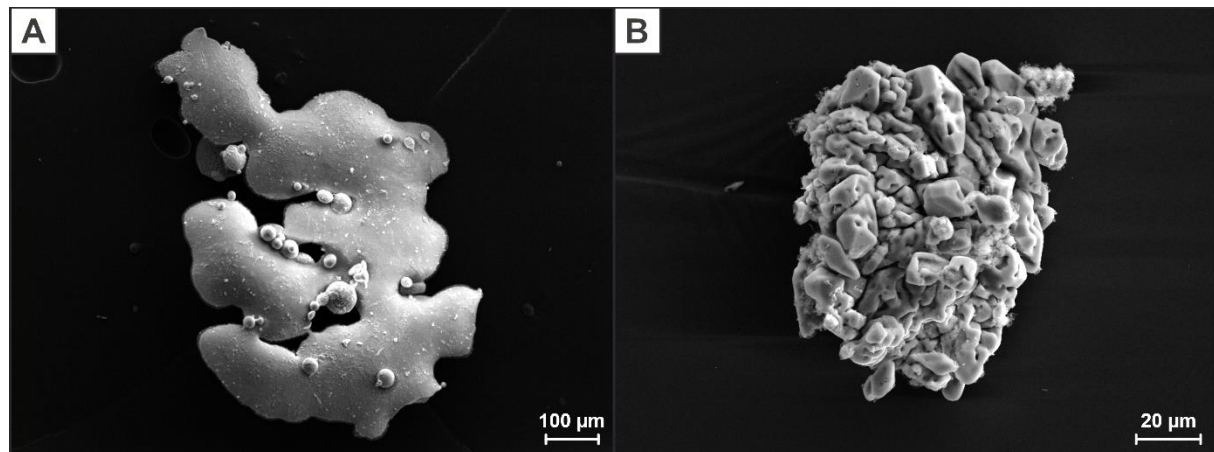


**Figure 5.4.** SEM images of elemental sulfur formed during experiment #2. A) Sulfur particle from the subsample taken at 220 °C. The appearance is similar to the molten sulfur at Toxic Castle (Kemp Caldera), and B) Fine-crystalline sulfur recovered from the Ti reaction cell after finishing the experiment (cf. Figures 5.3B and C). These particles resemble sulfur from the Great Wall site in Kemp Caldera (cf. Figure 5.1).

### 5.3.2 Sulfur isotopes

Isotopic compositions for the reactants  $\text{Na}_2\text{S} \cdot 3 \text{H}_2\text{O}$ ,  $\text{Na}_2\text{SO}_3$  and  $\text{S}^0$  (used as crystallization nucleus) were determined along with that of the  $\text{S}^0$ ,  $\text{H}_2\text{S}$  and  $\text{SO}_4$  fractions formed during the experiments (Table 5.2). Isotopic compositions for experimentally formed  $\text{H}_2\text{S}$  were determined from precipitated  $\text{Ag}_2\text{S}$ .

**Table 5.2**

Sulfur isotope data for sodium sulfide hydrate, sodium sulfite, elemental sulfur and the experimentally formed products.

Experiment	pH <sub>25°C</sub>	$\delta^{34}\text{S}$ of (precipitated) sulfur species				
		$\delta^{34}\text{S}_{\text{Sulfide}}$ [‰]	$\delta^{34}\text{S}_{\text{Sulfite}}$ [‰]	$\delta^{34}\text{S}_{\text{S}}$ [‰]	$\delta^{34}\text{S}_{\text{H}_2\text{S}}$ [‰]	$\delta^{34}\text{S}_{\text{SO}_4}$ [‰]
Reactants	--	6.7	-2.8	0.7	--	--
Products						
Exp. #1	7.8	--	--	-10.3	-4.1	nd
Exp. #2	1.2	--	--	<u>-0.3</u>	0.8	nd
Exp. #3	1.1	--	--	<u>0.4</u>	1.5	23.6

(--) means no measurement because material is not available, nd: not determined due to insufficient material. The underlined values mark the values of the recovered fine-crystalline sulfur formed during the experiment.

In experiment #1, elemental sulfur was precipitated during sample processing and is distinct from the  $\text{S}^0$  produced in experiments #2 and #3. Hydrogen sulfide and sulfur isotopic composition were similar in both low-pH experiments and  $\delta^{34}\text{S}$  values display the small offset expected from the minor equilibrium fractionation between native sulfur and  $\text{H}_2\text{S}$  (Ohmoto and Rye, 1979). We suggest that experiments #2 and #3 represent equilibrium partitioning between sulfur and sulfide under *in-situ* conditions.

### 5.3.3 Proportions of substance of experimentally produced sulfur compounds

Total amounts and derived proportions of the different sulfur compounds retrieved from the experiments indicate which reactions must have dominated the system. The amount of sulfate (as BaSO<sub>4</sub>) and sulfide (as Ag<sub>2</sub>S) obtained from the subsamples (5 or 10 mL) and the elemental sulfur retrieved from the much larger residual volume left in the Ti-cell, i.e. 45 mL or 35 mL were both extrapolated to match the initial 60 mL (see Table 5.3).

**Table 5.3**

Calculated molar mass of the sulfur species retrieved from the experiments. The weights of the samples derived from the 5 and 10 mL subsample (values written in brackets) and sulfur from the residual solution (45 mL for Exp. #2 and 35 mL for Exp. #3) were extrapolated to the initial ~60 mL in the Ti-cell at the beginning of the experiment.

Sulfur species	<i>M</i> [g/mol]	Weight [mg]				<i>n</i> [mol]	
		Exp. #2		Exp. #3		Exp. #2	Exp. #3
Sulfur (S <sup>0</sup> )	32.07	(12.8)	17.1	(8.7)	14.9	5.33 × 10 <sup>-4</sup>	4.65 × 10 <sup>-4</sup>
Sulfate (as BaSO <sub>4</sub> )	233.38	(8.0)	96.0	(4.3)	25.8	4.11 × 10 <sup>-4</sup>	1.11 × 10 <sup>-4</sup>
Sulfide (as Ag <sub>2</sub> S)	247.80	(3.7)	22.2	(1.6)	9.6	8.96 × 10 <sup>-5</sup>	3.87 × 10 <sup>-5</sup>

As seen in the results of the mass balance calculation, some sulfur is missing. It is likely that additional sulfur, which has formed a fine coating on the inside of the cell, could not be retrieved. An indication of this is that black Ti<sub>2</sub>S<sub>3</sub> has been formed as thin coating of the cell after the experiment when the Ti-cell was annealed at 600 °C. Apparently, there must have been remained S<sup>0</sup> in the cell to explain that observation.

## 5.4 Discussion

Magmatic sulfides in lavas at MORs show average δ<sup>34</sup>S values of -0.9 ‰, while in arc/back-arc environments the δ<sup>34</sup>S values range from 4 to 10 ‰, and sulfur occurs as SO<sub>2</sub> which is poised to degas from crystallizing magma (Hannington et al., 2005; Wallace, 2005; Labidi et al., 2012). Disproportionation of this magmatic SO<sub>2</sub> in arc/back-arc magmatic-hydrothermal systems forms acid-sulfate fluids with pH-values < 3 (Kim et al., 2009; de Ronde et al., 2011; Seewald et al., 2019). Rooted in a combination of the kinetic δ<sup>34</sup>S isotope effect and a temperature-dependent equilibrium isotope fractionation attributed to the disproportionation of SO<sub>2</sub>, SO<sub>4</sub> is enriched in <sup>34</sup>S and H<sub>2</sub>S and/or S<sup>0</sup> are <sup>34</sup>S-depleted compared to the initial magmatic SO<sub>2</sub> composition (Kusakabe et al., 2000; McDermott et al., 2015). This implies that the δ<sup>34</sup>S values of elemental sulfur are typically < 0 ‰ and those of the associated sulfate is commonly < 21 ‰. The isotope fractionation between native sulfur and H<sub>2</sub>S is very minor (Ohmoto and Rye, 1979), hence sulfides in arc/back-arc vent settings are usually also characterized by δ<sup>34</sup>S values < 0 ‰. But elemental sulfur typically has even lower δ<sup>34</sup>S values than sulfide because it tends to form at lower temperatures.

Although sulfur and sulfide typically have negative values of  $\delta^{34}\text{S}$ , positive values for  $\text{H}_2\text{S}$  and even  $\text{S}^0$  have also been documented in various hydrothermal systems. For instance, hydrothermal fluids at Niuatahi volcano (NE Lau Basin) display positive  $\delta^{34}\text{S}_{\text{H}_2\text{S}}$  values ranging from 0.2 to 4.5 ‰ (Peters et al., 2021). Other examples included the Macauley and Brothers hydrothermal system, both hosted in caldera volcanoes in the Kermadec arc. The Macauley white smoker vent field is close to the summit of a dacitic cone near the SE caldera wall. Here,  $\text{S}^0$  with a  $\delta^{34}\text{S}$  value of  $-3.4$  ‰ precipitates from highly acidic fluids with  $\delta^{34}\text{S}_{\text{H}_2\text{S}}$  values between 1.6 and 2.9 ‰ (Kleint et al., 2019; Peters et al., 2021). Brothers volcano hosts several, chemically distinct active hydrothermal sites (e.g., de Ronde et al., 2005; de Ronde et al., 2011). Whereas the NW Caldera and Upper Caldera vent fields are dominated by black smoker-type fluids and Cu-Fe-rich sulfide chimneys, the Upper and Lower Cone sites are characterized by white smoker venting and the occurrence of native sulfur. Fluids of Brothers Upper Caldera show  $\delta^{34}\text{S}$  values for dissolved sulfide between 3.0 and 4.6 ‰ (Kleint et al., 2019; Peters et al., 2021), while the Cone vent fluids are negative ( $\delta^{34}\text{S} = -8.0$  to  $-4.8$  ‰; de Ronde et al., 2011). Niua, a volcano located in the northernmost Tonga arc, hosts two active vent sites ( $\delta^{34}\text{S}_{\text{H}_2\text{S}}$  between 2.6 and 4.5 ‰), but positive elemental sulfur was only found at Niua North, exhibiting a  $\delta^{34}\text{S}$  value of 3.1 ‰ (Peters et al., 2021).

Even higher  $\delta^{34}\text{S}$  values in the range from 5 to 6 ‰ for elemental sulfur from active vents in the Kemp Caldera, South Sandwich arc, were reported by Kürzinger et al. (2022). They proposed that these values are incompatible with  $\text{SO}_2$  disproportionation and instead suggested that the sulfur is formed by synproportionation. The authors presented thermodynamic model calculations to support the feasibility of this additional pathway of  $\text{S}^0$  formation in magmatic-hydrothermal systems that are affected by the simultaneous degassing of both  $\text{SO}_2$  and  $\text{H}_2\text{S}$ . The very large range in the isotopic composition of sulfur and sulfide in arc/back-arc hydrothermal systems could be an indication of multiple pathways of sulfur formation mechanisms due to essential differences in redox, which allows for variable proportions of  $\text{SO}_2$  and  $\text{H}_2\text{S}$  to be added to the hydrothermal system (cf. Kusakabe et al., 2000).

#### 5.4.1 Experimental evidence for sulfur formation from $\text{SO}_2$ – $\text{H}_2\text{S}$ synproportionation

##### *Mass balance*

Our experimental results presented in this study indicate that the largest fractionation of the sulfur formed during the experiments could not have been due to  $\text{SO}_2$  disproportionation. This can easily be seen by the data presented in Table 5.3 (result section). First, less than 0.1 mmol of the original 12 mmol sulfide were left over. This shows that sulfide was not produced during  $\text{SO}_2$  disproportionation (eq. 5.1), but instead it was consumed (such as in reaction 5.3). Second, disproportionation should produce twice as much sulfate than sulfur (see eq. 5.2). But

in the reaction product the amount of sulfur is greater than the amount of sulfate. The development of abundant elemental sulfur in concert with the pronounced drop in sulfide concentration can only be explained if synproportionation (eq. 5.3) took place in the reactor.

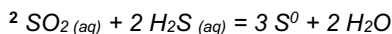
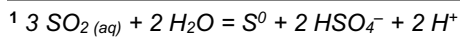
### Thermodynamics

Besides mass balance constraints, we explored how the energetics of the proposed synproportionation reaction compares to the common SO<sub>2</sub> disproportionation. This was already attempted by Kürzinger et al. (2022), but there were large uncertainties in pH and sulfide concentrations. Based on the new tight experimental constraints, we revised the energetics of the synproportionation to provide new comparative values for the energetics of the syn- and disproportionation pathway of elemental sulfur formation. For the measured low pH of ~1.2 in experiment #2 and #3 the dissociation equilibrium is predicted to lie entirely on the undissociated side with sulfur in solution remaining present as SO<sub>2</sub> and H<sub>2</sub>S (Figure 5.5). Results for Δ<sub>R</sub>G for the dis- and synproportionation reactions over a temperature range from 0 to 300 °C are listed in Table 5.4. They were calculated using the concentrations and activity coefficients (γ) provided in the footnote of Table 5.4 and are shown in Figure 5.6.

**Table 5.4**

Log K, standard state Gibbs energy (Δ<sub>R</sub>G<sup>0</sup>) and Gibbs energy (Δ<sub>R</sub>G) values for dis- and synproportionation reactions over a temperature range from 0 to 300 °C and constant pressures (p = 30 MPa).

Temp. [°C]	Disproportionation <sup>1</sup>								Synproportionation <sup>2</sup>		
	pH <sub>in-situ</sub>	Log K <sub>1</sub>	γ <sub>HSO4</sub>	γ <sub>SO4</sub>	Log K	Δ <sub>R</sub> G <sup>0</sup>	Log Q	Δ <sub>R</sub> G	Log K	Δ <sub>R</sub> G <sup>0</sup>	Δ <sub>R</sub> G
0	1.20	-1.59	0.69	0.20	27.40	-143.29	4.68	-118.82	23.32	-121.94	-93.73
20	1.20	-1.81	0.69	0.20	24.46	-137.28	4.67	-111.05	21.20	-118.95	-88.67
40	1.22	-2.07	0.68	0.19	21.73	-130.29	4.71	-102.08	19.25	-115.38	-83.03
60	1.25	-2.34	0.67	0.18	19.21	-122.51	4.75	-92.19	17.47	-111.39	-76.98
80	1.28	-2.62	0.66	0.16	16.87	-114.04	4.80	-81.60	15.84	-107.08	-70.60
100	1.29	-2.91	0.65	0.15	14.69	-104.94	4.81	-70.62	14.35	-102.50	-63.94
120	1.30	-3.19	0.64	0.14	12.66	-95.26	4.81	-59.08	12.98	-97.71	-57.09
140	1.32	-3.48	0.62	0.13	10.75	-85.06	4.83	-46.88	11.75	-92.91	-50.23
160	1.34	-3.77	0.61	0.12	8.96	-74.30	4.85	-34.08	10.60	-87.93	-43.17
180	1.35	-4.06	0.59	0.11	7.26	-62.95	4.85	-20.90	9.54	-82.76	-35.94
200	1.38	-4.35	0.57	0.10	5.63	-51.01	4.88	-6.81	8.55	-77.42	-28.53
220	1.40	-4.65	0.56	0.09	4.07	-38.44	4.89	7.76	7.62	-71.91	-20.95
240	1.44	-4.95	0.53	0.07	2.56	-25.19	4.94	23.31	6.74	-66.22	-13.19
260	1.50	-5.26	0.51	0.06	1.10	-11.18	5.01	39.99	5.91	-60.34	-5.25
280	1.56	-5.59	0.48	0.05	-0.35	3.72	5.09	57.62	5.13	-54.27	2.88
300	1.67	-5.94	0.45	0.04	-1.80	19.69	5.25	77.34	4.37	-47.97	11.25



Δ<sub>R</sub>G = Δ<sub>R</sub>G<sup>0</sup> + 2.303 + R T Log Q. In-situ pH and γ-values for HSO<sub>4</sub><sup>-</sup> and SO<sub>4</sub><sup>2-</sup> were calculated for a 400 mM NaCl solution with 20 mM SO<sub>4</sub><sup>2-</sup>. The b-dot extended Debye-Hückel equation was used to calculate the activity coefficients following Helgeson (1969). The activities required to compute Log Q were calculated using the following concentrations: 20 mM for SO<sub>2(aq)</sub> and 10 mM for H<sub>2</sub>S. The γ-values were assumed unity for neutral species. For the activity of HSO<sub>4</sub><sup>-</sup>, fractions of HSO<sub>4</sub><sup>-</sup> and SO<sub>4</sub><sup>2-</sup> were calculated based on a total sulfate concentration of 20 mM and from the listed γ-values (for the dissociation reaction  $\text{HSO}_4^- = \text{SO}_4^{2-} + \text{H}^+$ ).

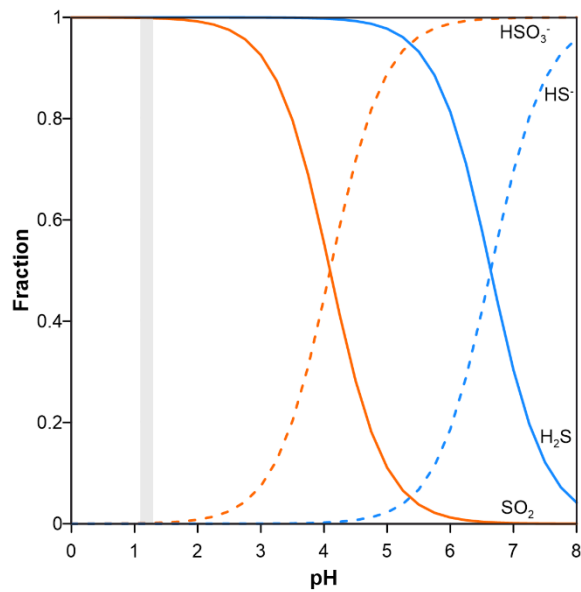


**Figure 5.5.** Effect of pH on the fractionation of  $\text{SO}_2$  and  $\text{H}_2\text{S}$  at  $\sim 220^\circ\text{C}$  (modified after Kürzinger et al., 2022). The measured pH of the experiment in which sulfur was formed is indicated by the shaded bar.

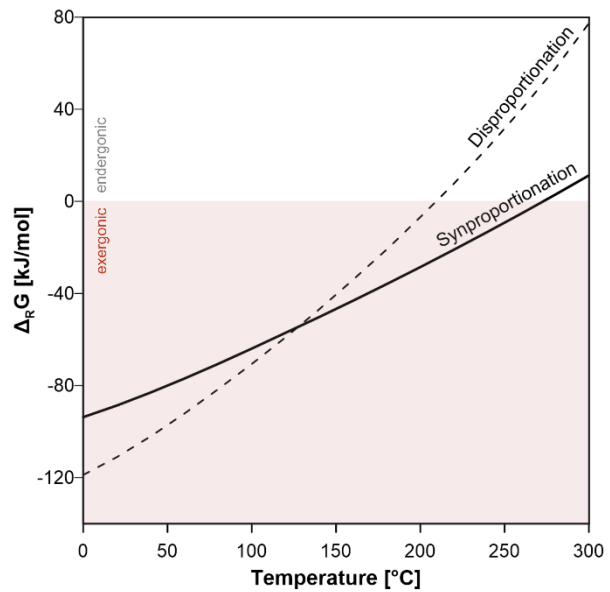


**Figure 5.6.** Gibbs energy of disproportionation and synproportionation reactions as function of temperature at isobaric conditions ( $p = 30\text{ MPa}$ ). Synproportionation stays exergonic to  $275^\circ\text{C}$ , while disproportionation reaches a chemical equilibrium at  $\sim 210^\circ\text{C}$ . See Table 5.4 for details.

At lower temperatures, both reactions are clearly exergonic, while the disproportionation reaction becomes endergonic at temperatures  $> 210^\circ\text{C}$ . Synproportionation, however, remains exergonic up to a temperature of about  $275^\circ\text{C}$  at the selected conditions ( $p = 30\text{ MPa}$ ). From an energetic perspective, both reactions are likely to occur in the experiment. But even if the disproportionation reaction is endergonic at the target temperature of  $220^\circ\text{C}$ , this sulfur formation process cannot be entirely excluded. The experimentally generated elemental sulfur could have formed by disproportionation during the cooling phase as the system passed through the temperature range in which this reaction would be predicted to take place.

The formation of  $\text{H}_2$  in the experiment, although in very small amounts of  $5$  to  $10\ \mu\text{mol/L}$ , indicates that another, subordinate reaction must have taken place in addition to the dominant synproportionation. A possible explanation for this can be given by partial oxidation of  $\text{SO}_2$  (eq. 5.8), which is also in agreement with thermodynamic predictions at the given conditions. Formation of sulfuric acid plus  $\text{H}_2$  by partial  $\text{SO}_2$  oxidation would thus explain the expected low pH at Toxic Castle (Kemp Caldera) and the relatively high amount of dissolved  $\text{H}_2$  in the fluids ( $14.1\ \mu\text{mol/kg}$  compared to the neighboring Great Wall location with only  $1.0\ \mu\text{mol/kg}\ \text{H}_2$ ; Kürzinger et al., 2022).

### Isotopes

To further illuminate sulfur formation process, we used the known initial isotopic composition of the reactants (Table 5.2) to construct a set of Rayleigh fractionation models for the different possible formation pathways (see appendix for details) and plotted the results together with the measured isotopic values of the sulfur recovered from the experiments (Figure 5.7). Another sulfur formation mechanism could be  $\text{SO}_4$  reduction, but these values could not be calculated because we did not have an initial  $\delta^{34}\text{S}_{\text{SO}_4}$  value due to no existing sulfate at the beginning of the experiment.

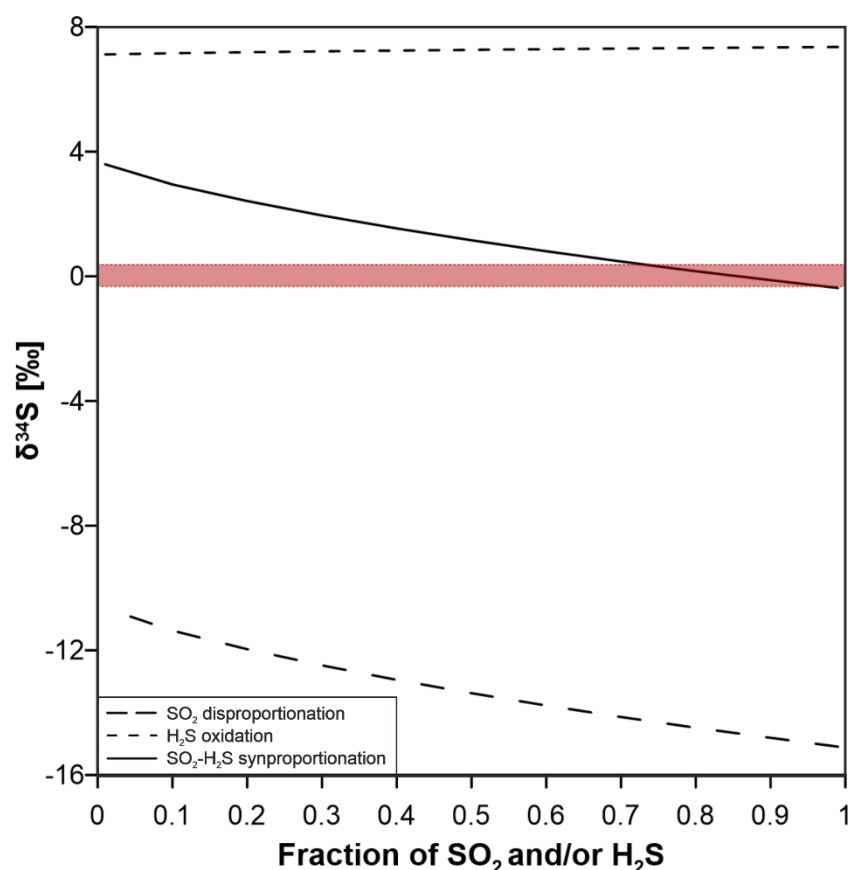
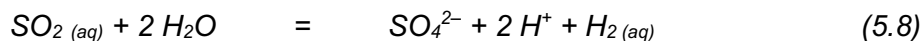


**Figure 5.7.** Results of expected  $\delta^{34}\text{S}$  values for sulfur formed by  $\text{SO}_2$  disproportionation,  $\text{H}_2\text{S}$  oxidation and synproportionation of  $\text{SO}_2$  and  $\text{H}_2\text{S}$  at 220 °C. The horizontal red bar represents the measured  $\delta^{34}\text{S}$  values of elemental sulfur obtained from the experiments ( $\delta^{34}\text{S} = -0.3$  to  $0.4$  ‰). The calculated isotopic composition for  $\text{H}_2\text{S}$  oxidation ranging from 7.12 to 7.36 ‰ plot outside the measured  $\delta^{34}\text{S}$  range of elemental sulfur. The  $\delta^{34}\text{S}$  range for  $\text{SO}_2$  disproportionation shows values between  $-15.1$  and  $-10.6$  ‰, which are far too negative. Only the sulfur values predicted for  $\text{SO}_2$ - $\text{H}_2\text{S}$  synproportionation ( $\delta^{34}\text{S} = -0.4$  to  $3.6$  ‰) fit with the measured  $\delta^{34}\text{S}$  values of sulfur.

The calculated values for H<sub>2</sub>S oxidation as well as SO<sub>2</sub> disproportionation fall outside the measured range because they are either far too negative or too positive (see Figure 5.7). Thus, these reactions can be excluded as a possible sulfur formation process. However, the calculation results suggest that δ<sup>34</sup>S<sub>S</sub> values resulting from SO<sub>2</sub>–H<sub>2</sub>S synproportionation are consistent with the measured sulfur isotope values (δ<sup>34</sup>S = –0.3 to 0.4 ‰) of elemental sulfur retrieved from experiments #2 and #3.

We have now presented three lines of evidence (mass balance, energetics and isotopic composition) to demonstrate that synproportionation can explain the formation of sulfur. But this formation process would exclusively produce elemental sulfur and water (eq. 5.3), no sulfate or sulfuric acid as it is the case with disproportionation (eq. 5.1 and 5.2). Sulfate was clearly recovered during sampling of the experiments (in the 5 or 10 mL subsample) and thus, it seems obvious that the sulfate was formed by disproportionation subordinated to the synproportionation reaction. But the modelled expected isotopic composition for sulfate formed through disproportionation (δ<sup>34</sup>S<sub>SO<sub>4</sub></sub> values in the range of 6.3 to 11.6 ‰ at 220 °C) is considerably lower than the measured value of 23.6 ‰. We hence suggest that the sulfate occurring in the experiments has been formed through partial oxidation of the residual SO<sub>2</sub> (eq. 5.8). Because SO<sub>2</sub> is highly soluble in water and because of its intermediate oxidation state, it can act as reducing and oxidizing agent.



In case of our experiments, 10 to 30 % of SO<sub>2</sub> and H<sub>2</sub>S have been reacted to form elemental sulfur via synproportionation. This percentage is also in agreement with the (calculated) mass balance of the total sulfur amount (cf. Table 5.3). The 10 to 30 % of the SO<sub>2</sub>–H<sub>2</sub>S turnover translates to a maximum δ<sup>34</sup>S value of 1.6 ‰ for the residual SO<sub>2</sub> (compared to the initial δ<sup>34</sup>S<sub>SO<sub>2</sub></sub> = –2.8 ‰). We further investigated the changing isotopic composition of sulfate formed by oxidation of the residual SO<sub>2</sub> over a temperature range from 100 to 220 °C (Figure 5.8).

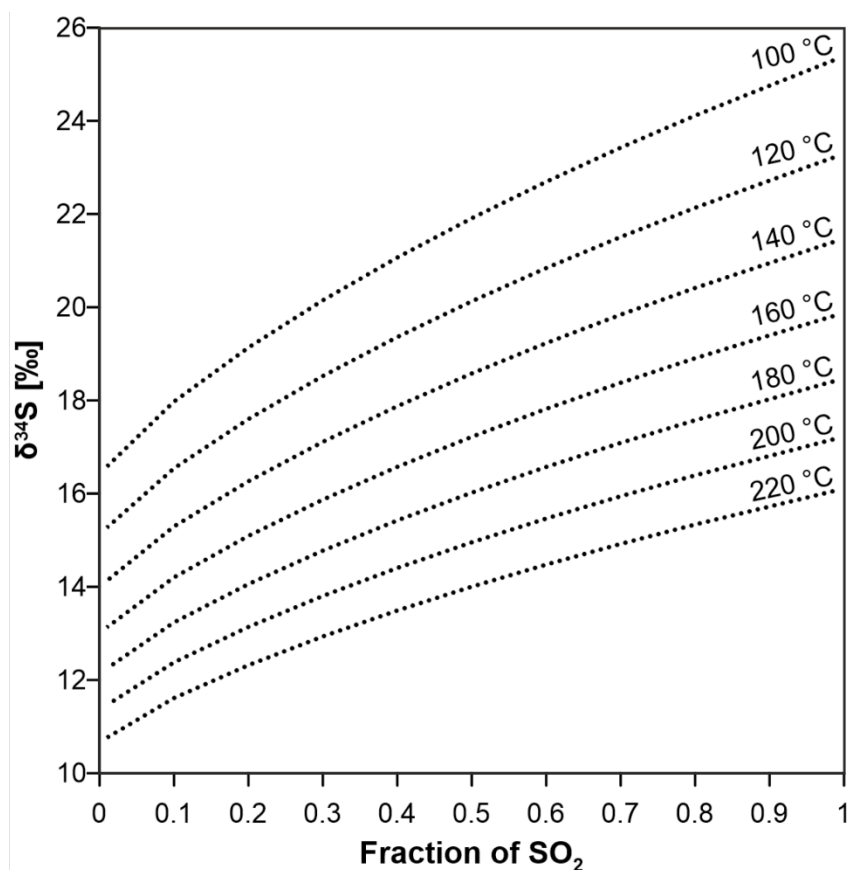


**Figure 5.8.** Plot of  $\delta^{34}\text{S}_{\text{SO}_4}$  vs. fraction of reacting  $\text{SO}_2$  for  $\text{SO}_2$  oxidation to sulfate. With an initial  $\delta^{34}\text{S}_{\text{SO}_2}$  value of 1.6, the sulfate formed by oxidation becomes more  $^{34}\text{S}$ -enriched with decreasing temperature. The isotopic value of the experimentally formed sulfur ( $\delta^{34}\text{S}_{\text{SO}_4} = 23.6 \text{ ‰}$ ) would plot between the 100 °C and 120 °C curve at fractions between 0.7 and 1. Note: The equilibrium isotopic fractionation factors ( $\alpha$ ) between the sulfur compounds are only valid for temperatures > 200 °C (see appendix). For temperatures < 200 °C,  $\alpha$  values were extrapolated.

Accordingly, barite retrieved from experiment #3 likely formed during the cooling process at a temperature between 100 and 120 °C. For the derived isotopic value of the residual  $\text{SO}_2$  ( $\delta^{34}\text{S}_{\text{SO}_2} = 1.6$ ), the corresponding sulfate would range between  $\delta^{34}\text{S}$  values of 15.3 and 25.3 ‰. The measured value of 23.6 ‰ would thus fall exactly within this range.

The detailed evaluation of the experiments conducted in this study help us to understand the peculiar observations made at Kemp Caldera and thereby contributed to a better understanding of the great variability of processes in arc and back-arc systems.

## 5.5 Conclusion

Experiments conducted at *in-situ* conditions enable a novel systematic investigation of elemental sulfur formation in hydrothermal environments. As mentioned by Peters et al. (2021) and Kürzinger et al. (2022), isotopically heavy sulfur requires a different origin than the common disproportionation. We previously speculated about possible synproportionation which is supposed to take place in the Kemp Caldera hydrothermal system. Hence, the measured  $\delta^{34}\text{S}_\text{s}$  values of experimentally generated elemental sulfur are consistent with values predicted by a Rayleigh fractionation model for  $\text{SO}_2\text{--H}_2\text{S}$  synproportionation. Moreover, the experiments revealed that synproportionation is not only a theoretical possibility, but it actually occurred during the experiments. Thermodynamic modelling further shows that from a perspective of energetics, synproportionation is also more favorable than the common disproportionation at the investigated conditions. Taken together, these results demonstrate that the sulfur formation mechanism of synproportionation can take place in natural hydrothermal environments and may represent a previously overlooked source of isotopically heavy sulfur.

## Acknowledgements

We thank the working group of W. Bach (University of Bremen, Germany) for providing the laboratories and the Dickson-type reactor that we were allowed to use for the hydrothermal experiments. We also thank P. Witte (University of Bremen, Germany) for the support with SEM-EDX analysis.

Additional funding was provided by the Deutsche Forschungsgemeinschaft (DFG, German Research Foundation) under Germany's Excellence Strategy, EXC-2077 – 390741603. Funding for the hydrothermal apparatus was provided by a MARUM incentive fund to W. Bach.

## 6 CONCLUSIONS AND OUTLOOK

The results of this work provide a more detailed picture of the Kemp Caldera, its formation and evolution, and the characteristics of its hydrothermal system.

The caldera was formed by at least one collapse event caused by magma withdrawal from the underlying magma chamber. The resulting ring faults close to the caldera rim acted and still act as pathways for penetrating seawater and hydrothermal fluids, so that hydrothermal activity is focused at the rim (Figure 6.1A). A local intrusion and a dacitic post-caldera eruption have caused uplift in the western part of the caldera and the formation of a resurgent cone in the central area (Figure 6.1B). Due to this extrusion, smaller faults and fissures around the resurgent cone have formed, where heat flow and hydrothermal activity is now focused as well.

The hydrothermal system of the Kemp Caldera seems to be a combination of two hydrothermal systems: Beehive Chimney at the Flare site shows typical mineral assemblages and fluid composition of seawater-rock-dominated hydrothermal systems, while the central Vent field is dominated by white smoker vents, which are common for magmatic-hydrothermal systems (Figure 6.1B and 6.1C). A signature feature especially of magmatic-hydrothermal systems is the formation of sulfur. At the Vent field sites Great Wall and Toxic Castle, elemental sulfur in fine-crystalline and liquid form, respectively, was found and further analyzed. The peculiarity of the sulfur is its uncommonly heavy isotopic composition with positive  $\delta^{34}\text{S}$  values ranging from 5.2 to 5.8 ‰, and its formation at pH-values much higher than observed in other systems. Both the isotopic composition and the pH are incompatible with the formation by  $\text{SO}_2$  disproportionation. Sulfur formation by disproportionation is a typical process in arc and back-arc environments. The sulfur precipitates from acid-sulfate fluids, and typically shows  $\delta^{34}\text{S}$  values  $< 0$  ‰. Accordingly, the sulfur from the Kemp Caldera must have a different origin. It is suggested that sulfur formation within the Kemp Caldera hydrothermal system is attributed to synproportionation of  $\text{SO}_2$  and  $\text{H}_2\text{S}$ . In this reaction,  $\text{SO}_2$  reacts with  $\text{H}_2\text{S}$  to form  $\text{S}^0$  and water, so that higher pH-values are more likely compared to the pH resulting from the sulfur plus sulfuric acid formation by disproportionation. To evaluate the feasibility of the synproportionation reaction, a Rayleigh fractionation model was applied. The measured  $\delta^{34}\text{S}$  values of the Kemp Caldera sulfur match the values predicted by the Rayleigh model. Moreover, experiments were conducted at hydrothermal conditions to gain a better insight into the synproportionation process. The isotope values of the experimentally generated sulfur were also consistent with the values calculated by the Rayleigh fractionation model adjusted to the experimental conditions. Together with thermodynamic modelling, the results therefore demonstrate that synproportionation is more favorable at the investigated (*in-situ*) conditions than the common disproportionation of magmatic  $\text{SO}_2$ .

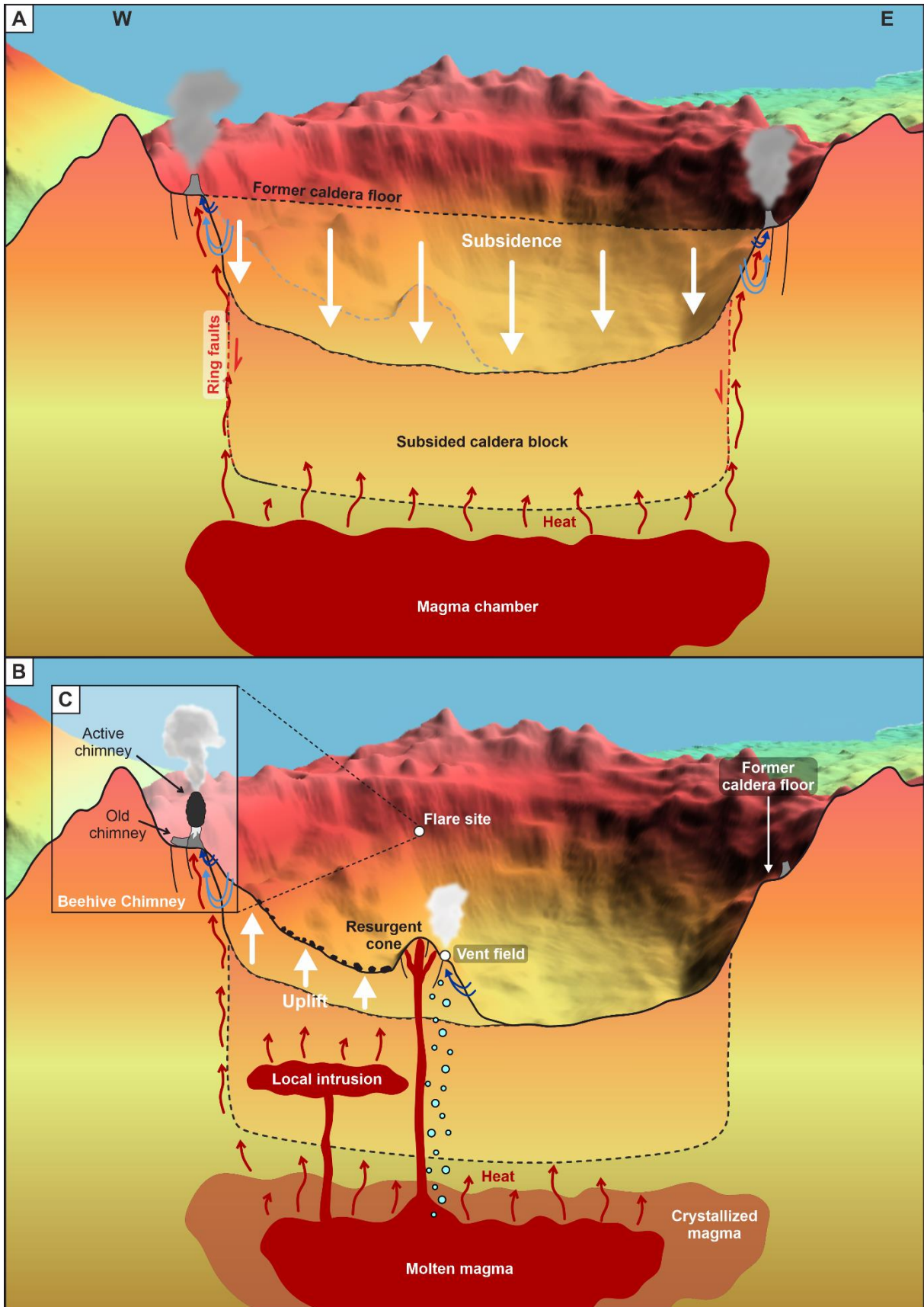


**Figure 6.1.** Cross-section through the Kemp Caldera from W to E to schematically illustrate its formation and development. A) Sketch of a subsidence event as a result of magma chamber roof collapse due to magma withdrawal. Resulting ring faults close to the caldera margin act as pathways for infiltrating seawater and hydrothermal fluids. The processes taking place there, indicated by the light and dark blue arrows in (A) and (B), are explained in more detail in Figure 1.5, B) Present state of the Kemp Caldera. Uplift of the western caldera floor may be caused by a local intrusion. A post-caldera eruption in the central part causes the development of a resurgent cone, which is accompanied by the formation of fissures and small faults. Due to the now provided pathways for hydrothermal fluids, heat flow as well as hydrothermal flow is now focused around the cone in addition to the hydrothermal activity at the caldera rim. The Vent field located at the eastern flank of the resurgent cone is dominated by white smoker vents. Elemental sulfur is found in crystalline and liquid form around the active vents, and C) Beehive Chimney at the Flare site at the NNW caldera rim is characterized by fluids that are typical for seawater-rock-dominated hydrothermal systems. At this site, inactive chimneys were found beside actively venting chimneys, consisting of barite and sulfide minerals.

Although synproportionation can occur in natural hydrothermal systems, as was demonstrated, an open question is at which conditions this reaction dominates over other sulfur forming processes. The phenomenon of isotopically heavy sulfur has been observed in only a few submarine hydrothermal systems. Thus, further investigations are needed to study the processes and behavior of sulfur formation in modern hydrothermal systems.

To get more information about the formation and development of the Kemp Caldera, rock samples from the caldera rim and the caldera interior are required. We know that the rocks of the central post-caldera eruption are of dacitic composition, but whether the caldera was originally basaltic/andesitic like the neighboring Kemp Seamount remains uncertain for now. Moreover, further ocean bottom (seismic) experiments could provide better insights into the rate of activity of the caldera's resurgent cone. Additional high-resolution data derived from micro-bathymetric mapping would provide more detailed information about the caldera morphology and would enable the mapping of faults around the resurgent cone.



## ACKNOWLEDGEMENTS

Albert Einstein once said: “Do not give up what is important to you just because it is not easy.” And he was right! My work was always important to me, but writing this thesis was not always easy and sometimes additional obstacles were put in the way. However, I had many people by my side who comforted and motivated me, and who helped me to get these obstacles out of the way.

First of all, I want to thank my supervisors Gerhard Bohrmann and Wolfgang Bach for their encouraging support through the last three years. They were on hand with help and advice for me. Even when they were on field trips, they answered my questions and mails, and always had time for me when I asked for a meeting. And many thanks to Colin Devey, who agreed to be the second reviewer of my thesis.

A big thanks to Thomas Pape and Alexander Diehl, who not only supported me as members of my thesis committee, but also always had an open door when I needed some help.

Special thanks to Petra Witte. She helped me with the SEM images and EDX analyses and introduced me to the technique and the programs that I could do the measurements and images on my own, spending hours and even days in her lab. I would also like to thank Harald Strauss for the nice phone calls we had in the course of sulfur isotope analyses.

Stefan Sopke and Anne Hübner – thank you for helping me with the microprobe measurements and rock sample preparation for thin sections. Special thanks here again to Anne Hübner, because I was allowed to put the rock preparation lab under water for a private rock sample.

My thanks go to Michael Magnus, who supported and motivated me already in my bachelor studies and helped me with the total microscopic images of the thin sections for one of my manuscripts. I would also like to mention Simone Kasemann. She actually had nothing to do with my work, but she took her time for me to talk a bit about submarine hydrothermal systems.

I would like to thank Janice Malnati for her support in the lab during my first months in the working group. Besides lab work, she always had something for me to do, like cleaning the archive room louver listening to Christmas songs in autumn.

Thank you to the colleagues of my working group. They have not only supported me mentally in the last three years, but have also ensured my physical well-being (with cake and other delicious things). And a special thanks to my fellow PhD students Yiting Tseng, Mechthild Doll and Nina Lešić, with whom I spent knitting afternoons, relaxing work in the lab with audio books and many hilarious moments in the office – you have become good friends to me.

## Acknowledgements

---

Special thanks also to Katharina Streuff, Lisa-Maria Röhling and Dorothea Gertler. They took the time for a last-minute read of my work and gave me feedback, even though they have enough to do for their own work.

Finally, and most of all, I would like to thank my family and my friends! Especially the non-scientific but rather heartfelt support and their positive spirit were often the best thing that could have happened to me. They understood when I didn't get in touch for what felt like eternities because I had too much to do, but they were always there for me when I needed them.

## REFERENCES

- Acocella V. (2021) Calderas. In: *Volcano-Tectonic Processes*: Springer, Cham, pp. 163–203. [https://link.springer.com/chapter/10.1007/978-3-030-65968-4\\_5](https://link.springer.com/chapter/10.1007/978-3-030-65968-4_5). DOI: 10.1007/978-3-030-65968-4\_5.
- Acocella V., Palladino D. M., Cioni R., Russo P., Simei S. (2012) Caldera structure, amount of collapse, and erupted volumes: The case of caldera, Italy. *GSA Bulletin* **124** (9/10), pp. 1562–1576.
- Aiuppa A., Inguaggiato S., McGonigle A., O'Dwyer M., Oppenheimer C. et al. (2005) H<sub>2</sub>S fluxes from Mt. Etna, Stromboli, and Vulcano (Italy) and implications for the sulfur budget at volcanoes. *Geochimica et Cosmochimica Acta* **69** (7), pp. 1861–1871. DOI: 10.1016/j.gca.2004.09.018.
- Alt J. C., Shanks W. C., Jackson M. C. (1993) Cycling of sulfur in subduction zones: The geochemistry of sulfur in the Mariana Island Arc and back-arc trough. *Earth and Planetary Science Letters* **119** (4), pp. 477–494. DOI: 10.1016/0012-821X(93)90057-G.
- Amcoff Ö. (1988) Experimental replacement of chalcopyrite by bornite: Textural and chemical changes during a solid-state process. *Mineral. Deposita* **23** (4), pp. 286–292. DOI: 10.1007/BF00206409.
- Amon D. J., Glover A. G., Wiklund H., Marsh L., Linse K. et al. (2013) The discovery of a natural whale fall in the Antarctic deep sea. *Deep Sea Research Part II: Topical Studies in Oceanography* **92**, pp. 87–96. DOI: 10.1016/j.dsr2.2013.01.028.
- Arango C. P., Linse K. (2015) New Sericosura (Pycnogonida:Ammonotheidae) from deep-sea hydrothermal vents in the Southern Ocean. *Zootaxa* **3995** (1), pp. 37–50. DOI: 10.11646/zootaxa.3995.1.5.
- Baker P. E., Holgate M. W., Longton R. E., Tilbrook P. J., Tomblin J. F. et al. (1964) A Survey of the South Sandwich Islands. *Nature* **203** (4946), pp. 691–693. DOI: 10.1038/203691a0.
- Barker P. F. (2001) Scotia Sea regional tectonic evolution: implications for mantle flow and palaeocirculation. *Earth-Science Reviews* **55** (1-2), pp. 1–39. DOI: 10.1016/S0012-8252(01)00055-1.
- Barry T. L., Pearce J. A., Leat P. T., Millar I. L., Le Roex A. P. (2006) Hf isotope evidence for selective mobility of high-field-strength elements in a subduction setting: South Sandwich Islands. *Earth and Planetary Science Letters* **252** (3-4), pp. 223–244. DOI: 10.1016/j.epsl.2006.09.034.

- Beaulieu S. E., Szafranski K. M. (2020) InterRidge Global Database of Active Submarine Hydrothermal Vent Fields Version 3.4, zuletzt geprüft am 8/24/2021. DOI: 10.1594/PANGAEA.917894.
- Berkenbosch H. A., de Ronde C. E. J., Gemmell J. B., McNeill A. W., Goemann K. (2012) Mineralogy and Formation of Black Smoker Chimneys from Brothers Submarine Volcano, Kermadec Arc. *Economic Geology* **107**, pp. 1613–1633. DOI: 10.2113/econgeo.107.8.1613.
- Berkenbosch H. A., Ronde C. E. J. de, Paul B. T., Gemmell J. B. (2015) Characteristics of Cu isotopes from chalcopyrite-rich black smoker chimneys at Brothers volcano, Kermadec arc, and Niutahi volcano, Lau basin. *Mineral. Deposita* **50** (7), pp. 811–824. DOI: 10.1007/s00126-014-0571-y.
- Bogie I., Lawless J. V., Rychagov S., Belousov V. (2005) Magmatic-related hydrothermal systems: Classification of the types of geothermal systems and their ore mineralization. *Proceedings of geoconference in Russia, Kuril*, pp. 51–73.
- Bohrmann G. (2019) The Expedition PS119 of the Research Vessel POLARSTERN to the Eastern Scotia Sea in 2019. Reports on Polar and Marine Research. Alfred-Wegener-Institut, Helmholtz-Zentrum für Polar- und Meeresforschung, Bremerhaven, Germany. DOI: 10.2312/BZPM\_0736\_2019.
- Branney M., Acocella V. (2015) Calderas. In: Haraldur Sigurdsson und B. F. Houghton (Hg.): *Encyclopedia of volcanoes*. Second edition. Amsterdam, Boston: Elsevier/AP, Academic Press is an imprint of Elsevier, pp. 299–315. DOI: 10.1016/B978-0-12-385938-9.00016-X.
- Branney M. J. (1995) Downsag and extension at calderas: new perspectives on collapse geometries from ice-melt, mining, and volcanic subsidence. *Bull Volcanol*, pp. 303–318.
- Bruguier N. J., Livermore R. A. (2001) Enhanced magma supply at the southern East Scotia Ridge: evidence for mantle flow around the subducting slab? *Earth and Planetary Science Letters* **191** (1-2), pp. 129–144. DOI: 10.1016/S0012-821X(01)00408-3.
- Butterfield D. A., McDuff R. E., Mottl M. J., Lilley M. D., Lupton J. E., Massoth G. J. (1994) Gradients in the composition of hydrothermal fluids from the Endeavour segment vent field: Phase separation and brine loss. *J. Geophys. Res.* **99** (B5), pp. 9561–9583. DOI: 10.1029/93JB03132.
- Butterfield D. A., Nakamura K., Takano B., Lilley M. D., Lupton J. E. et al. (2011) High SO<sub>2</sub> flux, sulfur accumulation, and gas fractionation at an erupting submarine volcano. *Geology* **39** (9), pp. 803–806. DOI: 10.1130/G31901.1.

- Capasso G., Favara R., Inguaggiato S. (1997) Chemical features and isotopic composition of gaseous manifestations on Vulcano Island, Aeolian Islands, Italy: An interpretative model of fluid circulation. *Geochimica et Cosmochimica Acta* **61** (16), pp. 3425–3440. DOI: 10.1016/S0016-7037(97)00163-4.
- Caress D. W., Chayes D. N., dos Santos Ferreira C. (2017) MB-system: Mapping the Seafloor. *Moss Landing, CA: Monterey Bay Aquariun Research Institute* ,
- Chan S. H. (1989) A review on solubility and polymerization of silica. *Geothermics* **18** (1-2), pp. 49–56. DOI: 10.1016/0375-6505(89)90009-6.
- Cline J. D. (1969) Spectrophotometric determination of hydrogen sulfide in natural waters. *Limnol. Oceanogr.* **14** (3), pp. 454–458. DOI: 10.4319/lo.1969.14.3.0454.
- Cole C. S., James R. H., Connelly D. P., Hathorne E. C. (2014) Rare earth elements as indicators of hydrothermal processes within the East Scotia subduction zone system. *Geochimica et Cosmochimica Acta* **140**, pp. 20–38. DOI: 10.1016/j.gca.2014.05.018.
- Cole J. W., Milner D. M., Spinks K. D. (2005) Calderas and caldera structures: a review. *Earth-Science Reviews* **69** (1-2), pp. 1–26. DOI: 10.1016/j.earscirev.2004.06.004.
- Connor C. B., Clement B. M., Song X., Lane S. B., West-Thomas J. (1993) Continuous monitoring of high-temperature fumaroles on an active lava dome, Volcán Colima, Mexico: Evidence of mass flow variation in response to atmospheric forcing. *J. Geophys. Res.* **98** (B11), pp. 19713–19722. DOI: 10.1029/93JB02169.
- Cooke D. R., Simmons S. F. (2000) Characteristics and Genesis of Epithermal Gold Deposits. In: Philip E. Brown und Steffen G. Hagemann (Hg.): Gold in 2000 /volume eds. G. Steffen Hagemann ; E. Philip Brown. Society of Economic Geologists: Society of Economic Geologists (Reviews in economic geology, 13), pp. 221–244. DOI: 10.5382/Rev.13.06.
- Corliss J. B., Dymond J., Gordon L. I., Edmond J. M., Herzen R. P. von et al. (1979) Submarine Thermal Springs on the Galapagos Rift. *Science* **203** (4385), pp. 1073–1083. DOI: 10.1126/science.203.4385.1073.
- de Ronde C. E. J., Baker E. T., Massoth G. J., Lupton J. E., Wright I. C. et al. (2001) Intra-oceanic subduction-related hydrothermal venting, Kermadec volcanic arc, New Zealand. *Earth and Planetary Science Letters* **193** (3-4), pp. 359–369. DOI: 10.1016/S0012-821X(01)00534-9.
- de Ronde C. E. J., Chadwick W. W., Ditchburn R. G., Embley R. W., Tunncliffe V. et al. (2015) Molten Sulfur Lakes of Intraoceanic Arc Volcanoes. In: Dmitri Rouwet, Bruce Christenson, Franco Tassi und Jean Vandemeulebrouck (Hg.): Volcanic Lakes. Berlin, Heidelberg:

- Springer Berlin Heidelberg (Advances in Volcanology), pp. 261–288. DOI: 10.1007/978-3-642-36833-2\_11.
- de Ronde C. E. J., Faure K., Bray C. J., Chappell D. A., Wright I. C. (2003) Hydrothermal fluids associated with seafloor mineralization at two southern Kermadec arc volcanoes, offshore New Zealand. *Miner Deposita* **38** (2), pp. 217–233. DOI: 10.1007/s00126-002-0305-4.
- de Ronde C. E. J., Hannington M. D., Stoffers P., Wright I. C., Ditchburn R. G. et al. (2005) Evolution of a Submarine Magmatic-Hydrothermal System: Brothers Volcano, Southern Kermadec Arc, New Zealand **100** (6), pp. 1097–1133. DOI: 10.2113/gsecongeo.100.6.1097.
- de Ronde C. E. J., Humphris S. E., Höfig T. W., Reyes A. G. (2019) Critical role of caldera collapse in the formation of seafloor mineralization: The case of Brothers volcano. *Geology* **47** (8), pp. 762–766. DOI: 10.1130/G46047.1.
- de Ronde C. E. J., Massoth G. J., Butterfield D. A., Christenson B. W., Ishibashi J. et al. (2011) Submarine hydrothermal activity and gold-rich mineralization at Brothers Volcano, Kermadec Arc, New Zealand. *Miner Deposita* **46** (5-6), pp. 541–584. DOI: 10.1007/s00126-011-0345-8.
- de Ronde C. E. J., Stucker V. K. (2015) Seafloor Hydrothermal Venting at Volcanic Arcs and Backarcs. In: Haraldur Sigurdsson und B. F. Houghton (Hg.): Encyclopedia of volcanoes. Second edition. Amsterdam, Boston: Elsevier/AP, Academic Press is an imprint of Elsevier, pp. 823–849. DOI: 10.1016/B978-0-12-385938-9.00047-X.
- Des Marais D. J., Walter M. R. (2019) Terrestrial Hot Spring Systems: Introduction. *Astrobiology* **19** (12), pp. 1419–1432. DOI: 10.1089/ast.2018.1976.
- Dickson F. W., Blount C. W., Tunell G. (1963) Use of hydrothermal solution equipment to determine the solubility of anhydrite in water from 100 degrees C to 275 degrees C and from 1 bar to 1000 bars pressure. *American Journal of Science* **261** (1), pp. 61–78. DOI: 10.2475/ajs.261.1.61.
- Diehl A., Bach W. (2020) MARHYS (MARine HYdrothermal Solutions) Database: A Global Compilation of Marine Hydrothermal Vent Fluid, End Member, and Seawater Compositions. *Geochem. Geophys. Geosyst.* **21** (12). DOI: 10.1029/2020GC009385.
- Diehl A., Ronde C. E. J. de, Bach W. (2020) Subcritical Phase Separation and Occurrence of Deep-Seated Brines at the NW Caldera Vent Field, Brothers Volcano: Evidence from Fluid Inclusions in Hydrothermal Precipitates. *Geofluids* **2020**, pp. 1–22. DOI: 10.1155/2020/8868259.

- Duggen S., Portnyagin M., Baker J., Ulfbeck D., Hoernle K. et al. (2007) Drastic shift in lava geochemistry in the volcanic-front to rear-arc region of the Southern Kamchatkan subduction zone: Evidence for the transition from slab surface dehydration to sediment melting. *Geochimica et Cosmochimica Acta* **71** (2), pp. 452–480. DOI: 10.1016/j.gca.2006.09.018.
- Eddy C. A., Dilek Y., Hurst S., Moores E. M. (1998) Seamount formation and associated caldera complex and hydrothermal mineralization in ancient oceanic crust, Troodos ophiolite (Cyprus). *Tectonophysics* **292** (3-4), pp. 189–210. DOI: 10.1016/S0040-1951(98)00064-X.
- Eldridge D. L., Guo W., Farquhar J. (2016) Theoretical estimates of equilibrium sulfur isotope effects in aqueous sulfur systems: Highlighting the role of isomers in the sulfite and sulfoxylate systems. *Geochimica et Cosmochimica Acta* **195**, pp. 171–200. DOI: 10.1016/j.gca.2016.09.021.
- Embley R. W., Jonasson I. R., Perfit M. R., Franklin J. M., Tivey M. A. et al. (1988) Submersible investigation of an extinct hydrothermal system on the Galapagos Ridge; sulfide mounds, stockwork zone, and differentiated lavas. *Canadian Mineralogist* **26**, pp. 517–539.
- Fischer T. P., Chiodini G. (2015) Volcanic, Magmatic and Hydrothermal Gases. In: Haraldur Sigurdsson und B. F. Houghton (Hg.): Encyclopedia of volcanoes. Second edition. Amsterdam, Boston: Elsevier/AP, Academic Press is an imprint of Elsevier, pp. 779–797. DOI: 10.1016/B978-0-12-385938-9.00045-6.
- Fischer T. P., Giggenbach W. F., Sano Y., Williams S. N. (1998) Fluxes and sources of volatiles discharged from Kudryavy, a subduction zone volcano, Kurile Islands. *Earth and Planetary Science Letters* **160** (1-2), pp. 81–96. DOI: 10.1016/S0012-821X(98)00086-7.
- Fischer T. P., Sturchio N. C., Stix J., Arehart G. B., Counce D., Williams S. N. (1997) The chemical and isotopic composition of fumarolic gases and spring discharges from Galeras Volcano, Colombia. *Geology* **77** (1-4), pp. 229–253. DOI: 10.1016/S0377-0273(96)00096-0.
- Fleet M. E. (1970) Structural aspects of the marcasite-pyrite transformation. *The Canadian Mineralogist* **10** (2), pp. 225–231.
- Fouke B. W. (2001) Depositional Facies and Aqueous-Solid Geochemistry of Travertine-Depositing Hot Springs (Angel Terrace, Mammoth Hot Springs, Yellowstone National Park, U.S.A.): Reply. *Journal of Sedimentary Research* **71** (3), pp. 497–500. DOI: 10.1306/2DC40959-0E47-11D7-8643000102C1865D.

- Fretzdorff S., Livermore R. A., Devey C. W., Leat P. T., Stoffers P. (2002) Petrogenesis of the Back-arc East Scotia Ridge, South Atlantic Ocean. *Journal of Petrology* **43** (8), pp. 1435–1467. DOI: 10.1093/petrology/43.8.1435.
- Gaillard F., Scaillet B. (2014) A theoretical framework for volcanic degassing chemistry in a comparative planetology perspective and implications for planetary atmospheres. *Earth and Planetary Science Letters* **403**, pp. 307–316. DOI: 10.1016/j.epsl.2014.07.009.
- Gamo T., Okamura K., Charlou J.-L., Urabe T., Auzende J.-M. et al. (1997) Acidic and sulfate-rich hydrothermal fluids from the Manus back-arc basin, Papua New Guinea. *Geology* **25** (2), pp. 139–142. DOI: 10.1130/0091-7613(1997)025<0139:AASRHF>2.3.CO;2.
- Gena K. R., Chiba H., Mizuta T., Matsubaya O. (2006) Hydrogen, Oxygen and Sulfur Isotope Studies of Seafloor Hydrothermal System at the Desmos Caldera, Manus Back-arc Basin, Papua New Guinea: An Analogue of Terrestrial Acid Hot Crater-lake. *Resource Geology* **56** (2), pp. 183–190. DOI: 10.1111/j.1751-3928.2006.tb00278.x.
- Georgieva M. N., Wiklund H., Bell J. B., Eilertsen M. H., Mills R. A. et al. (2015) A chemosynthetic weed: the tubeworm *Sclerolinum contortum* is a bipolar, cosmopolitan species. *BMC Evol Biol* **15** (1), pp. 280. DOI: 10.1186/s12862-015-0559-y.
- German C. R., Livermore R. A., Baker E. T., Bruguier N. I., Connelly D. P. et al. (2000) Hydrothermal plumes above the East Scotia Ridge: an isolated high-latitude back-arc spreading centre. *Earth and Planetary Science Letters* **184** (1), pp. 241–250. DOI: 10.1016/S0012-821X(00)00319-8.
- German C. R., Seyfried W. E. (2014) Hydrothermal Processes. In: Heinrich D. Holland und Karl K. Turekian (Hg.): *Treatise on geochemistry*. Oxford, UK, San Diego, CA, USA: Elsevier Pergamon, pp. 191–233. DOI: 10.1016/B978-0-08-095975-7.00607-0.
- Graham U. M., Bluth G. J., Ohmoto H. (1988) Sulfide-sulfate chimneys on the East Pacific Rise, 11 degrees and 13 degrees N latitudes; Part I, Mineralogy and paragenesis. *The Canadian Mineralogist* **26** (3), pp. 487–504.
- Hannington M. D., Jonasson I. R., Herzig P. M., Petersen S. (1995) Physical and Chemical Processes of Seafloor Mineralization at Mid-Ocean Ridges. In: Susan E. Humphris, Robert A. Zierenberg, Lauren S. Mullineaux und Richard E. Thomson (Hg.): *Seafloor Hydrothermal Systems: Physical, Chemical, Biological, and Geological Interactions*. Washington, D. C.: American Geophysical Union (Geophysical monograph series), pp. 115–157. DOI: 10.1029/GM091p0115.
- Hannington M. D., Ronde C. D. J. de, Petersen S. (2005) Sea-floor tectonics and submarine hydrothermal systems. In: J. W. Hedenquist, J. F. H. Thompson, R. J. Goldfarb und J. P.

- Richards (Hg.): Economic Geology 100th Anniversary Volume. Littelton, Colorado, USA: Society of Economic Geologists, pp. 111–141. <http://eprints.uni-kiel.de/6271/>.
- Hawkes J. A., Connelly D. P., Rijkenberg M. J. A., Achterberg E. P. (2014) The importance of shallow hydrothermal island arc systems in ocean biogeochemistry. *Geophys. Res. Lett.* **41** (3), pp. 942–947. DOI: 10.1002/2013GL058817.
- Hayashi K., Ohmoto H. (1991) Solubility of gold in NaCl-and H<sub>2</sub>S-bearing aqueous solutions at 250–350°C. *Geochimica et Cosmochimica Acta* **55** (8), pp. 2111–2126. DOI: 10.1016/0016-7037(91)90091-I.
- Haymon R., Baker E., Resing J., White S., McDonald K. (2007) Hunting for Hydrothermal Vents Along the Galápagos Spreading Center. *Oceanog.* **20** (4), pp. 100–107. DOI: 10.5670/oceanog.2007.10.
- Haymon R. M. (1983) Growth history of hydrothermal black smoker chimneys. *Nature* **301** (5902), pp. 695–698. DOI: 10.1038/301695a0.
- Hedenquist J. W., Arribas R. A., Gonzalez-Urien E. (2000) Exploration for Epithermal Gold Deposits. *Society of Economic Geologists* **13**, pp. 245–277. DOI: 10.5382/Rev.13.07.
- Hedenquist J. W., Taguchi S., Shinohara H. (2018) Features of Large Magmatic-Hydrothermal Systems in Japan: Characteristics Similar to the Tops of Porphyry Copper Deposits. *Resource Geology* **68** (2), pp. 164–180. DOI: 10.1111/rge.12159.
- Hein J. R., Mizell K. (2013) Hydrothermal systems and mineralization of volcanic arcs: Comparison of West Pacific and Mediterranean arcs, pp. 216–225.
- Helgeson H. C. (1969) Thermodynamics of hydrothermal systems at elevated temperatures and pressures. *American Journal of Science* **267** (7), pp. 729–804. DOI: 10.2475/ajs.267.7.729.
- Hepburn L. E. (2015) *Hydrothermal sediment geochemistry south of the Antarctic Polar Front*. Doctoral Thesis., 484 pp.
- Herzig P. M., Hannington M. D., Arribas Jr. A. (1998) Sulfur isotopic composition of hydrothermal precipitates from the Lau back-arc: implications for magmatic contributions to seafloor hydrothermal systems. *Mineral. Deposita* **33** (3), pp. 226–237. DOI: 10.1007/s001260050143.
- Hessler R. R., Kaharl V. A. (1995) The Deep-Sea Hydrothermal Vent Community: An Overview. *Washington DC American Geophysical Union Geophysical Monograph Series* **91**, pp. 72–84. DOI: 10.1029/GM091p0072.

- Holdgate M. W., Baker P. E. (1979) *The South Sandwich Islands: I. General description*. Cambridge. British Antarctic Survey,
- Humphris S. E., Tivey M. K. (2000) A synthesis of geological and geochemical investigations of the TAG hydrothermal field. Insights into fluid-flow and mixing processes in a hydrothermal system. *Special Papers-Geological Society of America*, pp. 213–236.
- Humphris S. E., Tivey M. K., Tivey M. A. (2015) The Trans-Atlantic Geotraverse hydrothermal field: A hydrothermal system on an active detachment fault. *Deep Sea Research Part II: Topical Studies in Oceanography* **121**, pp. 8–16. DOI: 10.1016/j.dsr2.2015.02.015.
- Iwasaki I., Ozawa T., Yoshida M., Katsura T., Iwasaki B., Kamada M. (1963) Nature of volcanic gases and volcanic eruption. *Bull Volcanol* **26** (1), pp. 73–81. DOI: 10.1007/BF02597276.
- James R. H., Green D. R. H., Stock M. J., Alker B. J., Banerjee N. R. et al. (2014) Composition of hydrothermal fluids and mineralogy of associated chimney material on the East Scotia Ridge back-arc spreading centre. *Geochimica et Cosmochimica Acta* **139**, pp. 47–71. DOI: 10.1016/j.gca.2014.04.024.
- Johnson J. W., Oelkers E. H., Helgeson H. C. (1992) SUPCRT92: A software package for calculating the standard molal thermodynamic properties of minerals, gases, aqueous species, and reactions from 1 to 5000 bar and 0 to 1000°C. *Computers & Geosciences* **18** (7), pp. 899–947. DOI: 10.1016/0098-3004(92)90029-Q.
- Kim J., Lee K.-Y., Kim J.-H. (2011) Metal-bearing molten sulfur collected from a submarine volcano: Implications for vapor transport of metals in seafloor hydrothermal systems. *Geological Society of America* **39** (4), pp. 351–354. DOI: 10.1130/G31665.1.
- Kim J., SON S.-K., SON J.-W., KIM K.-H., SHIM W. J. et al. (2009) Venting sites along the Fonualei and Northeast Lau Spreading Centers and evidence of hydrothermal activity at an off-axis caldera in the northeastern Lau Basin. *Geochem. J.* **43** (1), pp. 1–13. DOI: 10.2343/geochemj.0.0164.
- Kleine B. I., Gunnarsson-Robin J., Kamunya K. M., Ono S., Stefánsson A. (2021) Source controls on sulfur abundance and isotope fractionation in hydrothermal fluids in the Olkaria geothermal field, Kenya. *Chemical Geology* **582**, pp. 120446. DOI: 10.1016/j.chemgeo.2021.120446.
- Kleint C., Bach W., Diehl A., Fröhberg N., Garbe-Schönberg D. et al. (2019) Geochemical characterization of highly diverse hydrothermal fluids from volcanic vent systems of the Kermadec intraoceanic arc. *Chemical Geology* **528**, pp. 119289. DOI: 10.1016/j.chemgeo.2019.119289.

- Klose L., Kleint C., Bach W., Diehl A., Wilckens F. et al. (2022) Hydrothermal activity and associated subsurface processes at Niuatahi rear-arc volcano, North East Lau Basin, SW Pacific: Implications from trace elements and stable isotope systematics in vent fluids. *Geochimica et Cosmochimica Acta* ,
- Kürzinger V. (2019) Determination and Differentiation of the Hydrothermal Precipitates of Panarea, Italy. *FOG - Freiberg Online Geoscience* **54**, pp. 89.
- Kürzinger V., Diehl A., Pereira S. I., Strauss H., Bohrmann G., Bach W. (2022) Sulfur formation associated with coexisting sulfide minerals in the Kemp Caldera hydrothermal system, Scotia Sea. *Chemical Geology* **606**, pp. 1–20. DOI: 10.1016/j.chemgeo.2022.120927.
- Kusakabe M., Komoda Y., Takano B., Abiko T. (2000) Sulfur isotopic effects in the disproportionation reaction of sulfur dioxide in hydrothermal fluids: implications for the  $\delta^{34}\text{S}$  variations of dissolved bisulfate and elemental sulfur from active crater lakes. *Geology* **97** (1-4), pp. 287–307. DOI: 10.1016/S0377-0273(99)00161-4.
- Labidi J., Cartigny P., Birck J. L., Assayag N., Bourrand J. J. (2012) Determination of multiple sulfur isotopes in glasses: A reappraisal of the MORB  $\delta^{34}\text{S}$ . *Chemical Geology* **334**, pp. 189–198. DOI: 10.1016/j.chemgeo.2012.10.028.
- Larter R. D. (2009) The expedition JR224 of the RRS James Clark Ross in 2009. Chemosynthetically-driven Ecosystems South of the Polar Front consortium programme; Multidisciplinary exploration to constrain hydrothermal vent and cold seep locations in the Scotia Sea.
- Larter R. D., King E. C., Leat P. T., Reading A. M., Smellie J. L., Smythe D. K. (1998) South sandwich slices reveal much about arc structure, geodynamics, and composition. *Eos Trans. AGU* **79** (24), pp. 281. DOI: 10.1029/98EO00207.
- Larter R. D., Vanneste L. E., Morris P., Smythe D. K. (2003) Structure and tectonic evolution of the South Sandwich arc. *Geological Society, London, Special Publications* **219** (1), pp. 255–284. DOI: 10.1144/GSL.SP.2003.219.01.13.
- Leat P. T., Day S. J., Tate A. J., Martin T. J., Owen M. J., Tappin D. R. (2013) Volcanic evolution of the South Sandwich volcanic arc, South Atlantic, from multibeam bathymetry. *Journal of Volcanology and Geothermal Research* **265**, pp. 60–77. DOI: 10.1016/j.jvolgeores.2013.08.013.
- Leat P. T., Fretwell P. T., Tate A. J., Larter R. D., Martin T. J. et al. (2016) Bathymetry and geological setting of the South Sandwich Islands volcanic arc. *Antarctic Science* **28** (4), pp. 293–303. DOI: 10.1017/S0954102016000043.

- Leat P. T., Larter R. D. (2003) Intra-oceanic subduction systems: introduction. *Geological Society, London, Special Publications* **219** (1), pp. 1–17. DOI: 10.1144/GSL.SP.2003.219.01.01.
- Leat P. T., Livermore R. A., Millar I. L., Pearce J. A. (2000) Magma Supply in Back-arc Spreading Centre Segment E2, East Scotia Ridge. *Journal of Petrology* **41** (6), pp. 845–866. DOI: 10.1093/petrology/41.6.845.
- Leat P. T., Pearce J. A., Barker P. F., Millar I. L., Barry T. L., Larter R. D. (2004) Magma genesis and mantle flow at a subducting slab edge: the South Sandwich arc-basin system. *Earth and Planetary Science Letters* **227** (1-2), pp. 17–35. DOI: 10.1016/j.epsl.2004.08.016.
- Leat P. T., Smellie J. L., Millar I. L., Larter R. D. (2003) Magmatism in the South Sandwich arc. *Geological Society, London, Special Publications* **219** (1), pp. 285–313. DOI: 10.1144/GSL.SP.2003.219.01.14.
- Leat P. T., Tate A. J., Tappin D. R., Day S. J., Owen M. J. (2010) Growth and mass wasting of volcanic centers in the northern South Sandwich arc, South Atlantic, revealed by new multibeam mapping. *Marine Geology* **275** (1-4), pp. 110–126. DOI: 10.1016/j.margeo.2010.05.001.
- LeBas M. J., Maitre R. W. L., Streckeisen A., Zanettin B. (1986) A Chemical Classification of Volcanic Rocks Based on the Total Alkali-Silica Diagram. *J Petrology* **27** (3), pp. 745–750. DOI: 10.1093/petrology/27.3.745.
- Lee C.-T. A., Tang M. (2020) How to make porphyry copper deposits. *Earth and Planetary Science Letters* **529**, pp. 115868. DOI: 10.1016/j.epsl.2019.115868.
- Li K., Brugger J., Pring A. (2018) Exsolution of chalcopyrite from bornite-digenite solid solution: an example of a fluid-driven back-replacement reaction. *Miner Deposita* **53** (7), pp. 903–908. DOI: 10.1007/s00126-018-0820-6.
- Linse K., Copley J. T., Connelly D. P., Larter R. D., Pearce D. A. et al. (2019) Fauna of the Kemp Caldera and its upper bathyal hydrothermal vents (South Sandwich Arc, Antarctica). *R. Soc. open sci.* **6** (11), pp. 1–26. DOI: 10.1098/rsos.191501.
- Lipman P. W. (1997) Subsidence of ash-flow calderas: relation to caldera size and magma-chamber geometry. *Bull Volcanol* **59** (3), pp. 198–218. DOI: 10.1007/s004450050186.
- Livermore R. (2003) Back-arc spreading and mantle flow in the East Scotia Sea. *Geological Society, London, Special Publications* **219** (1), pp. 315–331. DOI: 10.1144/GSL.SP.2003.219.01.15.
- Lusk J., Bray M. D. (2002) Phase relations and the electrochemical determination of sulfur fugacity for selected reactions in the Cu–Fe–S and Fe–S systems at 1 bar and temperatures

- between 185 and 460 °C. *Chemical Geology* **192** (3-4), pp. 227–248. DOI: 10.1016/S0009-2541(02)00194-8.
- Mandon C. L., Seward T. M., Christenson B. W. (2020) Volatile transport of metals and the Cu budget of the active White Island magmatic-hydrothermal system, New Zealand. *Geology* **398**, pp. 106905. DOI: 10.1016/j.jvolgeores.2020.106905.
- Marcon Y. (2019) NavCleaner (OFOS Edition) for processing raw Posidonia USBL datagrams. DOI: 10.1594/PANGAEA.905243.
- Markússon S. H., Stefánsson A. (2011) Geothermal surface alteration of basalts, Krýsuvík Iceland—Alteration mineralogy, water chemistry and the effects of acid supply on the alteration process. *Geology* **206** (1-2), pp. 46–59. DOI: 10.1016/j.jvolgeores.2011.05.007.
- McDermott J. M., Ono S., Tivey M. K., Seewald J. S., Shanks W. C., Solow A. R. (2015) Identification of sulfur sources and isotopic equilibria in submarine hot-springs using multiple sulfur isotopes. *Geochimica et Cosmochimica Acta* **160**, pp. 169–187. DOI: 10.1016/j.gca.2015.02.016.
- McDermott J. M., Sylva S. P., Ono S., German C. R., Seewald J. S. (2018) Geochemistry of fluids from Earth's deepest ridge-crest hot-springs: Piccard hydrothermal field, Mid-Cayman Rise. *Geochimica et Cosmochimica Acta* **228**, pp. 95–118. DOI: 10.1016/j.gca.2018.01.021.
- Neukirchen F., Ries G. (2014) Hydrothermale Lagerstätten. In: Florian Neukirchen und Gunnar Ries (Hg.): Die Welt der Rohstoffe. Berlin, Heidelberg: Springer Berlin Heidelberg, pp. 143–227. DOI: 10.1007/978-3-642-37739-6\_4.
- Newton I. L. G., Woyke T., Auchtung T. A., Dilly G. F., Dutton R. J. et al. (2007) The *Calyptogenia magnifica* chemoautotrophic symbiont genome. *Science* **315** (5814), pp. 998–1000. DOI: 10.1126/science.1138438.
- Nielson D. L., Hulen J. B. (1984) Internal geology and evolution of the Redondo Dome, Valles Caldera, New Mexico. *J. Geophys. Res.* **89** (B10), pp. 8695. DOI: 10.1029/JB089iB10p08695.
- Nilsson K., Peach C. L. (1993) Sulfur speciation, oxidation state, and sulfur concentration in backarc magmas. *Geochimica et Cosmochimica Acta* **57** (15), pp. 3807–3813. DOI: 10.1016/0016-7037(93)90158-S.
- Oberlander O. P. (2022) Woods Hole Oceanographic Institution - The Discovery of Hydrothermal Vents, zuletzt geprüft am 9/11/2022.

- Ohmoto H., Lasaga A. C. (1982) Kinetics of reactions between aqueous sulfates and sulfides in hydrothermal systems. *Geochimica et Cosmochimica Acta* **46** (10), pp. 1727–1745. DOI: 10.1016/0016-7037(82)90113-2.
- Ohmoto H., Rye R. O. (1979) Isotopes of sulfur and carbon. In: Hubert L. Barnes (Hg.): *Geochemistry of Hydrothermal Ore Deposits*. 2. Edition: John Wiley & Sons, Inc., pp. 509–567.
- Ono S., Keller N. S., Rouxel O., Alt J. C. (2012) Sulfur-33 constraints on the origin of secondary pyrite in altered oceanic basement. *Geochimica et Cosmochimica Acta* **87**, pp. 323–340. DOI: 10.1016/j.gca.2012.04.016.
- Park J.-W., Campbell I. H., Chiaradia M., Hao H., Lee C.-T. (2021) Crustal magmatic controls on the formation of porphyry copper deposits. *Nat Rev Earth Environ* **2** (8), pp. 542–557. DOI: 10.1038/s43017-021-00182-8.
- Pearce J. A., Barker P. F., Edwards S. J., Parkinson I. J., Leat P. T. (2000) Geochemistry and tectonic significance of peridotites from the South Sandwich arc-basin system, South Atlantic. *Contributions to Mineralogy and Petrology* **139** (1), pp. 36–53. DOI: 10.1007/s004100050572.
- Pentecost A., Jones B., Renaut R. W. (2003) What is a hot spring? *Can. J. Earth Sci.* **40** (11), pp. 1443–1446. DOI: 10.1139/e03-083.
- Pereira S. I., Diehl A., McDermott J. M., Pape T., Klose L. et al. (2022) Geochemistry of hydrothermal fluids from the E2-segment of the East Scotia Ridge: Magmatic input, reaction zone processes, fluid mixing regimes and bioenergetic landscapes. *Frontiers in Marine Science*, pp. 696. DOI: 10.3389/fmars.2022.765648.
- Peters C., Strauss H., Haase K., Bach W., Ronde C. E. de et al. (2021) SO<sub>2</sub> disproportionation impacting hydrothermal sulfur cycling: Insights from multiple sulfur isotopes for hydrothermal fluids from the Tonga-Kermadec intraoceanic arc and the NE Lau Basin. *Chemical Geology* **586**, pp. 120586. DOI: 10.1016/j.chemgeo.2021.120586.
- Pirajno F. (2020) Subaerial hot springs and near-surface hydrothermal mineral systems past and present, and possible extraterrestrial analogues. *Geoscience Frontiers* **11** (5), pp. 1549–1569. DOI: 10.1016/j.gsf.2020.04.001.
- Polz M. F., Cavanaugh C. M. (1996) The ecology of the ectosymbiosis at a Mid-Atlantic Ridge hydrothermal vent site. In: W. Morawetz und H. Winkler (Hg.): *Deep Sea and extreme shallow-water habitats: affinities and adaptations*, Bd. 11 (11), pp. 337–352. DOI: 10.1016/S0065-2881(08)60016-4.

- Present T. M., Adkins J. F., Fischer W. W. (2020) Variability in Sulfur Isotope Records of Phanerozoic Seawater Sulfate. *Geophysical Research Letters* **47** (18), pp. 1-29. DOI: 10.1029/2020GL088766.
- Purser A., Marcon Y., Dreutter S., Hoge U., Sablotny B. et al. (2019) Ocean Floor Observation and Bathymetry System (OFOBS): A New Towed Camera/Sonar System for Deep-Sea Habitat Surveys. *IEEE J. Oceanic Eng.* **44** (1), pp. 87–99. DOI: 10.1109/joe.2018.2794095.
- Reeves E. P., Seewald J. S., Saccocia P., Bach W., Craddock P. R. et al. (2011) Geochemistry of hydrothermal fluids from the PACMANUS, Northeast Pual and Vienna Woods hydrothermal fields, Manus Basin, Papua New Guinea. *Geochimica et Cosmochimica Acta* **75** (4), pp. 1088–1123. DOI: 10.1016/j.gca.2010.11.008.
- Reid W. D. K., Sweeting C. J., Wigham B. D., Zwirgmaier K., Hawkes J. A. et al. (2013) Spatial differences in East scotia ridge hydrothermal vent food webs: influences of chemistry, microbiology and predation on trophodynamics. *PLoS one* **8** (6), pp. 1-11. DOI: 10.1371/journal.pone.0065553.
- Resing J. A., Lebon G., Baker E. T., Lupton J. E., Embley R. W. et al. (2007) Venting of Acid-Sulfate Fluids in a High-Sulfidation Setting at NW Rota-1 Submarine Volcano on the Mariana Arc. *Economic Geology* **102** (6), pp. 1047–1061. DOI: 10.2113/gsecongeo.102.6.1047.
- Resing J. A., Lupton J. E., Feely R. A., Lilley M. D. (2004) CO<sub>2</sub> and <sup>3</sup>He in hydrothermal plumes: implications for mid-ocean ridge CO<sub>2</sub> flux. *Earth and Planetary Science Letters* **226** (3-4), pp. 449–464. DOI: 10.1016/j.epsl.2004.07.028.
- Riley T. R., Carter A., Leat P. T., Burton-Johnson A., Bastias J. et al. (2019) Geochronology and geochemistry of the northern Scotia Sea: A revised interpretation of the North and West Scotia ridge junction. *Earth and Planetary Science Letters* **518**, pp. 136–147. DOI: 10.1016/j.epsl.2019.04.031.
- Rinehart J. S. (1980) Geysers of the World. In: John S. Rinehart (Hg.): Geysers and Geothermal Energy. New York, NY: Springer New York, pp. 1–23. DOI: 10.1007/978-1-4612-6084-4\_1.
- Robb L. (2005) *Introduction to Ore-Forming Processes*. Cornwell (UK). Blackwell Science Ltd, 386 pp.
- Rogers A. D. (2010) The expedition JC42 of the RRS James Cook in 2010. Chemosynthetic Ecosystems of the Southern Ocean (CHESSO).

- Rogers A. D., Tyler P. A., Connelly D. P., Copley J. T., James R. et al. (2012) The discovery of new deep-sea hydrothermal vent communities in the southern ocean and implications for biogeography. *PLoS biology* **10** (1), pp. e1001234. DOI: 10.1371/journal.pbio.1001234.
- Rosli N. A., Anuar M. N. A., Mansor M. H., Abdul Rahim N. S. I., Arifin M. H. (2022) What Makes A Hot Spring, Hot? *WG* **48** (1), pp. 30–35. DOI: 10.7186/wg481202204.
- Schoen R., Rye R. O. (1970) Sulfur isotope distribution in solfataras, yellowstone national park. *Science* **170** (3962), pp. 1082–1084. DOI: 10.1126/science.170.3962.1082.
- Schoonen M., Barnes H. (1991) Mechanisms of pyrite and marcasite formation from solution: III. Hydrothermal processes. *Geochimica et Cosmochimica Acta* **55** (12), pp. 3491–3504. DOI: 10.1016/0016-7037(91)90050-F.
- Schoonen M. A. (2004) Mechanisms of sedimentary pyrite formation. *Geological Society of America Special Paper* **379**, pp. 117–134. DOI: 10.1130/0-8137-2379-5.117.
- Scott S. D., Chase R. L., Hannington M. D., Michael P. J., McConachy T. F., Shea G. T. (1995) Sulphide deposits, tectonics and petrogenesis of Southern Explorer Ridge, northeast Pacific Ocean. In: Susan E. Humphris, Robert A. Zierenberg, Lauren S. Mullineaux und Richard E. Thomson (Hg.): *Seafloor Hydrothermal Systems: Physical, Chemical, Biological, and Geological Interactions*. Washington, D. C.: American Geophysical Union (Geophysical monograph series), pp. 719–733. <https://pascal-francis.inist.fr/vibad/index.php?action=getrecorddetail&idt=19716484>.
- Seewald J. S., Doherty K. W., Hammar T. R., Liberatore S. P. (2001) A new gas-tight isobaric sampler for hydrothermal fluids. *Deep Sea Research Part I: Oceanographic Research Papers* **49** (1), pp. 189–196. DOI: 10.1016/S0967-0637(01)00046-2.
- Seewald J. S., Reeves E. P., Bach W., Saccocia P. J., Craddock P. R. et al. (2015) Submarine venting of magmatic volatiles in the Eastern Manus Basin, Papua New Guinea. *Geochimica et Cosmochimica Acta* **163**, pp. 178–199. DOI: 10.1016/j.gca.2015.04.023.
- Seewald J. S., Reeves E. P., Bach W., Saccocia P. J., Craddock P. R. et al. (2019) Geochemistry of hot-springs at the SuSu Knolls hydrothermal field, Eastern Manus Basin: Advanced argillic alteration and vent fluid acidity. *Geochimica et Cosmochimica Acta* **255**, pp. 25–48. DOI: 10.1016/j.gca.2019.03.034.
- Seyfried W. E., Janecky D. R., Berndt M. E. (1987) Rocking autoclaves for hydrothermal experiments II. The flexible reaction-cell system. In: *Hydrothermal Experimental Techniques*: Wiley-Interscience Publications, pp. 216–239.
- Shanks W., Bischoff J. L., Rosenbauer R. J. (1981) Seawater sulfate reduction and sulfur isotope fractionation in basaltic systems: Interaction of seawater with fayalite and magnetite

- at 200–350°C. *Geochimica et Cosmochimica Acta* **45** (11), pp. 1977–1995. DOI: 10.1016/0016-7037(81)90054-5.
- Shanks W. C., Böhlke J. K., Seal R. R. (1995) Stable isotopes in mid-ocean ridge hydrothermal systems: Interactions between fluids, minerals, and organisms. In: Susan E. Humphris, Robert A. Zierenberg, Lauren S. Mullineaux und Richard E. Thomson (Hg.): *Seafloor Hydrothermal Systems: Physical, Chemical, Biological, and Geological Interactions*. Washington, D. C.: American Geophysical Union (Geophysical monograph series), pp. 194–221.
- Sillitoe R. H. (1973) The tops and bottoms of porphyry copper deposits. *Economic Geology* **68** (6), pp. 799–815. DOI: 10.2113/gsecongeo.68.6.799.
- Smith R. L., Bailey R. A. (1968) Resurgent Cauldrons. In: *Studies in Volcanology*, Bd. 116: Geological Society of America (Geological Society of America Memoirs, 116), pp. 613–662. DOI: 10.1130/MEM116-p613.
- Spieß F. N., Macdonald K. C., Atwater T., Ballard R., Carranza A. et al. (1980) East pacific rise: hot springs and geophysical experiments. *Science* **207** (4438), pp. 1421–1433. DOI: 10.1126/science.207.4438.1421.
- Stefánsson A., Keller N. S., Robin J. G., Ono S. (2015) Multiple sulfur isotope systematics of Icelandic geothermal fluids and the source and reactions of sulfur in volcanic geothermal systems at divergent plate boundaries. *Geochimica et Cosmochimica Acta* **165**, pp. 307–323. DOI: 10.1016/j.gca.2015.05.045.
- Stucker V. K., Walker S. L., Ronde C. E. J. de, Caratori Tontini F., Tsuchida S. (2017) Hydrothermal Venting at Hinepua Submarine Volcano, Kermadec Arc: Understanding Magmatic-Hydrothermal Fluid Chemistry. *Geochem. Geophys. Geosyst.* **18** (10), pp. 3646–3661. DOI: 10.1002/2016GC006713.
- Thatje S., Marsh L., Roterman C. N., Mavrogordato M. N., Linse K. (2015) Adaptations to Hydrothermal Vent Life in *Kiwa tyleri*, a New Species of Yeti Crab from the East Scotia Ridge, Antarctica. *PloS one* **10** (6), pp. e0127621. DOI: 10.1371/journal.pone.0127621.
- Thomas C., Livermore R., Pollitz F. (2003) Motion of the Scotia Sea plates. *Geophys J Int* **155** (3), pp. 789–804. DOI: 10.1111/j.1365-246X.2003.02069.x.
- Thompson G., Humphris S. E., Schroeder B., Sulanowska M., Rona P. A. (1988) Active vents and massive sulfides at 26°N (TAG) and 23°N (Snakepit) on the Mid-Atlantic Ridge. *Canadian Mineralogist* **26**, pp. 697–711.
- Tivey M. (2007) Generation of Seafloor Hydrothermal Vent Fluids and Associated Mineral Deposits. *Oceanog.* **20** (1), pp. 50–65. DOI: 10.5670/oceanog.2007.80.

- Tivey M. K. (1995) Modeling Chimney Growth and Associated Fluid Flow at Seafloor Hydrothermal Vent Sites. *Washington DC American Geophysical Union Geophysical Monograph Series* **91**, pp. 158–177. DOI: 10.1029/GM091p0158.
- Trewin N. H., Fayers S. R. (2005) SEDIMENTARY ROCKS | Chert. In: Richard C. Selley (Hg.): *Encyclopedia of geology*. Amsterdam, Heidelberg, S.I.: Elsevier; ScienceDirect Online-Anbieter (ScienceDirect), pp. 51–62. DOI: 10.1016/B0-12-369396-9/00315-4.
- Tun M. M., Warmada I. W., Idrus A., Harijoko A., Verdiansyah O., Watanabe K. (2015) High sulfidation epithermal mineralization and ore mineral assemblages of Cijulang Prospect, West Java, Indonesia. *J. Appl. Geol.* **6** (1). DOI: 10.22146/jag.7215.
- Tyler P. A. (2011) The expedition JC55 of the RRS James Cook in 2011. Bransfield Strait, the East Scotia Ridge and the Kemp Seamount Calderas; Cruise 3 of the NERC Consortium Grant 'Chemosynthetically-driven ecosystems in the Southern Ocean: Ecology and Biogeography' (ChEsSo).
- Vermeesch P., Pease V. (2021) A genetic classification of the tholeiitic and calc-alkaline magma series. *Geochemical Perspectives Letters* **19**, pp. 1–6.
- von Damm K. L. (1990) Seafloor hydrothermal activity: Black smoker chemistry and chimneys. *Annu. Rev. Earth Planet. Sci.* **18** (1), pp. 173–204. DOI: 10.1146/annurev.ea.18.050190.001133.
- von Damm K. L., Edmond J. M., Grant B., Measures C. I. (1985) Chemistry of submarine hydrothermal solutions at 21°N, East Pacific Rise. *Geochimica et Cosmochimica Acta* **49**, pp. 2197–2220. DOI: 10.1016/0016-7037(85)90222-4.
- Walker S. L., Baker E. T., Resing J. A., Nakamura K., McLain P. D. (2007) A New Tool for Detecting Hydrothermal Plumes: an ORP Sensor for the PMEL MAPR. *AGU Fall Meeting Abstracts* **2007**, pp. V21D-0753.
- Wallace P. J. (2005) Volatiles in subduction zone magmas: concentrations and fluxes based on melt inclusion and volcanic gas data. *Geology* **140** (1-3), pp. 217–240. DOI: 10.1016/j.jvolgeores.2004.07.023.
- Wallace P. J., Plank T., Edmonds M., Hauri E. H. (2015) Volatiles in Magmas. In: Haraldur Sigurdsson und B. F. Houghton (Hg.): *Encyclopedia of volcanoes*. Second edition. Amsterdam, Boston: Elsevier/AP, Academic Press is an imprint of Elsevier, pp. 163–183. DOI: 10.1016/B978-0-12-385938-9.00007-9.
- Wilckens F. K., Reeves E. P., Bach W., Seewald J. S., Kasemann S. A. (2019) Application of B, Mg, Li, and Sr Isotopes in Acid-Sulfate Vent Fluids and Volcanic Rocks as Tracers for

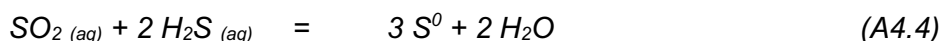
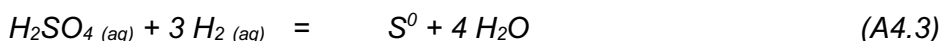
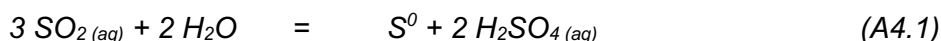
- 
- Fluid-Rock Interaction in Back-Arc Hydrothermal Systems. *Geochem. Geophys. Geosyst.* **20** (12), pp. 5849–5866. DOI: 10.1029/2019GC008694.
- Wu S.-J., Cai M.-J., Yang C.-J., Li K.-W. (2016) A new flexible titanium foil cell for hydrothermal experiments and fluid sampling. *The Review of scientific instruments* **87** (9), pp. 1–6. DOI: 10.1063/1.4963700.
- Zeng Z., Liu C., Chen C. A., Yin X., Chen D. et al. (2007) Origin of a native sulfur chimney in the Kueishantao hydrothermal field, offshore northeast Taiwan. *SCI CHINA SER D* **50** (11), pp. 1746–1753. DOI: 10.1007/s11430-007-0092-y.
- Zhao J., Brugger J., Chen G., Ngothai Y., Pring A. (2014a) Experimental study of the formation of chalcopyrite and bornite via the sulfidation of hematite: Mineral replacements with a large volume increase. *American Mineralogist* **99** (2-3), pp. 343–354. DOI: 10.2138/am.2014.4628.
- Zhao J., Brugger J., Ngothai Y., Pring A. (2014b) The replacement of chalcopyrite by bornite under hydrothermal conditions. *American Mineralogist* **99** (11-12), pp. 2389–2397. DOI: 10.2138/am-2014-4825.

## APPENDIX

### Additional information for manuscript II – Sulfur formation associated with coexisting sulfide minerals in the Kemp Caldera hydrothermal system, Scotia Sea

#### Rayleigh fractionation model

In these notes, we explain the Rayleigh fractionation models used to calculate sulfur isotope values of elemental sulfur ( $S^0$  or S) expected from  $SO_2$  disproportionation (reaction A4.1), oxidation of  $H_2S$  (reaction A4.2), sulfate reduction (reaction A4.3), and  $SO_2$ – $H_2S$  synproportionation (reaction A4.4), respectively.



Equilibrium sulfur isotope fractionation factors ( $\alpha$ ) as a function of temperature are listed in Table A4.1.

**Table A4.1**

Equilibrium isotopic fractionation factors between sulfur compounds.

Reaction i–j	$10^3 \ln \alpha_{i-j} = A \times 10^6/T^2 + B \times 10^3/T + C$			T range [°C]	References
	A	B	C		
$SO_{4(aq)}-H_2S_{(aq)}$	3.42	10.17	-7.34	200–400	Ohmoto and Lasaga (1982), Kleine et al. (2021)
$SO_{2(aq)}-H_2S_{(aq)}$	-1.63	-5.10	3.93	350–1050	Kleine et al. (2021)
$H_2S_{(aq)}-S$	-0.16	--	--	200–400	Ohmoto and Rye (1979)
$SO_{4(aq)}-S$	6.21	--	3.62	200–330	Kusakabe et al. (2000)

For the calculation of the equation, T is in Kelvin. The values for the reverse reaction are obtained with  $\delta^{34}S_{X-Y} = 1 + 1 - \alpha$ ;  $\alpha$  as fractionation factor of the respective reaction.

The equation  $10^3 \ln \alpha_{i-j} = A + B/T + C/T^2 + D/T^3$  can also be found in the literature (cf. Kleine et al., 2021). However, the parameter values for this equation are different from those mentioned in Table A4.1, so the formula must either be adapted or calculated with the corresponding values.

In the literature, values are not found for the pairs  $SO_{2(aq)}-S$  and  $SO_{4(aq)}-SO_{2(aq)}$ . These isotopic fractionation factors can be derived by combining the isotope fractionation between  $SO_{2(aq)}-H_2S_{(aq)}$  and  $S-H_2S_{(aq)}$  as well as  $SO_{4(aq)}-H_2S_{(aq)}$  and  $SO_{2(aq)}-H_2S_{(aq)}$ , respectively.

Closed-system Rayleigh fractionation models were applied to study the effects on the sulfur isotope compositions of elemental sulfur. The resulting sulfur isotope fractionation is generally described by Ono et al. (2012), Stefánsson et al. (2015) and Kleine et al. (2021), but the

equations were modified to express instantaneous  $\delta^{34}\text{S}$  variations in  $\text{S}^0$  formed upon the abovenamed reactions. Using a closed-system Rayleigh model, sulfur isotope ratios of sulfur (and sulfate) can be expressed as follows: for  $\text{SO}_2$  disproportionation (eq. A4.5 and A4.6),

$$\delta^{34}\text{S}_{\text{SO}_4(i)} = 1000 \times \left[ \left( \frac{\delta^{34}\text{S}_{\text{SO}_2}}{1000} + 1 \right) \times \frac{1-f^{\alpha(\text{SO}_4-\text{SO}_2)}}{1-f} - 1 \right] \quad (\text{A4.5})$$

$$\delta^{34}\text{S}_{\text{S}(i)} = 1000 \times \left[ \left( \frac{\delta^{34}\text{S}_{\text{SO}_2}}{1000} + 1 \right) \times \frac{1-f^{\alpha(\text{S}-\text{SO}_2)}}{1-f} - 1 \right] \quad (\text{A4.6})$$

for  $\text{H}_2\text{S}$  oxidation (eq. A4.7),

$$\delta^{34}\text{S}_{\text{S}(i)} = 1000 \times \left[ \left( \frac{\delta^{34}\text{S}_{\text{H}_2\text{S}}}{1000} + 1 \right) \times \frac{1-f^{\alpha(\text{S}-\text{H}_2\text{S})}}{1-f} - 1 \right] \quad (\text{A4.7})$$

for  $\text{SO}_4$  reduction (eq. A4.8),

$$\delta^{34}\text{S}_{\text{S}(i)} = 1000 \times \left[ \left( \frac{\delta^{34}\text{S}_{\text{SO}_4}}{1000} + 1 \right) \times \frac{1-f^{\alpha(\text{S}-\text{SO}_4)}}{1-f} - 1 \right] \quad (\text{A4.8})$$

and for and  $\text{SO}_2$ – $\text{H}_2\text{S}$  synproportionation (eq. A4.9 and A4.10),

$$\delta^{34}\text{S}_{\text{S}(i)} = 1000 \times \left[ \left( \frac{\delta^{34}\text{S}_{\text{SO}_2}}{1000} + 1 \right) \times \frac{1-f^{\alpha(\text{S}-\text{SO}_2)}}{1-f} - 1 \right] \quad (\text{A4.9})$$

$$\delta^{34}\text{S}_{\text{S}(i)} = 1000 \times \left[ \left( \frac{\delta^{34}\text{S}_{\text{H}_2\text{S}}}{1000} + 1 \right) \times \frac{1-f^{\alpha(\text{S}-\text{H}_2\text{S})}}{1-f} - 1 \right] \quad (\text{A4.10})$$

where  $f$  is the mol fraction of the reactant(s) reduced/oxidized to  $\text{S}^0$  (and sulfate), relative to the initial reactant(s), and  $\alpha$  is the fractionation factor between  $\text{S}^0$  (or sulfate) and the reactants  $\text{SO}_2$  and/or  $\text{H}_2\text{S}$ , respectively. Equations A4.9 and A4.10 give the  $\delta^{34}\text{S}$  values of sulfur produced by  $\text{SO}_2$  reduction and  $\text{H}_2\text{S}$  oxidation, respectively. In these calculations, values of  $\delta^{34}\text{S}_{\text{SO}_2} = +7.5 \text{‰}$  and  $\delta^{34}\text{S}_{\text{H}_2\text{S}} = +4.5 \text{‰}$  were assumed considering  $\delta^{34}\text{S}$  values of +4 to +10 ‰ for arc lavas (Hannington et al., 2005) and the isotopic composition of  $\text{H}_2\text{S}$  at Great Wall (+4.6 ‰). The difference of 3 ‰ between the  $\delta^{34}\text{S}$  values of  $\text{SO}_2$  and  $\text{H}_2\text{S}$  corresponds to fumarole gas temperature of 700 °C, using fractionation coefficients from Eldridge et al. (2016).

The cumulative isotopic composition of  $\delta^{34}\text{S}_{\text{S}}$  can then be determined by simple mass balance:

$$\delta^{34}\text{S}_{\text{S}} = \frac{\sum \delta^{34}\text{S}_{\text{S}(i)} f}{a} \quad (\text{A4.11})$$

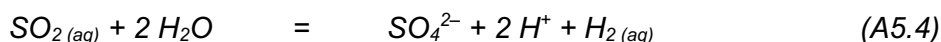
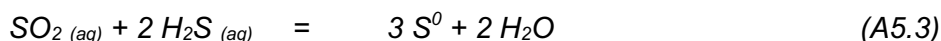
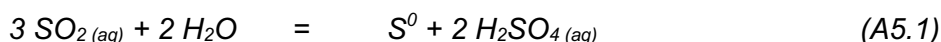
where  $f \in \{0.99, 0.98, \dots, 0.01\}$  and  $a$  is the percentage of the already reacted educt(s) or the number of  $\delta^{34}\text{S}_{\text{S}(i)}$  values added for a certain fraction value;  $a \in \{1, 2, \dots, 99\}$ . The stoichiometry of reaction A4.4 indicates that the  $\delta^{34}\text{S}$  values of the total sulfur produced by synproportionation of  $\text{SO}_2$  and  $\text{H}_2\text{S}$  is (resulting from eq. A4.9 and A4.10):

$$\delta^{34}\text{S}_{\text{S}} = \delta^{34}\text{S}(\text{A4.11})_{\text{SO}_2} + 2 \times \delta^{34}\text{S}(\text{A4.11})_{\text{H}_2\text{S}} \quad (\text{A4.12})$$

### Additional information for manuscript III – Experimental study of sulfur isotopic composition of white smoker precipitates in the Kemp Caldera (Scotia Sea)

#### Rayleigh fractionation model

Rayleigh fractionation models were used to calculate  $\delta^{34}\text{S}$  values of elemental sulfur ( $\text{S}^0$ ) expected from  $\text{SO}_2$  disproportionation (eq. A5.1),  $\text{H}_2\text{S}$  oxidation (eq. A5.2), and synproportionation of  $\text{SO}_2$  and  $\text{H}_2\text{S}$  (eq. A5.3), respectively, and  $\text{SO}_2$  oxidation for sulfate formation (A5.4).



In Table A5.1, equilibrium sulfur isotope fractionation factors ( $\alpha$ ) are listed as a function of temperature.

**Table A5.1**

Equilibrium isotopic fractionation factors between sulfur compounds (Kürzinger et al., 2022).

Reaction i-j	$10^3 \ln \alpha_{i-j} = A \times 10^6/T^2 + B \times 10^3/T + C$			T range [°C]	References
	A	B	C		
$\text{SO}_{4(aq)}-\text{H}_2\text{S}_{(aq)}$	3.42	10.17	-7.34	200–400	Ohmoto and Lasaga (1982), Kleine et al. (2021)
$\text{SO}_{2(aq)}-\text{H}_2\text{S}_{(aq)}$	-1.63	-5.10	3.93	350–1050	Kleine et al. (2021)
$\text{H}_2\text{S}_{(aq)}-\text{S}$	-0.16	--	--	200–400	Ohmoto and Rye (1979)
$\text{SO}_{4(aq)}-\text{S}$	6.21	--	3.62	200–330	Kusakabe et al. (2000)

For the calculation of the equation, T is in Kelvin. The values for the reverse reaction are obtained with  $\delta^{34}\text{S}_{X-Y} = 1 + 1 - \alpha$ ;  $\alpha$  as fractionation factor of the respective reaction.

Besides the equation shown in Table A5.1, another equation can be found in the literature:  $10^3 \ln \alpha_{i-j} = A + B/T + C/T^2 + D/T^3$  (cf. Kleine et al., 2021). Note that the parameter values for this equation differ from those listed in Table A5.1, so the equation has to be calculated using the appropriate values.

Furthermore, certain reaction pairs like  $\text{SO}_{2(aq)}-\text{S}$  and  $\text{SO}_{4(aq)}-\text{SO}_{2(aq)}$  are not found in the literature. These isotopic fractionation factors can be derived by combining the isotope fractionation between  $\text{SO}_{2(aq)}-\text{H}_2\text{S}_{(aq)}$  and  $\text{S}-\text{H}_2\text{S}_{(aq)}$  as well as  $\text{SO}_{4(aq)}-\text{H}_2\text{S}_{(aq)}$  and  $\text{SO}_{2(aq)}-\text{H}_2\text{S}_{(aq)}$ , respectively.

Closed-system Rayleigh fractionation models were applied to study the effects on the sulfur isotope compositions of elemental sulfur. The resulting sulfur isotope fractionation is generally described by Ono et al. (2012), Stefánsson et al. (2015) and Kleine et al. (2021), but the

equations were modified to express instantaneous  $\delta^{34}\text{S}$  variations in  $\text{S}^0$  formed upon the abovenamed reactions. Using a closed-system Rayleigh model, sulfur isotope ratios of sulfur (and sulfate) can be expressed as follows: for  $\text{SO}_2$  disproportionation (eq. A5.5 and A5.6),

$$\delta^{34}\text{S}_{\text{SO}_4(i)} = 1000 \times \left[ \left( \frac{\delta^{34}\text{S}_{\text{SO}_2}}{1000} + 1 \right) \times \frac{1-f^{\alpha(\text{SO}_4-\text{SO}_2)}}{1-f} - 1 \right] \quad (\text{A5.5})$$

$$\delta^{34}\text{S}_{\text{S}(i)} = 1000 \times \left[ \left( \frac{\delta^{34}\text{S}_{\text{SO}_2}}{1000} + 1 \right) \times \frac{1-f^{\alpha(\text{S}-\text{SO}_2)}}{1-f} - 1 \right] \quad (\text{A5.6})$$

for  $\text{H}_2\text{S}$  oxidation (eq. A5.7),

$$\delta^{34}\text{S}_{\text{S}(i)} = 1000 \times \left[ \left( \frac{\delta^{34}\text{S}_{\text{H}_2\text{S}}}{1000} + 1 \right) \times \frac{1-f^{\alpha(\text{S}-\text{H}_2\text{S})}}{1-f} - 1 \right] \quad (\text{A5.7})$$

for and  $\text{SO}_2$ – $\text{H}_2\text{S}$  synproportionation (eq. A5.8 and A5.9),

$$\delta^{34}\text{S}_{\text{S}(i)} = 1000 \times \left[ \left( \frac{\delta^{34}\text{S}_{\text{SO}_2}}{1000} + 1 \right) \times \frac{1-f^{\alpha(\text{S}-\text{SO}_2)}}{1-f} - 1 \right] \quad (\text{A5.8})$$

$$\delta^{34}\text{S}_{\text{S}(i)} = 1000 \times \left[ \left( \frac{\delta^{34}\text{S}_{\text{H}_2\text{S}}}{1000} + 1 \right) \times \frac{1-f^{\alpha(\text{S}-\text{H}_2\text{S})}}{1-f} - 1 \right] \quad (\text{A5.9})$$

and for  $\text{SO}_2$  oxidation (eq. A5.10),

$$\delta^{34}\text{S}_{\text{SO}_4(i)} = 1000 \times \left[ \left( \frac{\delta^{34}\text{S}_{\text{SO}_2}}{1000} + 1 \right) \times \frac{1-f^{\alpha(\text{SO}_4-\text{SO}_2)}}{1-f} - 1 \right] \quad (\text{A5.10})$$

where  $f$  is the mol fraction of the reactant(s) reduced/oxidized to  $\text{S}^0$  (and sulfate), relative to the initial reactant(s), and  $\alpha$  is the fractionation factor between  $\text{S}^0$  (or sulfate) and the reactants  $\text{SO}_2$  and/or  $\text{H}_2\text{S}$ , respectively. Equations A5.8 and A5.9 give the  $\delta^{34}\text{S}$  values of experimentally produced sulfur by  $\text{SO}_2$  reduction and  $\text{H}_2\text{S}$  oxidation, respectively. In these calculations, we used the initial isotopy of the reactants with values of  $\delta^{34}\text{S}_{\text{SO}_2} = -2.8 \text{‰}$  and  $\delta^{34}\text{S}_{\text{H}_2\text{S}} = +6.7 \text{‰}$ .

The cumulative isotopic composition of  $\delta^{34}\text{S}_\text{S}$  can then be determined by simple mass balance:

$$\delta^{34}\text{S}_\text{S} = \frac{\sum \delta^{34}\text{S}_{\text{S}(i)} f}{a} \quad (\text{A5.11})$$

where  $f \in \{0.99, 0.98, \dots, 0.01\}$  and  $a$  is the percentage of the already reacted educt(s) or the number of  $\delta^{34}\text{S}_{\text{S}(i)}$  values added for a certain fraction value;  $a \in \{1, 2, \dots, 99\}$ . The stoichiometry of reaction A5.3 indicates that the  $\delta^{34}\text{S}$  values of the total sulfur produced by synproportionation of  $\text{SO}_2$  and  $\text{H}_2\text{S}$  is (resulting from eq. A5.8 and A5.9):

$$\delta^{34}\text{S}_\text{S} = \delta^{34}\text{S}(\text{A5.11})_{\text{SO}_2} + 2 \times \delta^{34}\text{S}(\text{A5.11})_{\text{H}_2\text{S}} \quad (\text{A5.12})$$

To determine the residual  $\delta^{34}\text{S}_{\text{SO}_2}$  from the synproportionation reaction to further calculate the oxidation of this remaining  $\text{SO}_2$  to sulfate, the isotopic value of the disappearing  $\text{SO}_2$  must first be calculated (for the amount of substances, see eq. A5.4):

$$\delta^{34}\text{S}_{\text{SO}_2(\text{dis})} = \frac{n_{\text{SO}_4(\text{i})} \delta^{34}\text{S}_{\text{SO}_2(\text{i})}}{n_{\text{SO}_2}} \quad (\text{A5.13})$$

This value can now be inserted into the equation to calculate the residual  $\text{SO}_2$ :

$$\delta^{34}\text{S}_{\text{SO}_2(\text{residual})} = \frac{\delta^{34}\text{S}_{\text{SO}_2(\text{initial}) - (1-f)\delta^{34}\text{S}_{\text{SO}_2(\text{dis})}}{f} \quad (\text{A5.14})$$

## Versicherung an Eides Statt / *Affirmation in lieu of an oath*

**gem. § 5 Abs. 5 der Promotionsordnung vom 18.06.2018 /  
according to § 5 (5) of the Doctoral Degree Rules and Regulations of 18 June, 2018**

Ich / I, Victoria Kürzinger  
(Vorname / *First Name*, Name / *Name*)

versichere an Eides Statt durch meine Unterschrift, dass ich die vorliegende Dissertation selbständig und ohne fremde Hilfe angefertigt und alle Stellen, die ich wörtlich dem Sinne nach aus Veröffentlichungen entnommen habe, als solche kenntlich gemacht habe, mich auch keiner anderen als der angegebenen Literatur oder sonstiger Hilfsmittel bedient habe und die zu Prüfungszwecken beigelegte elektronische Version (PDF) der Dissertation mit der abgegebenen gedruckten Version identisch ist. / *With my signature I affirm in lieu of an oath that I prepared the submitted dissertation independently and without illicit assistance from third parties, that I appropriately referenced any text or content from other sources, that I used only literature and resources listed in the dissertation, and that the electronic (PDF) and printed versions of the dissertation are identical.*

Ich versichere an Eides Statt, dass ich die vorgenannten Angaben nach bestem Wissen und Gewissen gemacht habe und dass die Angaben der Wahrheit entsprechen und ich nichts verschwiegen habe. / *I affirm in lieu of an oath that the information provided herein to the best of my knowledge is true and complete.*

Die Strafbarkeit einer falschen eidesstattlichen Versicherung ist mir bekannt, namentlich die Strafandrohung gemäß § 156 StGB bis zu drei Jahren Freiheitsstrafe oder Geldstrafe bei vorsätzlicher Begehung der Tat bzw. gemäß § 161 Abs. 1 StGB bis zu einem Jahr Freiheitsstrafe oder Geldstrafe bei fahrlässiger Begehung. / *I am aware that a false affidavit is a criminal offence which is punishable by law in accordance with § 156 of the German Criminal Code (StGB) with up to three years imprisonment or a fine in case of intention, or in accordance with § 161 (1) of the German Criminal Code with up to one year imprisonment or a fine in case of negligence.*

Bremen, den 14.09.2022  
Ort / *Place*, Datum / *Date*

Kürzinger  
Unterschrift / *Signature*